# Study and manipulation of photoluminescent NV color center in diamond

Dingwei Zheng

**HAL Id: tel-00595302**
**https://tel.archives-ouvertes.fr/tel-00595302**

Submitted on 24 May 2011

# Study and Manipulation
# of Photoluminescent NV Color Center
# in Diamond

Étude et Manipulation des Propriétés de Spin du Centre Coloré
photoluminescent NV dans des nanocristaux de diamant

to obtain the title of

## PhD of Physics

of École Normal Supérieure de Cachan
and East China Normal University

Defended by

## Dingwei ZHENG

October 27, 2010

**Jury :**

| | | | |
|---|---|---|---|
| *Reviewers :* | Prof. Nicolas TREPS | - | LKB (Université Pierre et Marie Curie) |
| | Prof. Huan-Cheng CHANG | - | IAMS (Academica Sinica) |
| *Examinators :* | Prof. Longsheng MA | - | LPS (East China Normal University) |
| | Prof. Jean-François ROCH | - | LPQM (ENS de Cachan) |
| *Advisor :* | Prof. François TREUSSART | - | LPQM (ENS de Cachan) |
| | Prof. Xinye XU | - | LPS (East China Normal University) |

# Contents

# Contents          3

# Introduction

At present, quantum information is a rapidly developing branch in modern science. The unit of quantum information is the quantum bit (qubit) which is a two-level quantum system. Unlike classical digital states, a two-state quantum system can actually be in a superposition of the two states at any given time. Quantum information differs from classical information in several respects:

- Reading of a qubit results in a projection on a basis.
- An arbitrary state cannot be cloned.
- The state may be in a superposition of basis values.

Solid-state systems, in which spins (electron and nuclear) of various defects and impurities in semiconductors are used as stationary qubits. Quantum dots [119] and single molecules [85] have been utilized to generate single photon emission. But perhaps the most promising and applicable source of single photons for practical applications arises from optical defects in diamond. It is the only material presently known which contains room temperature photostable defects capable of producing single photon pulses with a high effciency. To date, of the over 500 known defect centers in diamond, only four have been identified as single photon emitters: silicon vacancy (SiV) center [139], Nikel related complex [49, 144], NV color center [75], and Chromium related complex [3]. The very low emission rates of the SiV center and the difficult to controllably fabricate Ni and Cr related centers at the single level, limit the practical applications with these centers. In the contrary, the nitrogen-vacancy (NV) center is up to now the best candidate for quantum information applications, owing to its room-temperature photostability, allowing single photon generation, and to its capability of electron spin manipulation.

About ten years ago it was noted that the NV in its singly-charged state, $NV^-$ has many of the desired attributes of a qubits [86]: its triplet ground state provides long coherence spin states to manipulate the qubit, and it has a convenient optical transition in the visible. In recent years much progress has been made towards the realization of quantum information processing (QIP) based upon NV centers in diamond. We

can build an efficient single-photon source [17, 75]; Optical and microwave qubit gate operations have been performed [26] using optical readout of single electron [70] and nuclear spins [71, 29, 143]. Electron spin coherence times exceeding 1 ms at room temperature [10] have been observed with nuclear spin-zero environment of the diamond lattice. A variety of techniques has been employed for coupling NV centers in diamond to optical microcavities [11, 12, 109, 126] and waveguides [46] for realization of large-scale quantum information processing and for quantum repeater systems.

Optical readout of the NV$^-$ electron spin resonance has also allowed advanced application to nanomagnetometry. Hgh sensitivity magnetometers have been developed with different techniques such as: superconducting quantum interference device (SQUID)[15], scanning Hall probe microscopy [24], magnetic force microscopy (MFM) [94], and magnetic resonance force microscopy (MRFM) [118, 88]. Though these techniques offer high sensitivity, they require cryogenic cooling or vacuum conditions, they are feasible to some particular domain. In contrast, the NV color center has several outstanding advantages for this application. Optical polarization and spin state readout facilitates convenient and nonivasive far field detection. The atomic NV sensor permits the minimization of the sample-sensor distance, and the manipulation can be carried out at room temperature [9]. By using NV centers, researchers are able to image the vector magnetic field [87, 129], to sense the fluctuating nanoscale magnetic fields [58, 95] and also to readout single nuclear spins [71, 128, 106]. Recently, using a magnetic tip to produce a large field gradient, NV diamond has achieved 5 nm resolution under ambient condition [10].

Numerous studies have been done to understand the NV$^-$ center electronic states and energy levels. Uniaxial stress measurements [33] have determined that the NV center has $C_{3v}$ symmetry, with the ZPL emission band associated with an $A$ to $E$ dipole transition. The hole burning EPR signal [112], optically detected magnetic resonance(ODMR) [107], electron spin resonance [113, 84] and Raman heterodyne experiments [89] have established the energy level scheme of NV$^-$ center . Several theoretical works have been done, using the Linear Combination of Atomic Orbitals (LCAO) approach to build the electronic orbitals to describe the possible quantum states, looking at the NV center as a molecule [81]. Moreover, group theory results are used to take into account the symmetry of the diamond crystal, and of the NV itself [91, 92]. However, the knowledges about NV color center level structure are still incomplete and numerous studies are in progress to unveil unknown properties.

In this dissertation, we investigate a variety of aspects of NV centers in the diamond including: production, photoluminescence property, electron spin property etc. by means of confocal microscopy and optically detected magnetic resonance (ODESR) technique. Besides, different means to achieve far field optical super resolution will be discussed as well. The thesis contains two parts, Part I from Chapter 2 to Chapter 4,

which mainly concern the optical properties of NV color center. Part II includes Chapter 5 to Chapter 8 and deals with the spin manipulation and spin readout technique of NV color center. The thesis is organized as follows:

In Chapter 2, we will firstly review different techniques for producing diamond and creating NV color centers. Then the photochromic effect of NV centers due to the modification of NV center charge [$NV^-\leftrightarrow NV^0$] is investigated. The photochromic effect of a single NV color center is of great interests in order to better control the NV center charge state $NV^0$ and $NV^-$ centers. Recently the negatively charged form $NV^-$ has the remarkable spin properties optically detectable.

In Chapter 3, we study the reversible quenching of NV color center photoluminescence under infrared (IR) pulsed laser irradiation in diamond. Several approaches are used to interpret this effect. We conclude that the IR effect is induced by multi-photon absorption of diamond crystal. It is possible to use this effect for STED-like super resolution imaging of NV center in diamond nanocrystals.

In Chapter 4, various far field optical super-resolution techniques are demonstrated. This include annular shaped illumination beam, or doughnut shaped beam in the regime of saturation, and IR pulsed excitation quenching effect. Their working principles and spatial resolution improvement are discussed.

In Chapter 5, the electron spin property of NV color center is reviewed briefly. Optically detected electron spin resonance (ODESR) experiment is applied to the $NV^-$ color center. The samples and experimental setup used in the second part is also introduced.

In Chapter 6, the NV center electron spin is manipulated with a static magnetic field, continuous microwave field and pulsed microwave field. Properties of NV color centers (PL lifetime, PL intensity, Rabi-oscillation, coherence time) are investigated through these manipulations.

In Chapter 7, the ODESR experiment is applied to an ensemble of NV colors. The four possible orientations of NV spin axis are figured out from the Zeeman shift of NV electron spins. We also developed a fluorescence lifetime monitoring method to have access to the magnetic field without the necessary of microwave excitation of the ESR. Moreover, it is possible to evaluate the uniformity of spin orientation distribution of an ensemble of NV centers from this experiment. This is of great importance for the application of ensemble of NV centers as a magnetic field sensor.

In Chapter 8, the NV spin and NV optical dipoles' orientations in the space is determined using the Zeeman effect and polarization measurements. These two different approaches lead to an identical result. This is a vital study for efficient coupling of

$NV^-$ centers to photonic structures and for magnetic field sensing.

# Part I

# Optical property of NV color centers

# NV$^0$ and NV$^-$ color centers in diamond

## Contents

## 2.1   Overview of diamond and color centers in diamond

### 2.1.1   General introduction of diamond and defects

As a precious gemstone, diamonds are fancy-colored, in addition to its superlative physical qualities, the highest hardness and thermal conductivity of any bulk material, the study of diamond covers numerous domains such as gemology, material, biology, physics, etc.

Diamond is an allotrope of carbon, where the carbon atoms are arranged in a variation of the face-centered cubic crystal structure, called a diamond lattice. Such

special structure results in the strong covalent bonding between its atoms, which is the origin of its hardness. Diamond has a wide band gap of 5.5 eV corresponding to the deep ultraviolet wavelength of 225 nm. This means pure diamond should transmit visible light and appear as a clear colorless crystal. As the materials scientist F. Franck said, "Crystals are like people, it is only the defects that make them interesting. " In fact, colors of diamonds come from small amounts of defects or impurities (about one per million of lattice atoms) in diamond lattice. The luminescent defects, which have special energy structures, are able to absorb or fluorescent photons with special wavelengths. Thanks to different kinds of defects, the diamonds are rendered blue (boron), yellow (nitrogen), brown (lattice defects), green (nickel), purple, pink, orange or red as seen in Figure 2.1, which not only make it beautiful but are also interesting for scientific researches. Such kind of luminescent defects are called color centers and more than 500 color centers in diamond have been catalogued until now [145].



**Figure 2.1:** Colorful diamonds with luminescent defects in diamond lattice.

### 2.1.2   Fabrication of diamond crystal

Most natural diamonds are formed at high-pressure high-temperature conditions existing at depths of 140 to 190 kilometers in the Earth mantle [20, 45], the growth occurs over periods from 1 billion to 3.3 billion years. Diamonds can also be obtained by synthetic method, which can satisfy the large demand fro the gemological and industrial use. The High-Pressure High-Temperature (HPHT) procedure is the first developed synthesis of diamond [22]. It became a commercial reality during the 1950s and remains the major manufacturing method for synthetic diamond products. In essence, HPHT emulates the way in which natural diamonds are created deep in the earth where the

enormous pressure makes carbon crystals with the denser structure of diamond more stable than those of other carbon allotropes such as graphite (Figure 2.2). The HPHT growth process offers a significant degree of control over the quality and geometry of diamond obtained. Most diamond produced by this method is small grains of type Ib. However, longer controlled growth periods enable production of single crystal Ib stones with dimensions routinely up to 8 mm. The drawback of this technique is that the experimental condition of pressure as high as 60 000 atmospheres is quite tricky and costly.
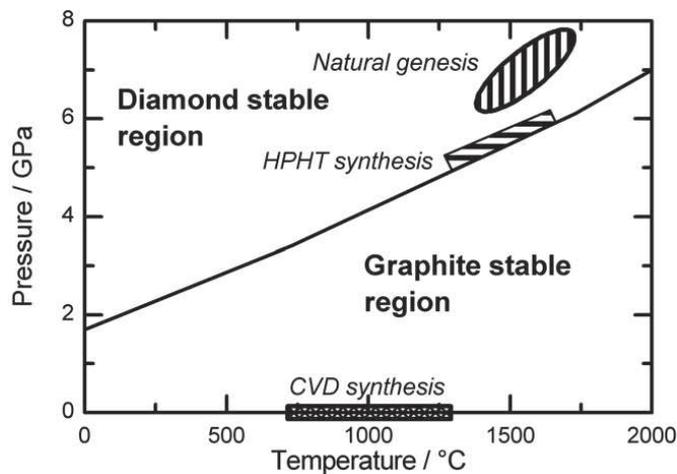


**Figure 2.2:** Phase diagram for carbon indicating main regions of pressure-temperature space in which diamond growth occurs [8].

Another popular method of growing synthetic diamond is Chemical Vapor Deposition (CVD). At low pressure (below atmospheric pressure), a mixture of carbon-rich gases (typically 1 to 99 methane to hydrogen) is broken into fragments and reassemble into diamond film on a surface by microwaves, hot filament, arc discharge, welding torch or laser. The growth rate is typically about 1 $\mu$m per hour. Techniques such as increasing the pressure of the carbon-rich gas [135] have been developed to accelerate the growing processor. The CVD diamonds are thin and flawed films. The flaws can be reduced by choosing a pure diamond as the substrate.

Diamond nanocrystals can also be formed by detonating certain carbon-containing explosives in a metal chamber. These diamond nanocrystals are called "detonation nanodiamond". The explosion heats and compresses the graphite to an extent sufficient for its conversion into diamond. The product is always rich in graphite and other non-diamond carbon forms and requires prolonged boiling in hot nitric acid (about 1 day at 250 °C) to dissolve them.

## 2.2   NV color centers in diamond

### 2.2.1   Creating NV color centers in diamond

The NV color center in diamond lattice is one of the most well known color centers. It is a point defect in the diamond lattice, formed by a substitutional Nitrogen atom combined with an adjacent vacancy in diamond lattice as shown in Figure 2.3. It can be viewed as a molecule trapped in diamond lattice. The NV color center absorbs well the photons in VIS-UV range and fluorescent broadly in the VIS range as shown in Figure **??**. Bright, photostable luminescence, working at ambient condition characters of NV colors enables it for the applications of scientific imaging, biolabeling as well as quantum communication and computing.
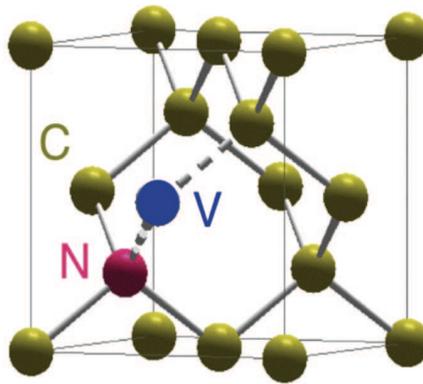


**Figure 2.3:** Schematic representation of the NV center structure.

NV color center can be found in natural diamonds, but the concentrations and locations of defects are quite different from one to another. In order to controllably create NV, some synthesize techniques have been developed. The NV color centers can be created after obtaining diamond crystal or during diamond growth process. Figure 2.4 shows a common technique of producing NV color center, which begins from the substitutional nitrogen atoms (called C or P1 centers in diamond literature). Diamonds containing such impurity are firstly irradiated by high-energy particles such as electrons, protons, neutrons, ions and gamma particles, which produce lattice vacancies. Then the sample is annealed at temperatures around 800°C, in order to mobile the vacancies. At this temperature, substitutional nitrogen produces strain in the diamond lattice and efficiently captures moving vacancies, then forms the NV color center. It was recently demonstrated that some oxidate procedure such as acid cleaning or thermal oxidation were used to remove the surface contamination caused by annealing, and therefore increase the brightness of nanodiamonds.

**Raw diamond**

50μm

**Irradiated
(electron beam)**

**Annealed
(800°C, 2 hours)**
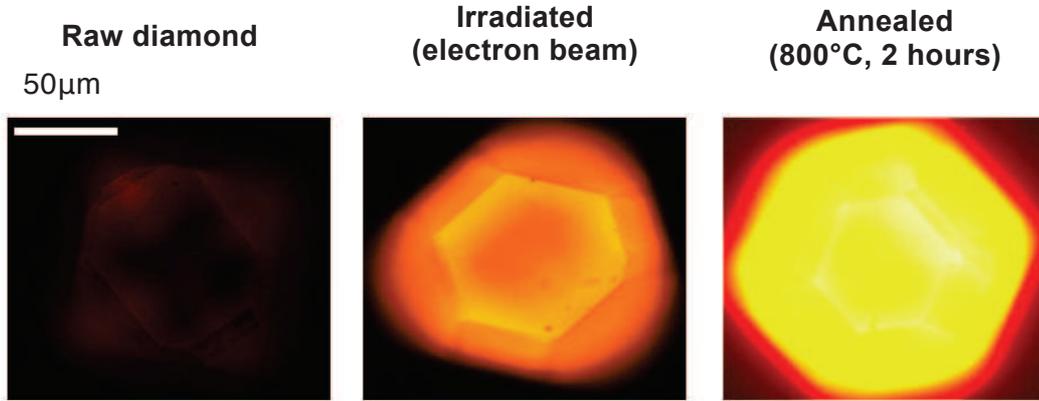


**Figure 2.4:** The common process of creating NV color centers. Images are obtained by measuring photoluminescence of the diamond.

Another approach of creating NV color centers is nitrogen implantation in a very pure type IIa diamond [96]. In this approach, nitrogen atoms are implanted by focusing a nitrogen ion beam on the diamond surface, meanwhile, vacancies are created during the slowing down of the implants. The NV center can be formed upon annealing. The advantage of this technique is the low paramagnetic impurity contaminant, namely paramagnetic nitrogen. It is well known that for quantum information science, spin qubits have to be introduced in a spin-free lattice to ensure long coherence time, paramagnetic nitrogen substitution forms a spin bath thus limiting the coherence time [132]. The efficiency of this process is limited by the number of vacancies available in the vicinity of the N stopping position and by the capture cross section of vacancies by nitrogen. Recently, a two step implantation process which includes low dose $N_2^+$ molecular ion implantations followed by high dose C implantation has been demonstrated to increase the generation efficiency of NV centers by over 50 % [102].

The CVD-grown diamond is unique in that NV centers can be created during the synthesis process. The NV color center incorporated diamond film can be grown with 0-0.1% $N_2$, 0.7% $CH_4$, 99.2% $H_2$ gas mixture, at about 800°C substrate temperature and low pressure [111]. The NV center concentration varies with the nitrogen doping levels. Single defects can be created by optimizing the nitrogen doping levels.

In the frame work of this dissertation, we have used samples fabricated by different fabrication methods, such as HPHT and CVD. The NV centers are created by high dosage irradiation with electron, proton and nitrogen particles.

### 2.2.2   Optical addressing of single NV color center

Optical excitation and detection of the NV color centers photoluminescence(PL) is realized with a home-built setup, illustrated in Figure 2.5. The confocal microscopy (left part) allows to address single NV emitter and provide very high SNR (signal to noise ratio) photoluminescence. The NV color center is excited by either a cw laser or a pulsed laser (wavelength=532 nm) depending on the application. The excitation beam is focused onto the sample using a high numerical aperture microscope objective (NA=0.95) working in air. The focusing point is raster scanned relative to the sample with nanometric resolution, using a piezoelectric driven mirror tilting system. The photoluminescence of the excited NV center is collected by the same objective and spectrally filtered from the remaining pumping light by a long-pass filter with a wavelength cut-off at 580 nm, and a transmission >80% in the range 580-750 nm. A standard confocal detection system is also used to select the luminescence coming from a sample volume of about 1.43 $\mu$m$^3$. The mirror M2 is mounted on a flip-flop base, which enables us to measure either the spectrum or intensity of the photoluminescence. In order to identify the single photon emission, we use the so-called Hanbury-Brown-Twiss (HBT) technique as shown in the right bottom side of Figure 2.5. The PL beam is divided into two identical beams using a 50/50 beam splitter, and detected by two avalanche photodiodes (APD), the signals from two APDs are analyzed with the correlation function.

$$g^2(\tau) = \frac{< n_1(t)n_2(t+\tau) >}{< n_1(t) >< n_2(t+\tau) >}, \tag{2.1}$$

where $n_1(t)$ $[n_2(t+\tau)]$ is the number of counts registered on the detector APD1 (APD2) at time $t$ $[t+\tau]$. The $< \cdots >$ symbol means the time average computed by integrating over a long time period. It turns out that $g^2(\tau)$ represents the coincident between counting of APD1 at the moment of $t$ and APD2 at $t + \tau$.

For a single photon beam, the photons come out with regular gaps between them. A single photon cannot be splitted by the beam splitter, and consequently it will be detected either by APD1 or APD2. Therefor, the coincidence detection between APD1 and APD2 at zero-delay ($\tau = 0$) will be 0. This zero value of g$^{(2)}$(0) obtained at zero delay time is then the signature of the single photon for all our work.

### 2.2.3   Photoluminescence of NV$^0$ and NV$^-$ color centers

We first begin to study NV color center in diamond nanocrystals, the sample preparation will be introduced in section 2.1. Figure 2.6a is the scanning image of the sample with the confocal setup in Figure 2.5. The bright spots are fluorescent emitters corresponding to NV color centers. It is well known that The NV color center exhibits two charge states: neutrally charged NV$^0$, with a zero-phonon line at 575 nm (2.156 eV)
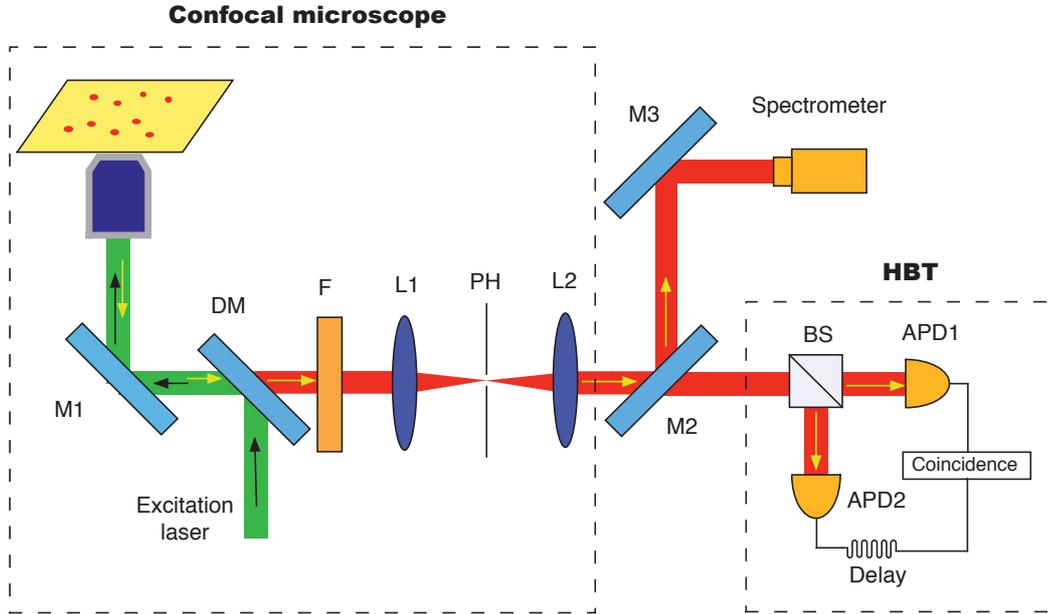
**Figure 2.5:** Optical setup used for detection of PL of NV color center in diamond: M1 is a mirror mounted on a piezoelectric driven tilting system; DM is a dichroic mirror which separates the fluorescence from the excitation light; M2 is a flip-flop mirror for choosing measurement of photon counting (on the avalanche photodiodes APD) or photoluminescence spectrum (using an imaging spectrograph SPC).

[98] and negatively charged $NV^-$, with a zero-phonon line at 637 nm (1.945 eV) [33]. The charge state of NV centers can be determined from their spectrums (Figure 2.6b, 2.6c). Both $NV^-$ and $NV^0$ centers can be found in this sample, the ratio is about 1:1.

The $g^{(2)}$ curves of $NV^-$ and $NV^0$ centers are depicted in Figure 2.6. Figure 2.6d and 2.6e are the $g^{(2)}$ curve of single $NV^-$ and $NV^0$ centers at different excitation power. It is well known that $NV^-$ color center has a long lifetime metastable level (Figure 5.2a). When excited with a strong laser power and become saturated, the electron will be populated to the metastable level and results in the bunching effect [16] as shown in Figure 2.6d. In contrast, all the observations on single $NV^0$ color centers showed no bunching effect for any excitation powers (see Figure 2.6e), which may leads to a conclusion that the $NV^0$ color center is a two level system without the metastable state as shown in Figure 5.2b.

Our proposed energy level scheme of $NV^0$ center lacks the dark metastable state compared to the $NV^-$ center. It is well known that the long-lifetime metastable state can trap the electrons and decrease the PL intensity of NV centers. The two-level $NV^0$ center is hence supposed to have higher PL intensity compared to the $NV^-$ center. However, the fluorescence property of NV colors are strongly influenced by its ambient
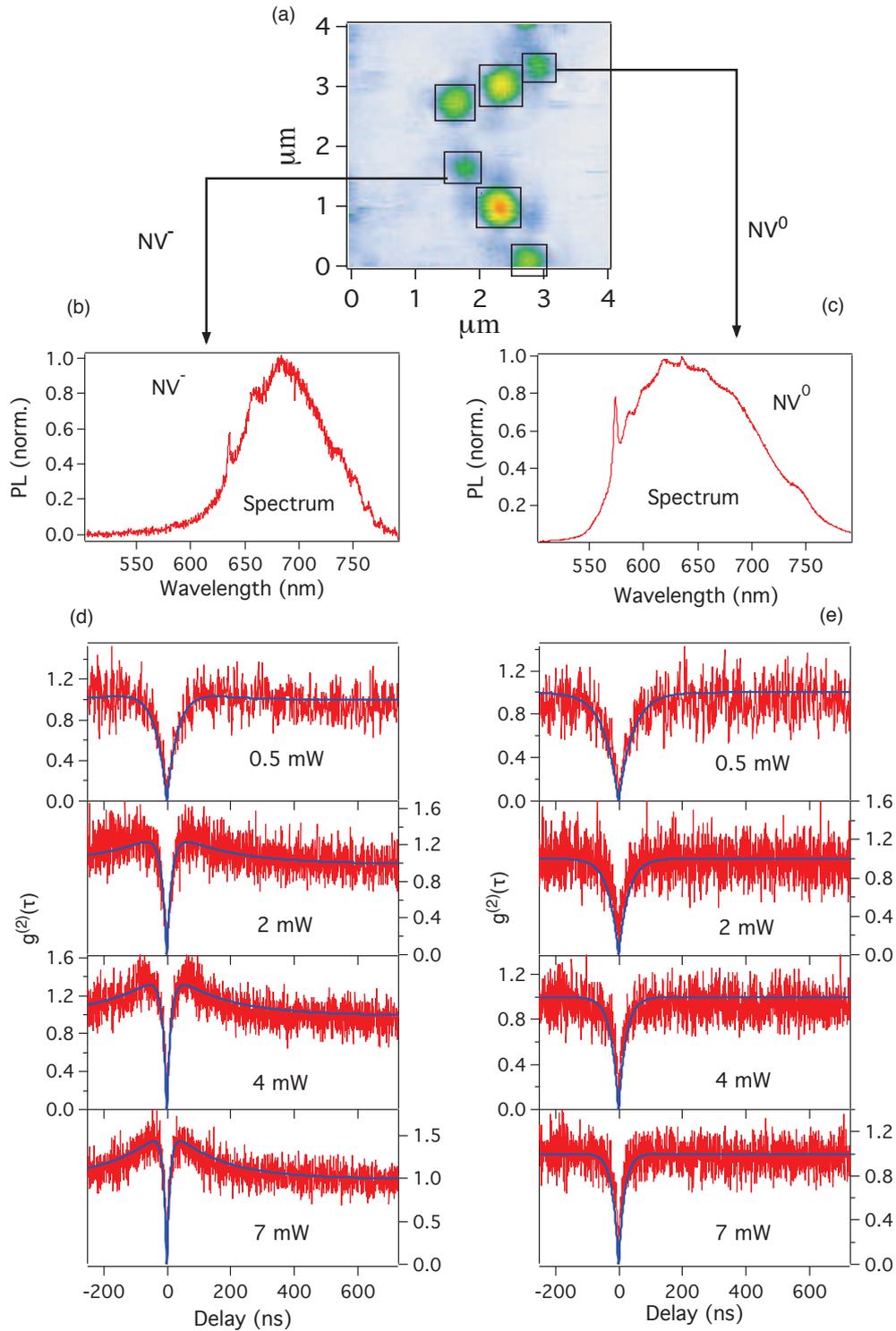
**Figure 2.6:** (a) is the scanning image of diamond nanocrystals containing NV color centers. (b) and (c) are the PL spectrum of a single NV$^-$ and a single NV$^0$ color centers, (d) and (e) are the corresponding autocorrelation function measurements. All measurements are realized under the same experimental conditions and at room temperature.
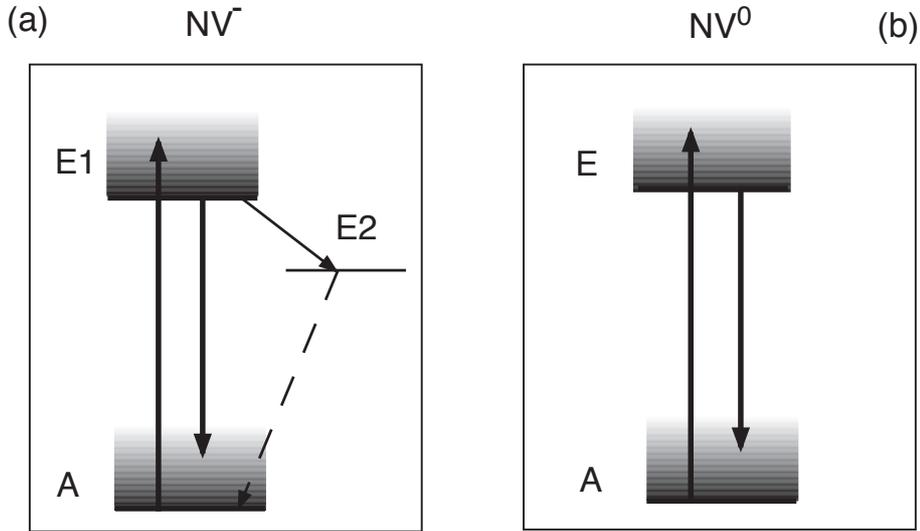
**Figure 2.7:** Proposal of energy diagram of NV$^-$ and NV$^0$ color centers. The 2-level structure of NV$^0$ center allows obtaining a perfect antibunching curve, while the 3-level structure of NV$^-$ color center causes the bunching effect.

conditions and its dipole orientations, it seems difficult to do the comparison in the the aspect of PL intensity. Fortunately, the photochromic effect of NV color center are able to switch the NV color center between different charge states, which is quite useful for investigating the single NV$^-$ and NV$^0$ in the same site i.e. under the same condition.

## 2.3 Study of photochromic effect between NV$^0$ and NV$^-$ color centers

### 2.3.1 Review of the charge state study of NV color centers

When the NV center is present in a diamond crystal, a single charge state often dominates but both charge states can co-exist [80]. The charge state of NV color center was firstly supposed to depend on the nitrogen impurity according to studies on vacancy related impurities in diamond [34]. In order to explain the two state coexistence of NV$^0$ and NV$^-$, the impurities in the vicinity of the NV center was brought forward to dominate the charge state of NV center [30]. The study of vertical distribution of NV centers in high purity diamond indicated that the NV$^0$/NV$^-$ intensity ratio increases during the first 150 nm of etching [121], which suggests that the charge state of NV center is dominated by an electronic acceptor layer near the surface.

These two charge states could be created independently but also can be transformed from one to the other by applying different kinds of excitations. This transformation is called photochromic effect since it changes the band gaps between two charge states. The photochromic effect, i.e. photon-induced transformation of charge state of NV color center has been discussed in various studies. Y. Dumeige et al [39] reported that by exciting a nanodiamond with a 500 nm femtosecond laser, a single $NV^-$ color center was first transformed to a single $NV^-$ color center combined with a single $NV^0$ color center and finally become a single stable $NV^0$ color center. N. B. Manson et al [90] reported a photochromic effect of an ensemble of NV color centers, and verified the proportion of the $NV^-$ and $NV^0$ color centers as a function of the excitation wavelength and excitation time. T. Gaebel et al [49] reported a reversible photochromism effect, by exciting NV color centers embedded in a bulk diamond with a continuous laser at $\lambda = 514$ nm, a single $NV^0$ color center was ionized to a single $NV^-$ color center and finally relaxation to a single $NV^0$ color center under dark condition. All these observations were generally attributed to electron excitation and capture dynamics between nearby nitrogen donors and NV centers.

Recently, selective oxidation have been applied on diamonds containing NV color centers which were created by ion implantation and annealing [47]. The oxidation converts neutral NV centers to negatively charged NV centers. The results suggest that the graphitic damage is one possible reason for the electronic depletion effect.

The photochromic effect has also been observed in our studied. The behavior differs from sample to sample, moreover, the observation of photochromic effect of a single NV color center enables us to investigate the photoluminescence of $NV^0$ and $NV^-$ color centers and their comparisons.

### 2.3.2   Photochromic effect of NV color center in bulk diamonds

The photochromic effect can be observed on both CVD and HPHT bulk diamonds. The CVD bulk diamond sample is provided by CEA-LIST (Laboratoire d'Intlégration des Systèmes et des Technologies, CEA Saclay). Nitrogens are implanted in diamond crystal by high energy irradiation, and then the sample is annealed with Oxygen gas at 450°C for 8 hours. NV color center concentration is experimentally determined to be about $2 \times 10^3 / \mu m^3$. We have studied the photochromism of this sample and the results are shown in Figure 2.8. Firstly, the sample is excited with low laser power (3 $\mu$W), the PL spectra shows that most of the centers are $NV^0$. The spectra red shifts as we increase the excitation power, the ZPL of $NV^-$ center becomes more and more pronounced indicating the transition of $NV^0$ centers to $NV^-$ centers. This photochromic effect is reversible. Indeed, as soon as we decreased the excitation power to 5 $\mu$W, the centers return to the former $NV^0$ form.
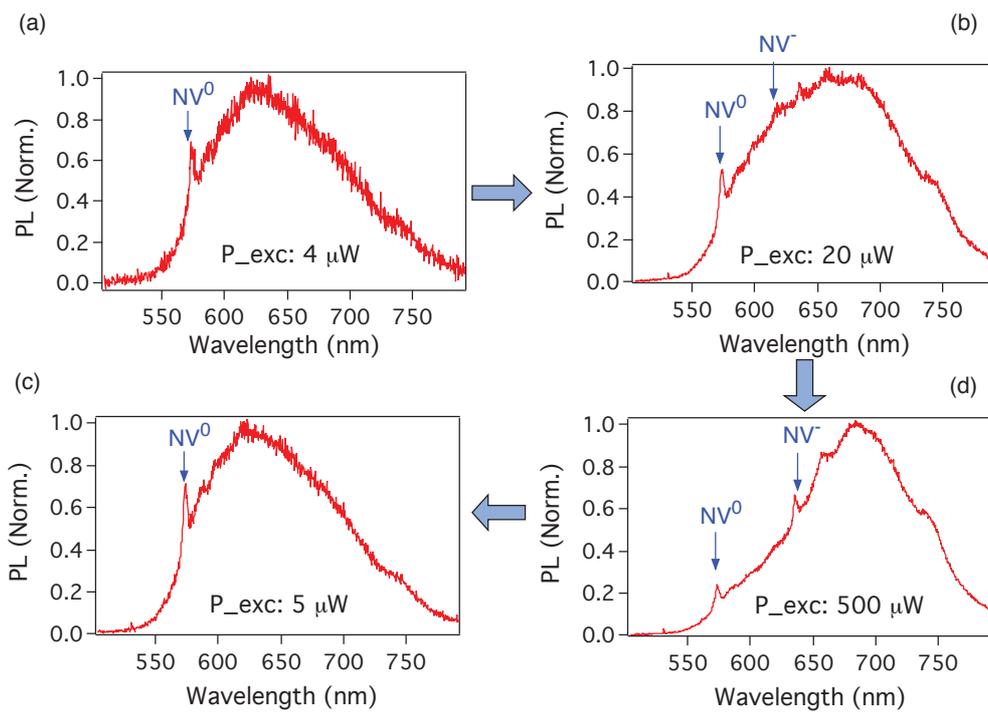
**Figure 2.8:** Reversible photochromic of NV color centers in a CVD bulk diamond as a function of the excitation power. P_exc, the PL spectra red shifts when increase the excitation power, and recovers as soon as the excitation power decreases. The sample contains multiple NV color centers and it is excited by a continuous laser at $\lambda$=532 nm.

A type Ib HPHT bulk diamond provided by CEMHIT (Conditions Extrêemes et Matériaux: Haute Température et Irradiation) Orléan also present the photochromic effect. This HPHT bulk diamond with intrinsic substitutional Nitrogens is irradiated by a proton beam then annealed at 800°C for 10 hours. NV color centers are formed with high concentration which is experimentally measured to be about $7\times10^5/\mu m^3$. The PL spectras obtained by different excitation powers are shown in Figure 2.9. At low excitation power, the NV$^0$ and NV$^-$ center co-exist identified by the ZPLs at 580 nm and 637 nm respectively. While at high excitation power, the NV$^0$ ratio decreases, and even disappears at 12 $\mu$W. The excitation power is chosen in a random order, hence the photochromic effect of this sample is also reversible.
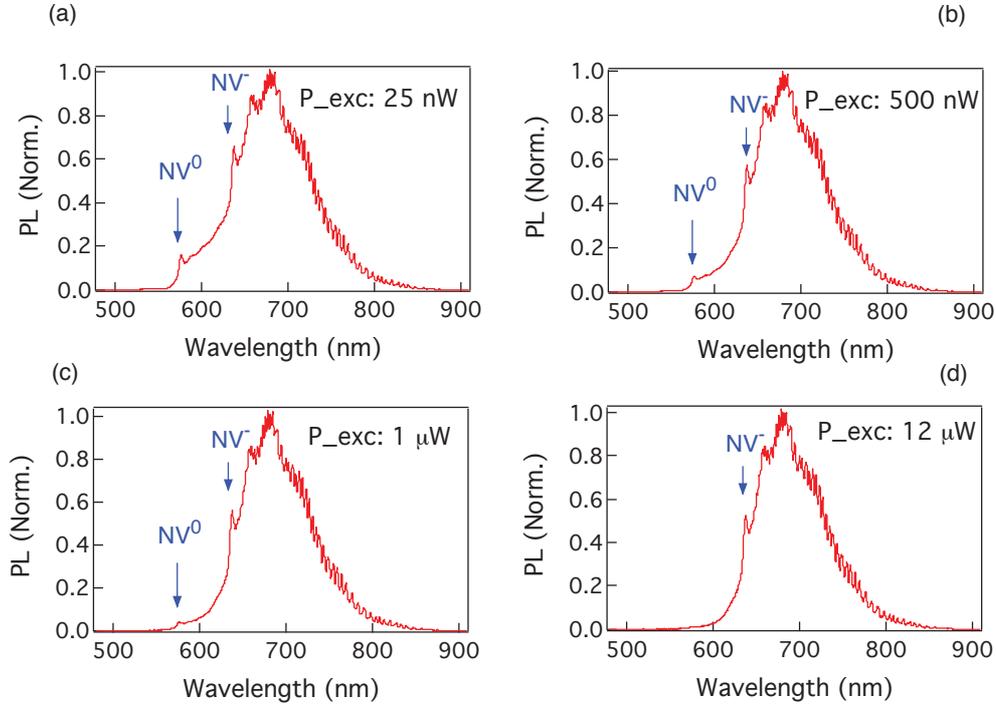


**Figure 2.9:** PL spectra of a proton irradiated HPHT bulk diamond taken at different excitation power, ZPL of NV$^0$ decreases with excitation power and disappears at an excitation power stronger than 8 $\mu$W. The sample contains multiple NV color centers and it is excited by a continuous laser at $\lambda$=532 nm.

In summary, both of these two bulk diamond samples behave a reversible photochromic effect. The neutral NV$^0$ charge state is stable at low excitation power, by increasing the excitation power, the proportion of NV$^0$ centers decreases or even disappear in the case of the proton irradiated HPHT bulk diamond. However, since these samples have high NV concentrations, it is not clear wether the NV$^0$ center simply transforms to NV$^-$ or the NV$^0$ centers are quenched at high excitation power. In

the following section, the photochromism of a single NV color center in a diamond nanocrystal will be studied in detail.

### 2.3.3 Photochromic effect of a single NV color center in nanodiamonds

High-brightness NV associated nanodiamonds (NDs) used for this study are provided by Institute of Atomic and Molecular Science, Academia Sinica, Taiwan. The NV embedded NDs were produced through radiation-damage of synthetic type Ib diamond powders using 40 keV $He^+$ bombardment at a dose of $1 \times 10^{13}$ ions $cm^{-2}$. The mean size of the particles is about 20 nm and each ND contains about 1 10 NV color centers. The NDs are dispersed into water, then spin coated onto a quartz substrate. Statical study of the sample shows that about 10 % of the detected NDs contain single NV color center. Both single $NV^0$ and $NV^-$ are found with a ratio of about 50:50. Single NV color centers in this sample have an average counting rate of about 60 kcps, with a saturation power of about 7 mW.

We focus the excitation beam to excite a single $NV^-$ and measure the spectrum and the $g^{(2)}(\tau)$ at a function of the excitation power. We found that when the excitation power is about 20 mW, the $NV^-$ spectra blue shifts to the one of $NV^0$ center while the $g^2(\tau)$ indicated that the $NV^-$ center remains single. The photochromism of NV color center was generally explained by the ionization effect of high excitation power. The excited electron of $NV^-$ color center is transferred to other impurities by tunnel effect, and then the color center becomes neutral charged ($NV^0$).

In this case, the same single NV color can be either negatively charged or neutral, which enable us to make a direct comparison of the PL between these two charge states in the same experimental condition. The PL intensities as a function of excitation power are plotted in Figure 2.11. Obviously, after the transformation, the emission rate increases by a factor of about 1.6. This can be another proof for the two-level energy scheme of $NV^0$ color center shown in Figure 5.2. Indeed, without the dark metastable state, the excited electron has only one way to relax to the ground state, and $NV^0$ emits more photons than $NV^-$. With such energy scheme, the higher PL intensity of the $NV^0$ color center compared to $NV^-$ can be well explained.

Unlikely to the bulk diamond samples, the high excitation power transforms irreversibly a single $NV^-$ color center to a single $NV^0$ center. The newly created $NV^0$ center partially returned to the negatively charged state after 20 hours dark relaxation. The transformation power is much higher, about 10 mW,

In order to verify the stability of the new created $NV^0$ color center, we measured the emission photon number as well as the $g^{(2)}(\tau)$ behavior after 20 hours relaxation
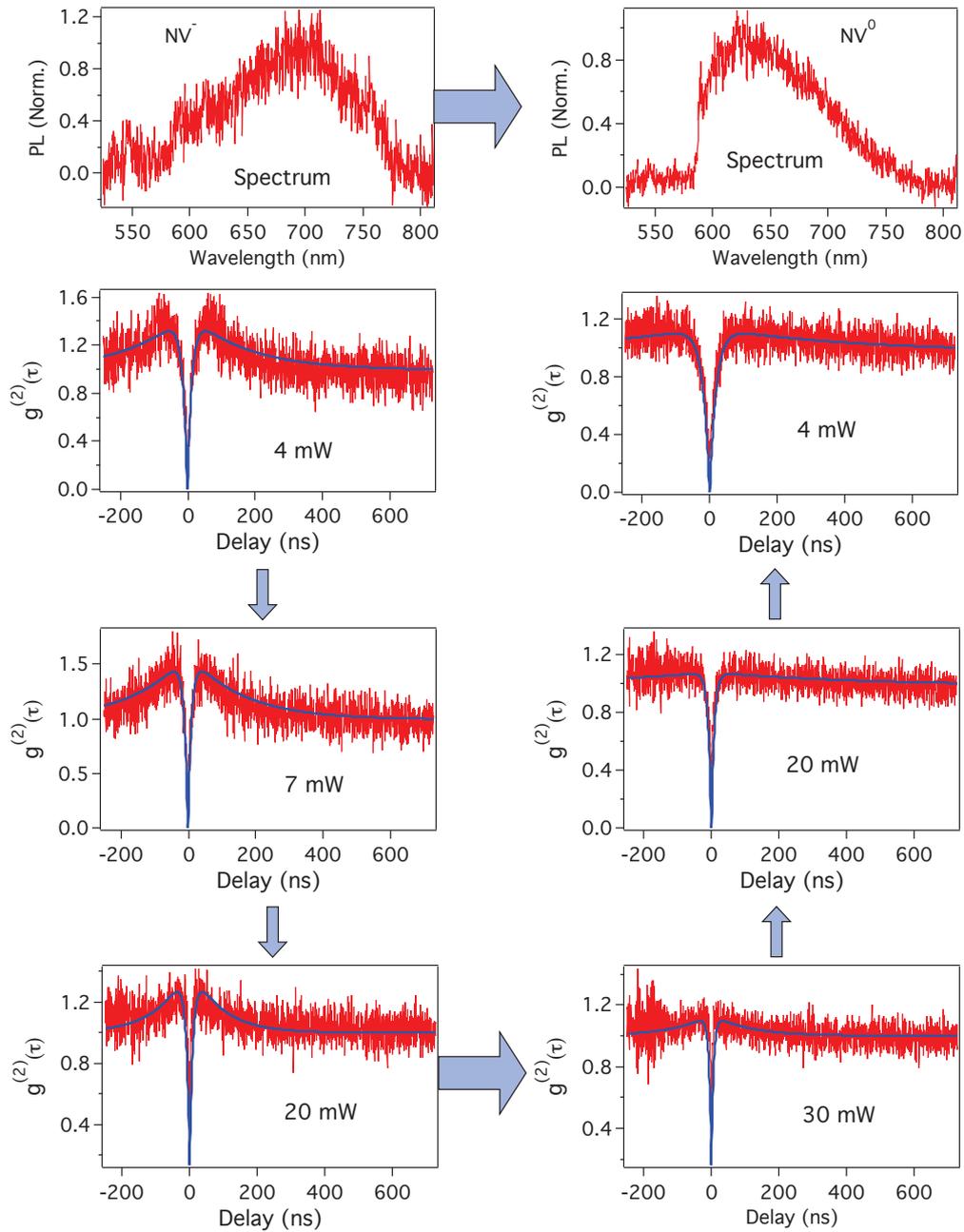
**Figure 2.10:** Photochromic effect of single NV color center in FND, A single NV$^-$ color center is transformed to a neutral NV$^0$ charge state after irradiated with 10mW 532nm laser, The irradiation time is more than 5 minutes.
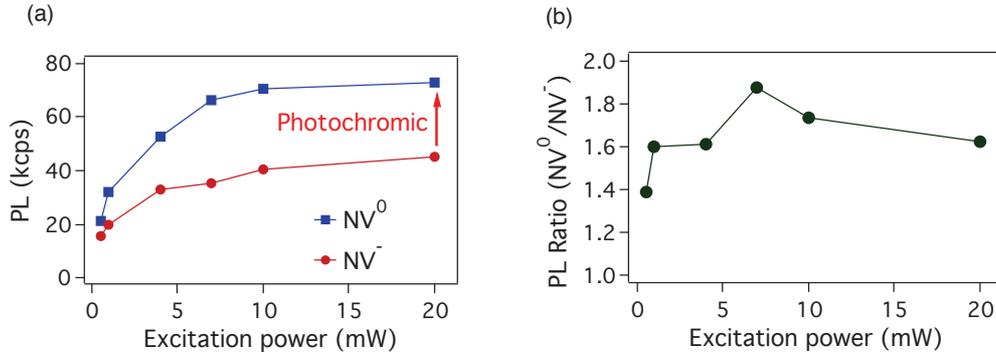
**Figure 2.11:** Figure (a): comparison of emission photon numbers in function of the excitation power, obtained by a single NV color center, in neutral and negative charge states. Figrue (b): ratio of emission photons obtained with NV$^0$ and NV$^-$ single color centers vs excitation power.
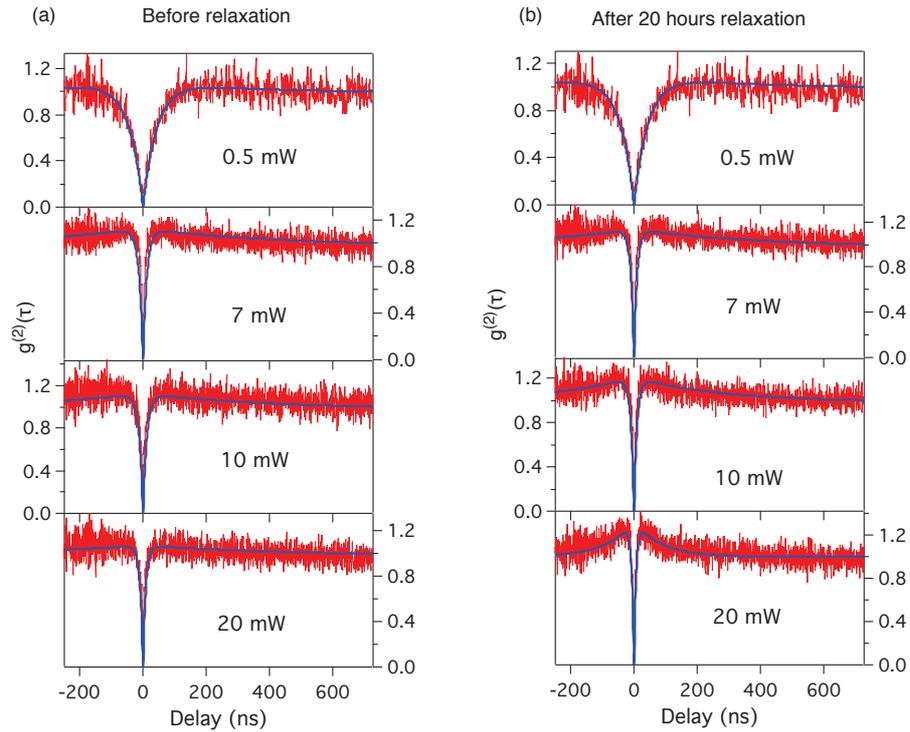


**Figure 2.12:** Relaxation of photochromic effect. Figures at left: g$^{(2)}$ measurements of the NV center obtained just after a strong irradiation, the color center is ionized to a neutral charged state. Figures at right: g$^{(2)}$ measurements of the same NV center obtained after 20 hours relaxation, the color center remains single, NV$^0$ returns partially to NV$^-$

under dark condition. As illustrated in Figure 2.12, the color center remains single
and the NV$^0$ color center tends to return to negatively charge state after 20 hours of
relaxation. However, after 20 hours, the proportion of NV$^-$/NV$^0$ is really low, and
bunching effect (signification of NV$^-$ center) is observed only at very high excitation
power.

## 2.4   Conclusions

In conclusion, we firstly reviewed different techniques of synthesizing diamond crystal
and creating NV color centers in diamond crystals. In our study, the home-built confo-
cal microscope is employed to scan diamond sample surface and address the fluorescent
NV color centers. The single NV color centers are identified with HBT technique. We
then investigated the photochromic effect of NV color centers in various samples pre-
pared by different techniques. The photochromism behaves in many ways. However,
comparing all the results published and recently obtained by us, it seems that neutral
charge state of NV center is more stable at low excitation power. Finally, we propose
a two-level energy scheme for NV$^0$ color center base on the photon correlation curve
at saturation power and the PL intensities of the two charge states of a photochromic
single NV center.

Our observation shows that NV$^0$ center is "brighter" than NV$^-$ center which satisfies
the requirement of bio-labelling. However, without the "dark" metastable state, the
electron spin state of NV$^0$ centers cannot be read-out optically as NV$^-$ centers. The
technique of optical read-out of electron spin state will be discussed in Chapter **??**.

# Control of the photoluminescence of NV color centers

## 3.1 Introduction

The nitrogen-vacancy (NV) color center in diamond has been identified as a system of choice for single photon generation [17] and individual electron spin manipulation [70]. This color center has the great advantage of being photostable at room temperature and does not exhibit any photoblinking. Many applications have beed proposed using either the optical or magnetic property of such NV color centers.

In order to realize these applications, improvements of photoluminescence properties, such as photoluminescence lifetime [126, 130], emission spectrum [130], spin coherence time [10], etc., has been proposed and demonstrated. Besides, for certain applications such as NV based markers in biology [43, 101] or NV based qubits in quantum information [5, 7, 62], controlling the photoluminescence signal of color centers in diamond is necessary.

The first technique uses the stimulated emission depletion (STED) [62, 60] to decrease the photoluminescence of NV color center and it has been used for the super-resolution imaging. In fact, STED technique involves two laser beams at different wavelengths: the usual one (green laser) exciting fluorescent emitters, and an additional one (red laser, STED-beam) depleting the emitter excited state by stimulated emission. This technique allows to modulate the photoluminescence of both neutral $NV^0$ and negative $NV^-$ charges color centers (See Chapter 1 for the definition of $NV^0$ and $NV^-$ color center in diamond.).

The second technique consists of applying a microwave field to switch the spin states of the ground level of a single spin associated to a single negatively charged $NV^-$ color center [70, 77, 78]. This technique allows to change the photoluminescence of a single emitter by a factor of 25 % and paves the way to study and manipulate the single electron spin resonance as it will be demonstrated in the second part of this dissertation.

In this chapter, we demonstrate another way to control the photoluminescence of NV color centers in diamond crystals, by exciting the NV color center by a high power pulsed infrared (IR) laser. This chapter is organized as follow. In Section 2, we present the experimental setup and samples used in this study. In Section 3, we demonstrate the modification of the photoluminescence of NV color centers in diamond by exciting them simultaneously with a green and an IR beams. Section 4 shows the IR pulsed excitation effect on the photoluminescence of NV color center in diamond bulk crystal. In Section 5, we demonstrate the mechanism of the photoluminescence quenching effect due to the IR excitation. We discuss about other possible applications and summarize the work in the last Section.

## 3.2   Experimental setup and sample preparation

### 3.2.1   Two-wavelength picosecond laser

The excitation laser used for all the studies of the IR effect is a "home-built" mode-locked $Nd:YVO_4$ picosecond laser constructed by the Institut d'Optique (LCFIO,

Palaiseau, France). The picosecond laser operates at 1064 nm with a repetition rate of 4.8 MHz and a pulse width of 16 ps. A KTP crystal ($4 \times 4 \times 5$ mm$^3$) is then used to generate second-harmonic wavelength at 532 nm as shown in Fig. 3.1(a). At the output of the laser system, two synchronized beams (532 nm and 1064 nm) are well superposed in space and in time, with corresponding average powers, $P_{532 \text{ nm}} \simeq 40$ mW and $P_{1064 \text{ nm}} \simeq 800$ mW.
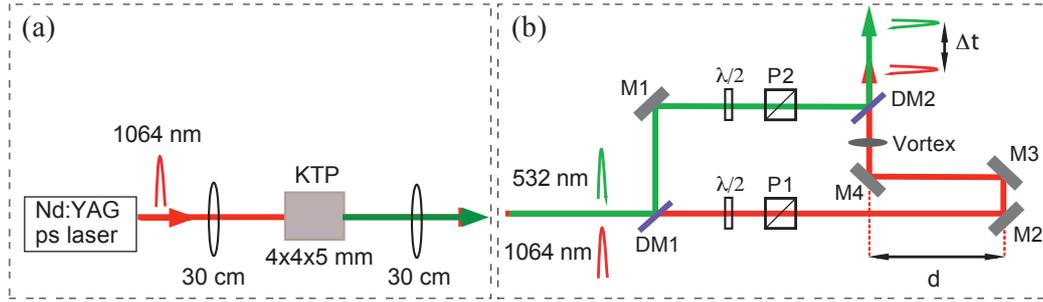


**Figure 3.1:** (a) Pulsed laser source used to excite the NV color centers in diamond. The original mode-locked Nd:VO$_4$ laser is frequency-doubled providing a synchronized and coherent two-wavelength excitation light source. (b) Experimental setup used to independently control the power and the phase of each laser beam and to vary the time delay between 532 nm and 1064 nm excitation pulses.

We then realized a setup, as depicted in Fig. 3.1(b), to independently control the power and the phase of each laser wavelength, as well as the time overlapping of two laser pulses. The two beams are first separated by a dichroic mirror (DM1) in order to independently control their powers, phases and polarizations, etc. To change the time overlapping of the green and IR pulses, we translate the two mirrors (M2 and M3) by a distance d. The IR pulse is then delayed by $\Delta t$ with respect to green pulse. Note that due to the limitation of the optical table, we can only translate the mirrors by a limited distance, d = 2.7 m, corresponding to a maximal delay, $\Delta t = 9$ ns. The two laser beams are then spatially combined by a second dichroic mirror (DM2) before being focused into the diamond sample. After this system, the powers of green and IR excitations measured in front of the objective are, $P_{532 \text{ nm}} \simeq 15$ mW and $P_{1064 \text{ nm}} \simeq 300$ mW.

### 3.2.2 Confocal microscopy setup

Optical excitation and detection of the photoluminescence of NV color centers are realized with a confocal microscope home-built setup, illustrated in Fig. 3.2. Two laser beams (green and IR) are focused into the diamond sample via a high numerical aperture (NA =1.4, oil immersion) objective (Obj.). The focus point is raster scanned relative to the sample with nanometer resolution, using a 3D-piezoelectric translation system. The photoluminescence of the excited NV center is collected by the same

objective, in opposite propagation way of the excitation. The photoluminescence is separated from the excitation beam by a polarization beam splitter (PBS). A standard confocal detection system consisting of two lenses and a pinhole of 100 $\mu$m-diameter is used to collect the luminescence coming from a sample volume of about 1 $\mu$m$^3$, ensuring the collection of light emitted by only one nanocrystal.
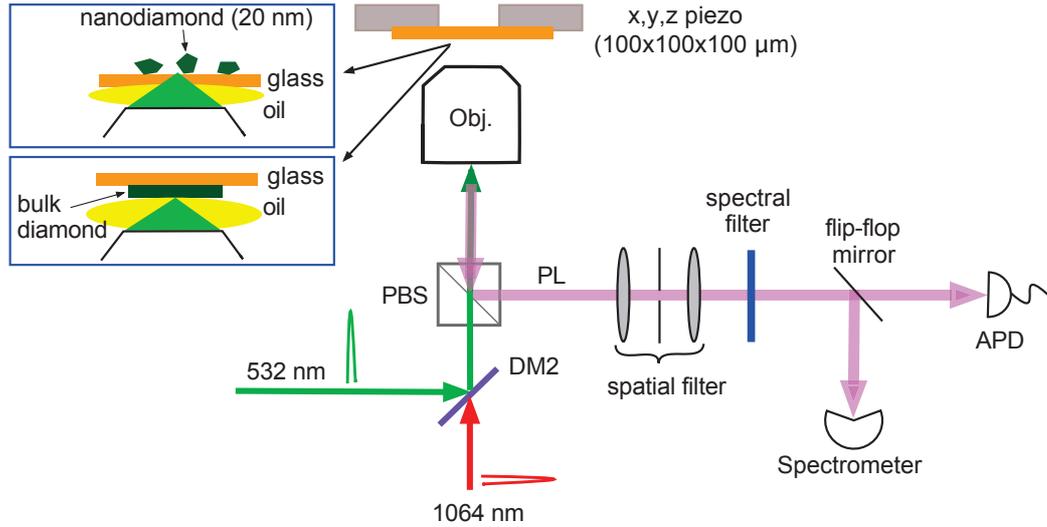


**Figure 3.2:** Experimental setup used to study the effect of IR excitation on the photoluminescence of NV color centers in diamond crystals. The NV color centers are excited, via an oil immersion microscope objective (Obj.), by a pulsed green laser and its photoluminescences are quenched by a pulsed IR excitation. The photoluminescence is collected by the same Obj. and spatially and spectrally filtered before being detected by an avalanche photodiode (APD) or by a spectrometer.

The excited NV color center emits a broadband photoluminescence (FWHM $\approx$ 100 nm) centered at 670 nm for NV$^-$ and at 590 nm for NV$^0$ color centers. The photoluminescence is spectrally filtered from the remaining pump lights by a long-pass filter with wavelength cut-off at 545 nm for avoiding the green excitation and by a short-pass filter (Schott KG5 filter) with wavelength cut-off at 850 nm for stopping the IR excitation. The photoluminescence is finally detected by a silicon avalanche photodiode (APD) operating in the single-photon counting regime and/or by a spectrometer working at low temperature for recording the photoluminescence spectra.

### 3.2.3  Sample preparation

The diamond nanocrystals (nanodiamonds) sample is prepared following a procedure described in [23], using a commercial source (MSY; Microdiamant). Starting from 50

nm diamond powders, the nanocrystals are irradiated with 40 keV He irradiation, followed by thermal annealing at 800°C, to produce efficiently NV color centers. These nanodiamonds contain statistically 50 % of $NV^-$ and 50 % of $NV^0$ color centers. We then annealed and extracted sub-20 nm diamond nanoparticles by multi-step annealing/centrifugation procedure. The nanodiamonds containing NV color centers are finally spin-coated on a quartz substrate. The characteristics of these nanodiamonds are studied and shown in previous chapter.

Alternatively, a type-Ib HPHT bulk diamond sample is also used to study the effect of IR pulsed excitation. In this case, NV centers, mostly negatively charged, are created from the initially embedded nitrogen impurities, by irradiation with a high-energy electron beam and annealing for 2 hours at 850°C. A density of about 200 NV color centers/$\mu m^3$ were created in [77]. All these samples are fixed in a sample holder which is mounted in a PZT translation system, as presented in previous paragraph, for this study.

## 3.3 Pulsed IR excitation: quenching of the luminescence of NV color centers

### 3.3.1 Effect of IR excitation on the luminescence of NV color centers in nanodiamonds

The nanodiamonds containing both $NV^-$ and $NV^0$ color centers are used for the first analysis of the IR excitation. The sample is first raster scanned with only an excitation beam at 532 nm (average power = 0.18 mW) to obtain a photoluminescence image of NV color centers. The result is shown in 3D-view in Fig. 3.3(a). Four bright spots, corresponding to four "nanodiamonds", are found and are numerized as A, B, C, and D. Note that in this work we don't have intention to study the single emitter and none of these four centers is single.

We then simultaneously excite these nanodiamonds with 532 nm (average power = 0.18 mW) and 1064 nm (average power = 100 mW) beams. The corresponding photoluminescence image of NV color centers are shown in Fig. 3.3(b). A clear diminution of the luminescent emission is observed for different nanodiamonds. Note that we also changed the polarization (linear at different directions or circular) of both green (532 nm) and infrared (1064 nm) beams, and the modulation of the luminescence signal remains the same.

Furthermore, by using a spectrometer to verify the emission spectrum of NV color centers, we found that the pulsed IR excitation quenches the photoluminescence of

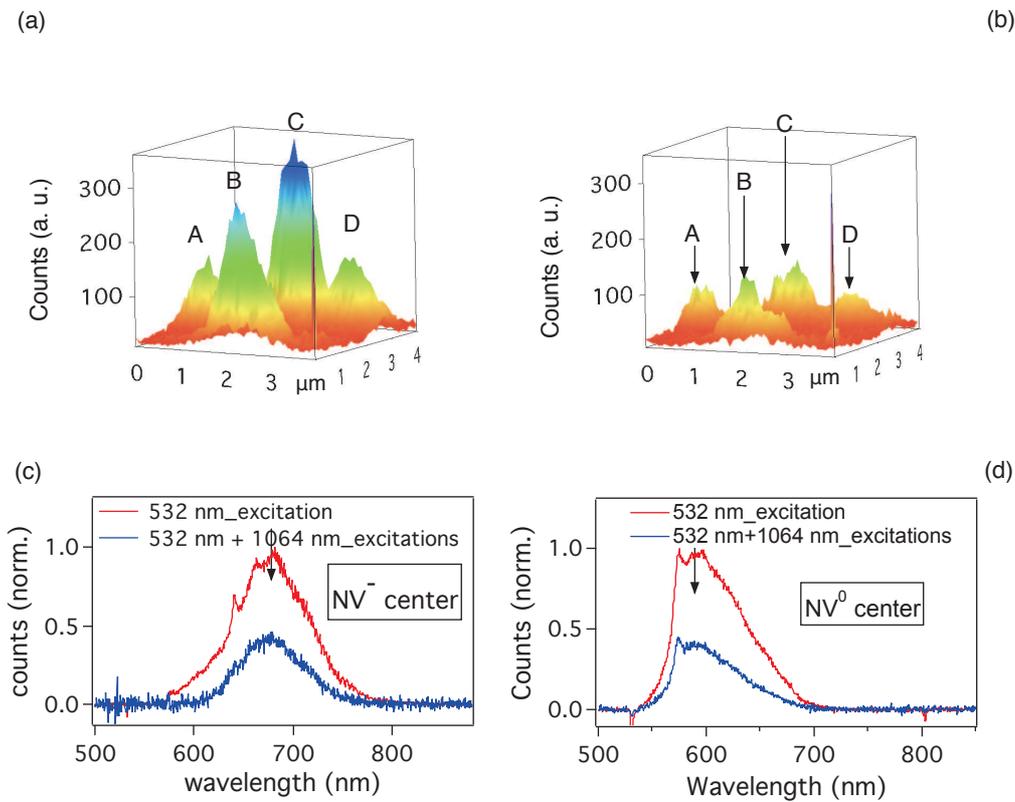**Figure 3.3:** Effect of pulsed infrared (1064 nm) excitation on the photoluminescence property of NV color centers in diamond nanocrystals. (a) Photoluminescence image obtained with only a 532 nm excitation. (b) Photoluminescence image obtained by simultaneous pulsed excitations at 532 nm and at 1064 nm. (c) and (d) Luminescence spectra obtained without and with infrared excitation for both charge states of NV centers.

both NV$^-$ and NV$^0$ color centers. Figures 3.3(c) and (d) show the photoluminescences spectra obtained without and with infrared excitation. A similar diminution quantity is observed for both charged types color centers.

We note that the photoluminescence quenching is only observed with IR pulsed excitation. Indeed, we have replaced the pulsed IR laser by a continuous IR laser, but no modulation of the photoluminescence is observed. Besides, by scanning the sample with only IR pulsed excitation, we didn't observe any photoluminescence emission of NV color centers. The IR excitation probably does not induce any direct modification of the NV color center, by either one-photon absorption or two-photon absorption [145, 142]. More investigation should be done in order to understand the mechanism of the IR pulsed excitation, and it will be presented in the next Sections.

### 3.3.2 Response time of the IR pulsed excitation

The effect of IR excitation on photoluminescence quenching is observed to be very fast and is a reversible phenomenon. Indeed, the photoluninescence is immediately quenched when the IR excitation is turned on and it recovers to the original level when the IR excitation is turned off, as shown in Fig. 3.4(a). The response time of the IR effect when the excitation is on or off is much shorter than the acquisition time of the detection system (e.g., acquisition time of the electronic system and the response time of the avalanche photodiode) and it cannot be determined by the experimental curve shown in Fig. 3.4(a). In order to determine the response time of the IR effect, we have used a technique of time correlation measurement. Figure 3.4(b) shows the decay of the photoluminescence with and without the IR excitation. To clearly observe the photoluminescence quenching effect, IR pulse is turned on after the green pulse by a delay of 3.1 ns. The photoluminescence is immediately quenched with a response time of about 740 ps. This response time is however similar to the response time of the detection system of the experiment, and it can be seen in the rising edge of the curve. We therefore believe that the photoluminescence quenching effect happens quasi-immediately after turning on the IR pulse and lasts for only during the IR excitation, i.e., IR pulse duration ($\approx$ 16 ps).

This IR pulsed excitation is therefore interesting for many applications requiring rapid response of the system, such as fast switching of NV color center in diamond based single photon source, or rapid optical super-resolution imaging. The later will be discussed in Chapter 3.
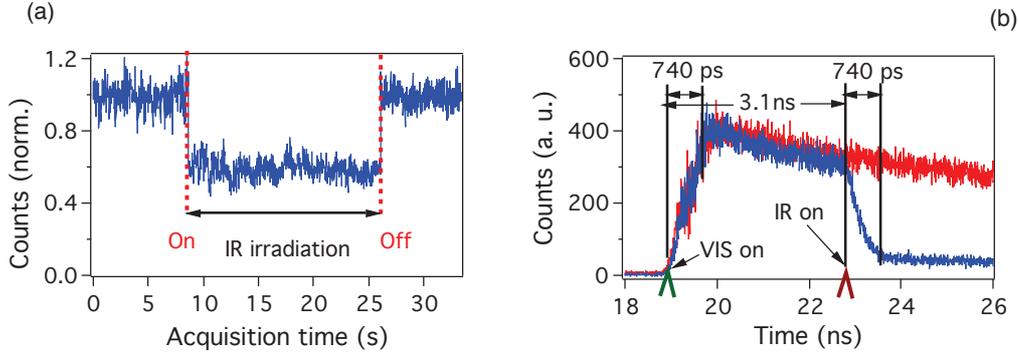
**Figure 3.4:** Quenching effect of the photoluminescence of a nanodiamond containing NV color centers. (a) Photoluminescence intensity is quenched when the IR beam is turned on and it rapidly recovers to its original level when the IR beam is turned off. (b) Decay of the photoluminescence of NV color centers as a function of green and infrared excitations. The infrared excitation is delayed by 3.1 ns with respect to the green excitation. A typical response time of the photoluminescence due to the infrared excitation is about 740 ps, which is however extended by the response time of the detection system.

### 3.3.3   Time delay dependence of infrared excitation quenching effect

As mentioned above, the IR pulsed excitation obviously don't have direct interaction with NV color center. However, the recent study [115] demonstrated that NV color center also luminesces in infrared range, i.e., at 1046 nm, due to the transition between two metastable states. We wonder if the IR pulsed excitation, i.e., 1064 nm, can be absorbed by this transition, and consequently modifies the photoluminescence of the NV color center. In fact, the transition from the excited level to the metastable level is only efficient if the NV color center is excited with a green laser at high power (> 1 mW), i.e., at saturation level. However, we observe that the IR excitation effect is more evident with low green excitation power, as low as 50 $\mu$W. Besides, the lifetime of the metastable level is very long, of about 300 ns, in contraste to very short response time of the IR excitation effect. It is therefore difficult to explain the effect of the IR excitation by the metastable levels of the NV color center.

   To clarify this point, we propose an experiment by delaying the IR pulses excitation with respect to green pulses excitation and measuring the diminution of the photoluminescence. To delay the IR pulses, we use the setup shown in Fig. 3.2(b). By translating the two mirrors by a distance d, the IR pulse is delayed by $\Delta$t ($\Delta$t = 2d/c, where $c$ is the speed of light in the air) with respect to green pulse. The green and IR excitations powers are kept constant for all measurements, P$_{532\ nm}$=180 $\mu$W and P$_{1064\ nm}$=100 mW.

   Figure 3.5(a) shows that the quenching effect depends on the delay between green

and IR pulses. It is obvious that when IR pulse goes after green pulse, the application of IR pulses quenches the PL intensity of NV color center. The photoluminescence quenching is maximal if the delay is about 1 ns and it is weak with a delay of 9 ns. Figure 3.5(b) shows the IR quenching effect as a function of the delay. The diminution ratio of PL intensity is demonstrated to be decreased with the delay and the effect of IR excitation on the luminescence of NV color center is only valid if the delay between green and IR pulses is shorter than 30 ns. The continuous curve is the monoexponential fit showing a time decay of about 10.2 ns of the quenching rate, which is very close to the photoluminescence decay lifetime of the NV color center (about 11 ns).
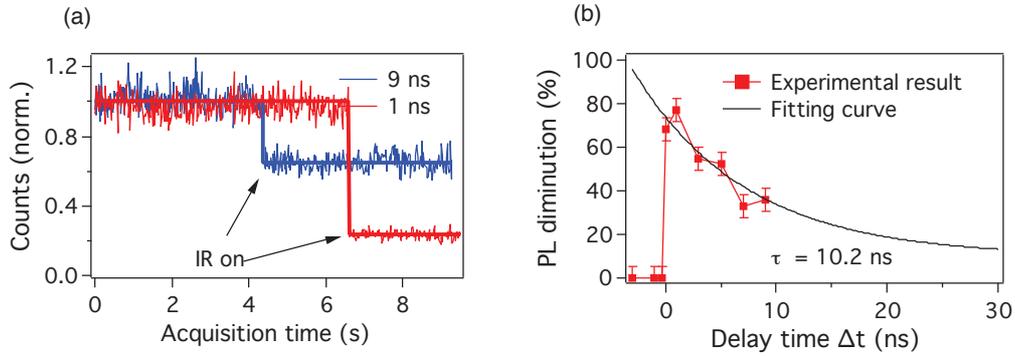


**Figure 3.5:** (a) Photoluminescence diminution obtained by $\Delta t = 1$ ns and $\Delta t = 9$ ns. (b) Photoluminescence quenching as a function of the time delay, $\Delta t$. The black curve is the monoexponential fit showing a time decay of the photoluminescence of about 10.2 ns, similar to the decay lifetime of the NV color center.

What happens if the delay is negative, i.e., the IR pulse is exposed before the green pulse. In fact, with a large negative $\Delta t$, we don't see any IR excitation effect on the photoluminescence of NV color center. Hereafter, we call the negative delay by $\delta t = -\Delta t$. In order to observe the IR effect with IR pulses which are slightly before green pulses, we realize an experimental setup shown in Fig. 3.6. Two laser beams (green and IR) are superposed through all their propagation. We assume that the green and IR pulses have no time-delay before entering into the delaying setup. According to the confocal setup, as shown in Fig. 3.2, a minimum delay ($\delta t = 6$ ps) has been arbitrarily introduced. Additional weak delay of few picoseconds is introduced by using several glass cubes (SF2). Indeed, since the difference of the refractive index of the used glass cubes for the 532 nm-wavelength and 1064 nm-wavelength is about 0.2645, each glass cube of 25 mm-length delays the green pulses by a 6.6 ps with respect to IR pulses.[1]

With only the minimum delay due to the glass cube of the confocal setup (6 ps), a decrease of photoluminescence is observed, though the ratio is not very high. The

---

[1]The IR light can be anytime removed from the co-propagating green beam by introducing a piece of thin KG5 filter.
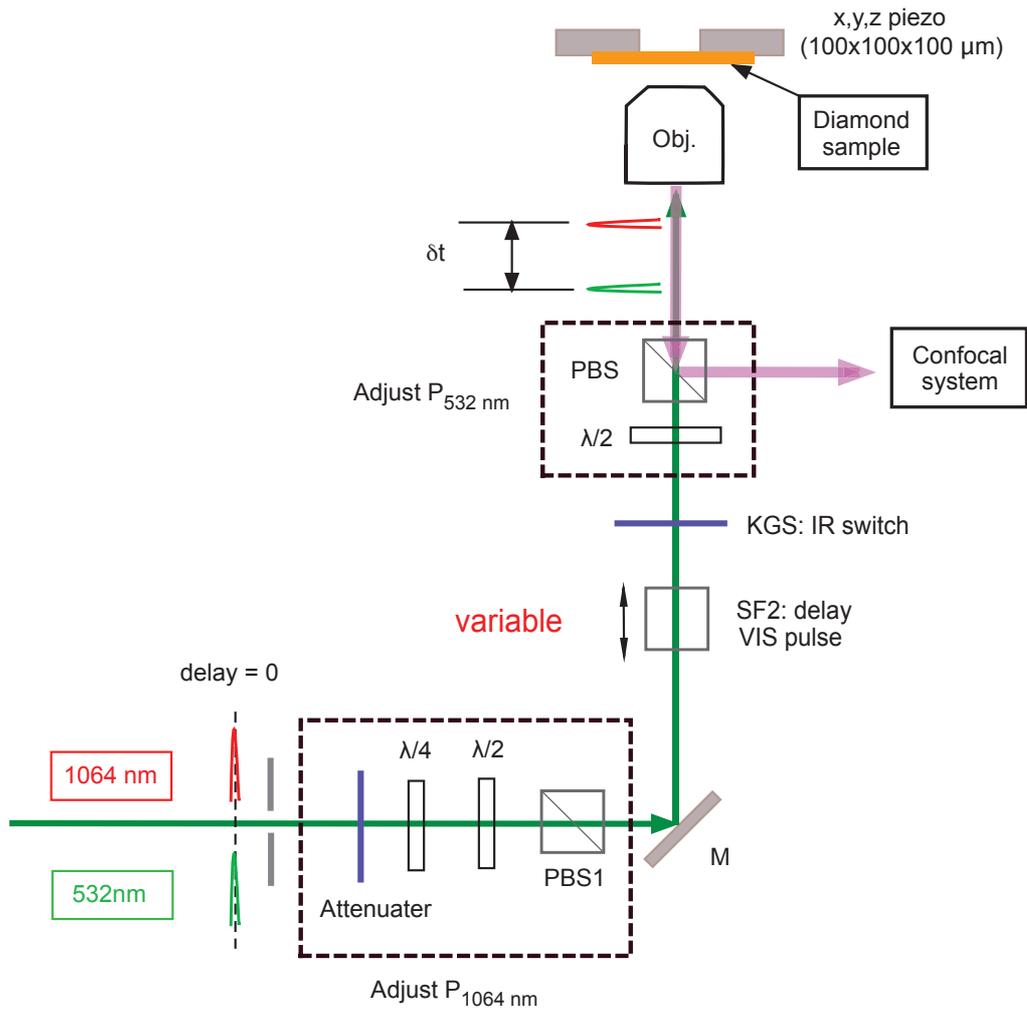
**Figure 3.6:** Experimental setup used to study the PL quenching effect due to pulsed IR excitation. The IR pulses are exposed slightly before green pulses by using several SF2 cubes.

IR effect decreases as a function of $\delta t$ is shown in Fig. 3.7. The IR pulse almost has no effect on the photoluminescence of NV color centers when it is irradiated by $\delta t = 17$ ps before green pulse. In fact, the delay of 17 ps is almost equal to the IR pulse duration. As we known that the diamond is a good thermal conductor with a thermal conductivity of 900-2,320 W·m$^{-1}$·K$^{-1}$. Due to such good thermal conductivity, the heating induced by IR pulses disperses so fast, well before the arrival of the green pulse.
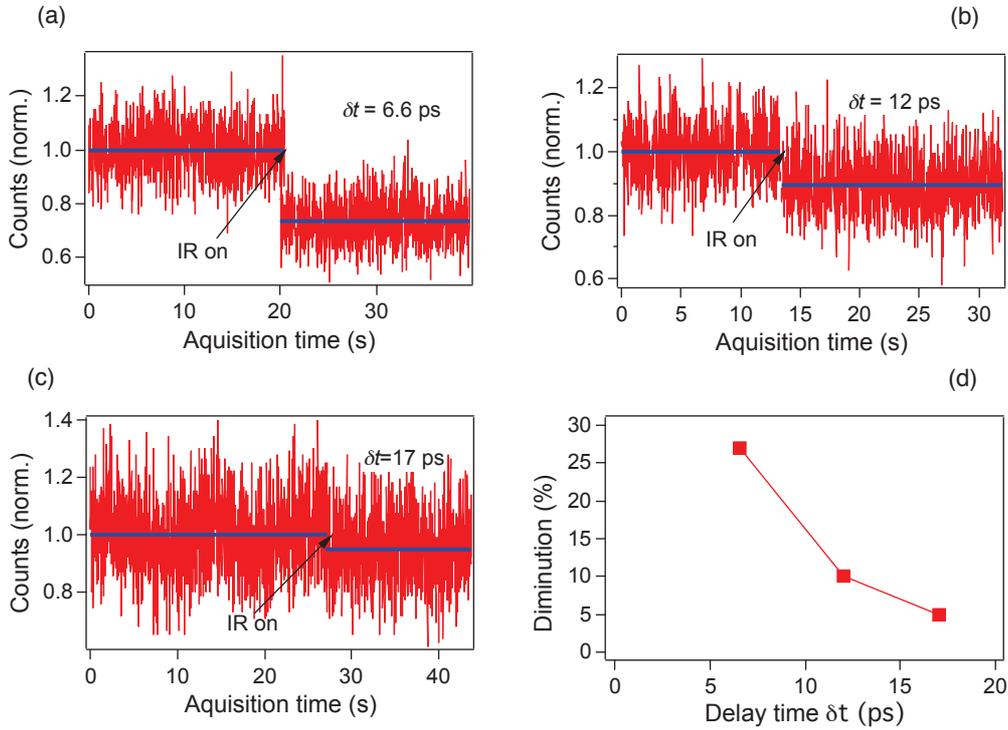


**Figure 3.7:** IR effect on the photoluminescence of NV color center observed when the IR pulses are exposed before VIS pulses. The excitation moment of the IR pulses and the delay time are indicated in each figure. With a delay of 17 ps, no IR effect can be observed. (d) The photoluminescence modulation versus delay time. The solid curves in Figure (a-c) represent the average values which are used to calculate the diminutions.

These obserations again confirm that the response time of the IR pulsed excitation is about the pulse duration. These results totally eliminate the hypothesis that the IR excitation induces the re-absorption of the metastable level, moreover, this suggests that the photoluminescence quenching effect is due to the modification of the excited level of the NV color center. The interaction, direct or indirect, between the IR excitation and the excited levels of NV color center will be demonstrated in the next Section.

### 3.3.4   Dependence of photoluminescence quenching effect on IR excitation power

In order to use this IR pulsed excitation effect for different applications, it is iimportant to know what is the minimum power of the IR excitation to induce the modification of the luminescence of NV color centers and what is the maximum diminution of the photoluminescence. We have realized the measurement of the luminescence modulation as a function of both IR and green irradiating powers. The result shows that the quenching effect was not influenced much by the green power change, though lower green power allows to have better modulation. Whereas the change of IR power varies strongly the modulation of the luminescence of NV color center. Figure 3.8(b) shows the normalization of the luminescence signal as a function of the IR power. A threshold of about 5 mW is indicated, and the best modulation is about 73 % when $P_{IR}$=116 mW as shown in Figure 3.8(a).
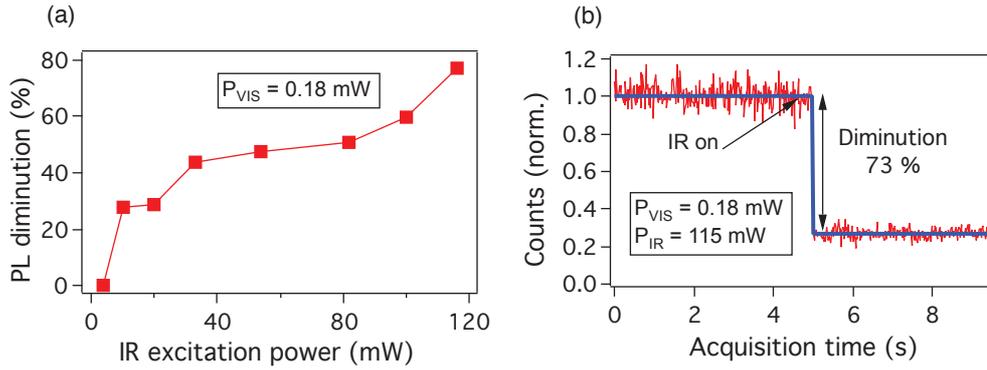


**Figure 3.8:** Photoluminescence quenching effect obtained by different IR excitation powers. (a) Normalized diminution of the luminescence as a function of IR power. (b) Photoluminescence as a function of time obtained without and with IR excitation, showing the best modulation.

Additionally, we observed that when we use high IR excitation power and for a long exposure time, the photoluminescence signal of NV color centers is unstable as shown in Figure 3.9. Moreover, some of the luminescent centers irreversibly faded after several scans with strong IR light : a bleaching effect of high IR excitation power. This indicates that the strong IR excitation not only quenches the PL of NV color centers but also makes them blinking or even "kills" them under certain conditions. In combining with the observations shown in above, we propose that the PL quenching effect due to IR excitation is caused by the thermally induced variance of the environment around NV color centers. To clearify this point, we propose to study the IR excitation effect on the PL of NV color centers in a bulk diamond in which the NV color center is surrounded by a large area of diamond material. If the IR excitation induces some
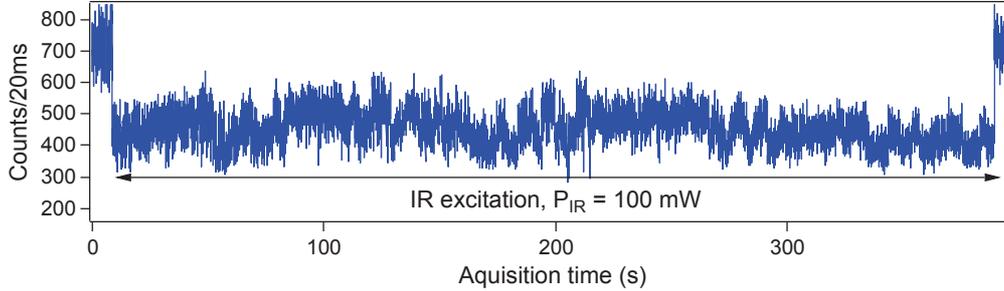
**Figure 3.9:** IR quenching effect at high IR excitation power. The photoluminescence signal is unstable as a function of excitation time.

changes of the environment around NV color centers, we should have different results.

## 3.4 Infrared excitation effect on PL of NV color centers in a bulk diamond

From the study of IR excitation effect of NV color center in nanodiamond, we know that the IR effect happens only when the IR pulses go after the VIS pulses, the unstable character of NV color center under strong IR irradiation illustrates that the IR quenching effect is probably caused by the thermally induced variance of the environment around NV color centers, such effect are supposed to be much more obvious on bulk diamond compared to nanodiamonds.

For the first test of the IR effect on the PL of NV color center in bulk diamond, the laser beam was focused slightly out of the sample surface. By switching on and off the IR beam, the modulation of the photoluminescence is immediately observed, similar to the observation on nanodiamonds. Figure 3.10 shows the IR effect as a function of the IR power. However, the modulation is not so high as in the case of diamond nanocrystals, even at very high IR power of about 360 mW. This doesn't mean that the effective intensity is also high, because the focusing point is out of the diamond surface. This is only equivalent to an excitation of a large quantity of NV color center.

Surprisingly, when we optimized the focusing point on the sample surface, the diamond in the focusing area is burned, indicating by an increase of the detected photon number from about $10^4$ counts per second to about $10^6$ counts per second. This photons are not related to the photoluminescence of NV color centers, but rather to emission of burned carbon atoms.

The micro-explosion effect is observed with even at very low IR excitation power.
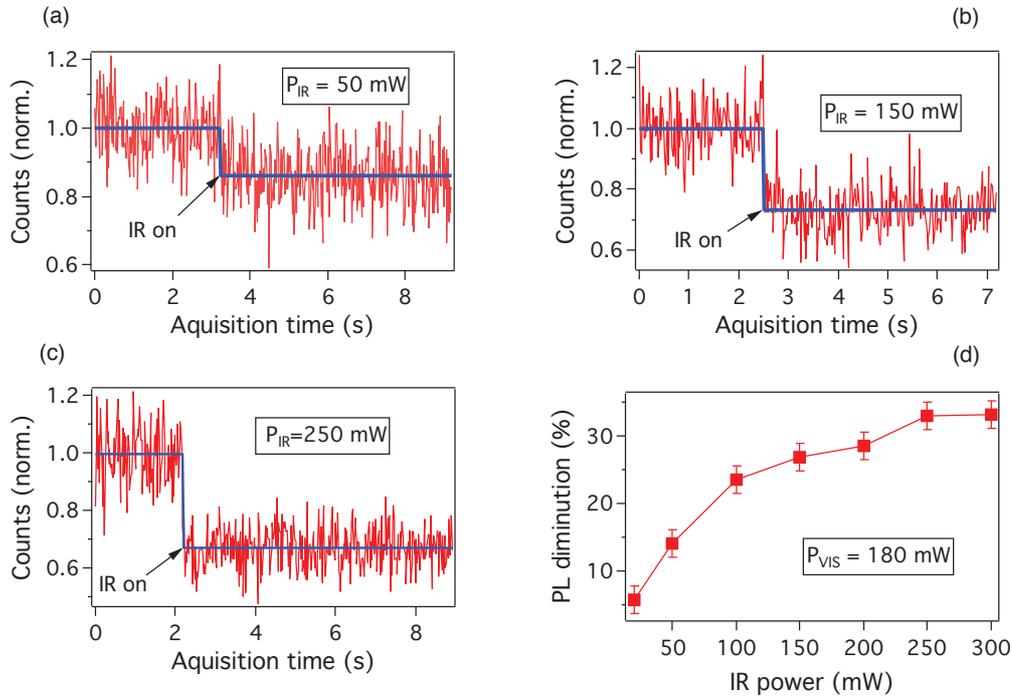
**Figure 3.10:** IR effect on the photoluminescence of NV color centers in bulk diamond. The results are obtained by focusing the IR beam slightly out of the surface of diamond sample. The effect is similar to the one observed with nanodiamonds.
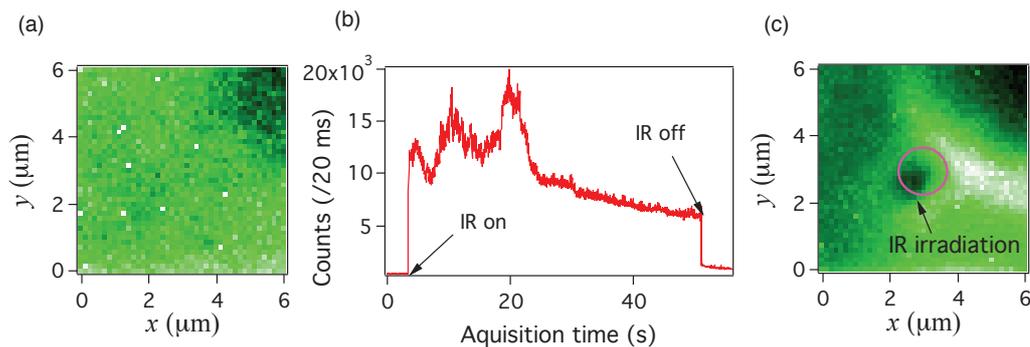


**Figure 3.11:** IR effect on the photoluminescence of NV color centers in a bulk diamond. The IR pulses burn the diamond surface at very low power (40 mW). The burning effect is immediate and no diminution of photoluminescence signal is observed. (a) and (c): scanning pictures obtained before and after 40 mW IR irradiation. (b) photoluminescence as a function of the acquisition time. The moments of turning on and off of the IR pulses are indicated.
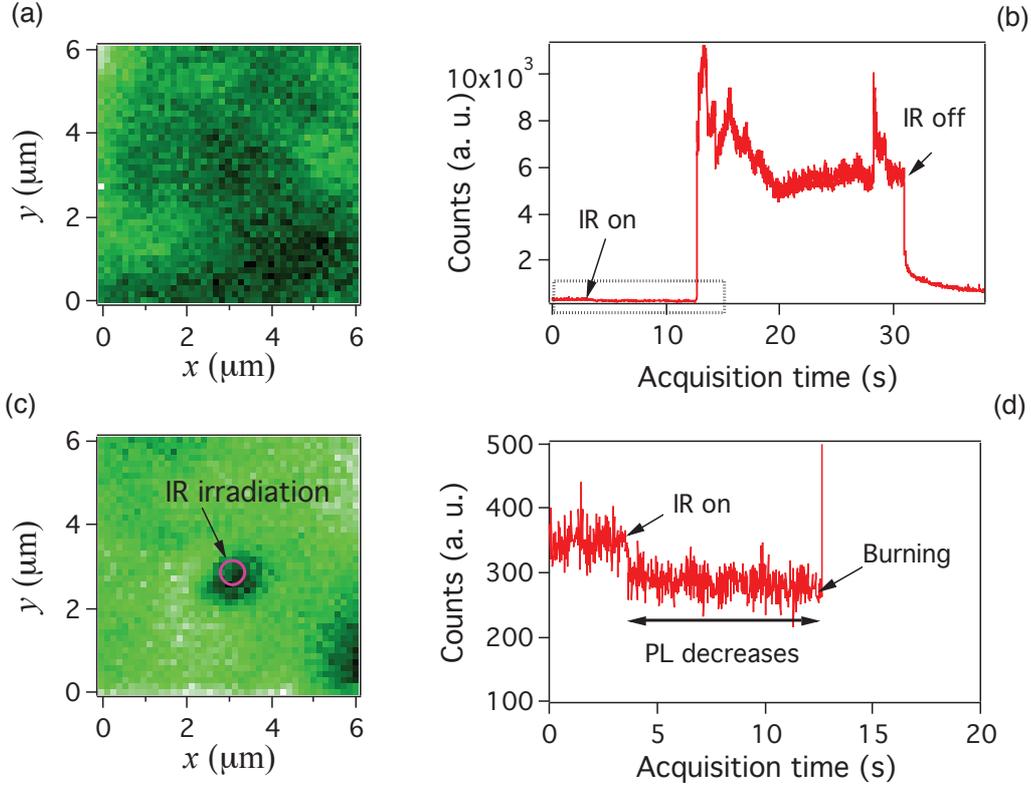
**Figure 3.12:** IR pulsed excitation effect on the photoluminescence of NV color centers in a bulk diamond crystal. (a) Photoluminescence image obtained by only a 532 nm excitation. (b) Photoluminescence intensity obtained with on and off of IR excitation. A burning effect is observed. (c) Zoom in of the photoluminescence intensity curve obtained in the beginning of the IR excitation, showing the thermal effect of the high intensity IR excitation: i) photoluminescence signal first decreases, as in case of nanodiamond, and then rapidly increases due to the explosion effect. (d) Photoluminescence image obtained after burning effect due to IR excitation. A black spot is observed at focusing point of the IR excitation beam.

For the excitation power larger than 40 mW, we can observe the burning effect at every where of the sample surface, as shown in Fig. 3.11. When the IR power is decreased to 30 mW or 20 mW, this effect is sensitive to the sample surface quality, the focusing position, and also the exposure time. It is quite interresting to study the IR excitation effect at this range of IR power and we may find out the relationship of the burning effect and the photoluminescence quenching effect.

Figure 4.8 shows the IR effect with $P_{IR} = 30$ mW. At this power, the burning effect is not immediately obtained for all the tested areas. In particular, for some areas, a decrease of photoluminescence is observed before burning. The instant between the $IR_{on}$−moment and the burning varies from area to area. This experiment demonstrates two behaviors of the IR excitation, PL quenching and diamond burning, which

is originally induced by the thermal effect due to the high peak intensity of the IR excition. The threshold of burning effect is experimentally determined to be about 30 mW. At lower power, for example 20 mW, we still can observe the burning effect, but less evident, and for that the PL quenching effect is dominant.

This observation confirms a relationship between two effects, micro-explosion and photoluminescence quenching, as a consequence of IR high excitation peak intensity. It is worth to note that the burning effect in diamond due to high excitation power at 1064 nm wavelength was also observed and used for fabrication of microstructures [131, 146]. The micro-explosion effect is due to five-photon absorption of diamond matrix at high peak intensity of 1064 nm excitation. This absorption induces heating of diamond crystal, melting and vaporization. The photoluminescence modulation is therefore due to the thermal effect of diamond crystal at high intensity pulsed excitation (but below the burning threshold) which modifies the energy diagram of the NV color center embedded inside the diamond matrix.

## 3.5 Model of photoluminescence quenching effect due to IR pulsed excitation
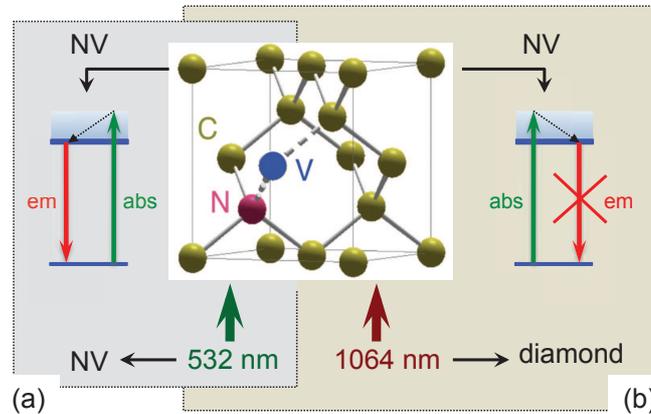


**Figure 3.13:** Proposed mechanism of the photoluminescence quenching effect of NV color centers due to the IR excitation. (a) NV color center in diamond crystal absorbes only 532 nm light and emits luminescence. (b) NV color center absorbes 532 nm light while diamond crystal absorbes 1064 nm via multi-photon absorption process. The later is shortly (during pulse duration) ionized and it affects (quenching) the photoluminescence of NV color center.

We can conclude that the IR excitation does not have direct interaction with NV color center. The thermal effect of diamond host induced by IR excitation high peak intensity is the origin of the modulation of the photoluminescence of NV color centers.

Furthermore, due to the high peak intensity of very short IR pulses, the local temperature of diamond crystal rapidly increases to very high value and also rapidly decreases to room temperature at the end of the pulse duration, resulting in a rapid modulation of the photoluminescence of the NV color center, as shown in section 3.3.3.

The mechanism of the photoluminescence quenching is summarized in Fig. 3.13. NV color center in diamond crystal absorbs only green light and emits photons. Diamond crystal absorbs light at 1064 nm via multi-photon absorption process, which then induces change of energy level of NV color center, consequently quenches the photoluminescence emission. This mechanism allows to explain all above experimental observations, namely i) there is no observation of IR effect with a continuous IR excitation, because there is no multi-absorption effect, ii) the photoluminescence quenching effect is observed for any kind of color center, because the IR excitation does not have direct interaction with color center but with diamond host, iii) there is a dependence of photoluminescence quenching rate on the time delay between green and IR excitation pulses, because of the short time thermal effect, etc.

## 3.6   Conclusions

We have demonstrated the effect and the mechanism of the pulsed infrared excitation on the photoluminescence of nitrogen-vacancy color centers in diamond crystal. By exciting the diamond sample with a high peak intensity pulsed IR beam, diamond crystal is locally annealed due to the multi-photon absorption of the diamond crystal, leading to the change of the energy level of the NV color centers embedded inside the diamond. Consequently, the photoluminescence of NV color centers is quenched to almost 80 %, depending on the IR excitation intensity. The quenching effect is demonstrated reversible without and with IR excitation, with a typical response time of hundred picoseconds, for which the measurement is limited by the response time of the detection system. The rapid photoluminescence quenching with very sort time response is useful for different applications, based on the use of color centers in diamond. The use of IR pulsed excitation for increasing the resolution of the optical imaging of NV color center in diamond will be demonstrated in Chapter 4. Other applications such as rapid switching of NV color center based single photon source and tunable photonic bandgap device based on diamond photonic crystal, could be also envisageable using this IR excitation effect.

# Super-resolution optical imaging of NV color centers in nanodiamonds

**Contents**

## 4.1 Microscopes allowing nano-imaging

### 4.1.1 Introduction

The microscope is one of the most popular tools for the modern science. It enables us to look into the microscopy world as small as molecules and atoms. A very important parameter of the microscopy is the resolution, which is defined as the minimum distance of two small objects that can be distinguished during the imaging process. Up to now, some techniques such as the atomic force microscope (AFM) [**?**], the scanning near field optical microscope (SNOM) [41], the transmission electron microscope (TEM) [138] and the scanning tunneling microscope (STM) [19] are able to resolve single atoms. However, all these techniques require specific sample surface, and can be applied for particular cases such as 1D and 2D structure. Most of them can be used only for nano-imaging of sample, which are placed in vicinity of the scanning instruments.

The far field optical microscope remains an important in diverse fields such as molecular and cell biological studies [79, 110], due to its non-invasive property, applicable to living cells and fluorescence labeling distinguishability. Moreover, the unique advantage of being a non-contact process in a flexible setup that can operate in air, vacuum or liquid environment makes the optical microscopy to be a very attractive tool for micro-fabrication and data storage [57, 136, 76]. The main drawback of conventional optical microscopy is its limited resolution due to the diffraction limit. The optical resolution is of the order of the wavelength of the light used for illumination. Overcome the diffraction limit and achieving the super-resolution become an important task in order to apply optical microscope for nanoscience. Super-resolution imaging nowadays is one of the most popular research topics in the far field optical microscopy domain.

The diffraction limit was first described by E. Abbe a hundred years ago [1]. It is expressed as $d = \frac{\lambda}{\text{NA}} = \frac{\lambda}{n \sin \alpha}$, where $\lambda$ is the wavelength of light and NA is the numerical aperture of the objective, defined as the sine of the half aperture angle $\alpha$ multiplied by the refractive index of the medium filling the space between the cover glass and the front lens $n$. In this chapter, we develop different techniques to improve the resolution of a confocal optical microscope. Our aim is to improve the photoluminescence image of NV color centers in diamond. This is quite important for different applications based on the use of NV color centers, such as NV based biomarkers or quantum information.

## 4.1.2 Resolution limit of far field optical microscopy

In order to achieve high resolution imaging, a high numerical aperature (NA) objective lens (OL) is often used. In an usual case, the illumination beam has an uniform phase distribution and an gaussian intensity distribution. We call the OL in this case "circular OL", according to Ref. [21, 56, 124], in order to distinguish with other cases treated later.

In order to determine the intensity distribution at the focusing point of such high NA OL, *i.e.*, the optical resolution, we adopt a simplest theory by using the non-paraxial scalar Debye approximation. The intensity distribution at the focus-region of an aberration-free high-aperture circular lens, $h(v, u)$, i.e., the 3-D amplitude point spread function (APSF) in image space is given by [55]:

$$h(v,u) = \exp[-\frac{iu}{4\sin^2(\alpha_0/2)}] \int_0^{\alpha_0} P(\theta) J_0(\frac{v\sin\theta}{\sin\alpha_0}) \exp[\frac{iu\sin^2(\theta/2)}{2\sin^2(\alpha_0/2)}] \sin\theta d\theta, \quad (4.1)$$

where $J_0$ is the zero-order Bessel function, $\theta$ is the angle of convergence of a ray, $\alpha$ is the semi-aperture angle, and $P(\theta)$ is an apodization function or the pupil function of the circular OL. For a common case, we have:

$$P(\theta) = \cos^{1/2}\theta. \quad (4.2)$$
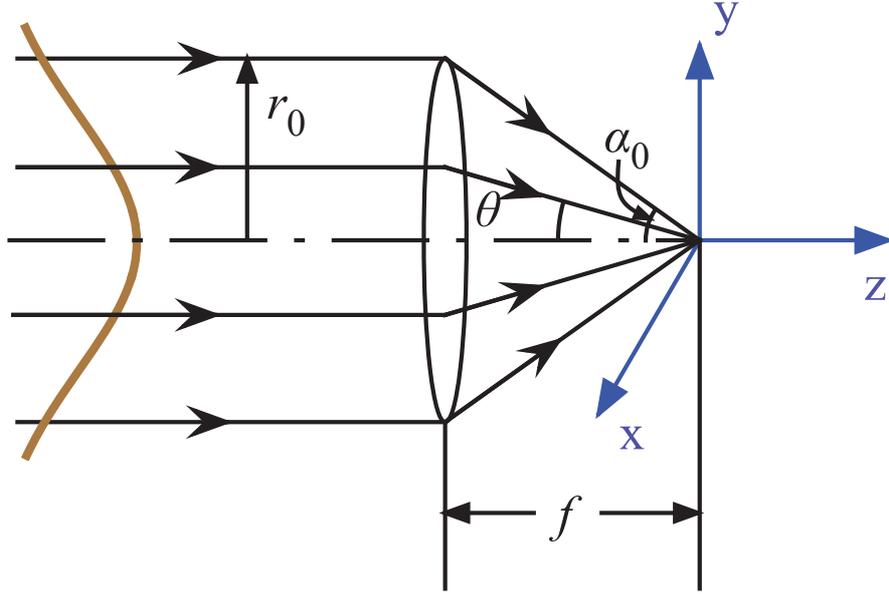
**Figure 4.1:** Focusing configuration of an OL. The origin of the coordinate system is placed in the geometrical focal point. The incoming wave propagates in $z$-direction.

The sine condition means that the imaging system has a two-dimensional (2D) transverse space-invariance. Variables $v$ and $u$ in Eq. 4.1 are the transverse and axial optical coordinates, respectively, defined as:

$$v = \frac{2\pi}{\lambda} r \sin \alpha_0, \tag{4.3}$$

$$u = \frac{8\pi}{\lambda} z \sin^2(\alpha_0/2), \tag{4.4}$$

where $r$ and $z$ are the real radial and axial coordinates in the image space, and $\sin\alpha_0$ is the numerical aperture of the objectives in the image space. $\lambda$ is the wavelength of the incident light. By replacing the $v$ and $u$ in Eq. 4.1 with Eq. 4.3 and Eq. 4.4, the complex amplitude of a monochromatic plane wave of wavelength $\lambda$ after being focused by a circular lens with aperture radius $r_0$, focal length $f$, and a pupil complex transmittance $P(\theta)$ is expressed as:

$$A_{\text{circular}}(r, z) = \frac{2\pi i}{\lambda} \int_0^{\alpha_0} P(\theta) J_0(kr \sin \theta) \times \exp(-ikz \cos \theta) \sin \theta d\theta, \tag{4.5}$$

where $k$ is the wave number

$$k = \frac{2\pi}{\lambda}. \tag{4.6}$$

(a)

(b)

1.0

D

-0.8    r ($\mu m$)    0.8

Intensity
distribution

$r_0$

-3

-2

-1

0.5

1.0

z ($\mu m$)    0

Z

1

2

3

(c)

0.9

0.8

D ($\mu m$)    0.7

0.6

0.5

—— Lateral (D)
- - Axial(Z)

10

8

6    Z ($\mu m$)

4

0.8    1.0    1.2    1.4
Numerical Aperture
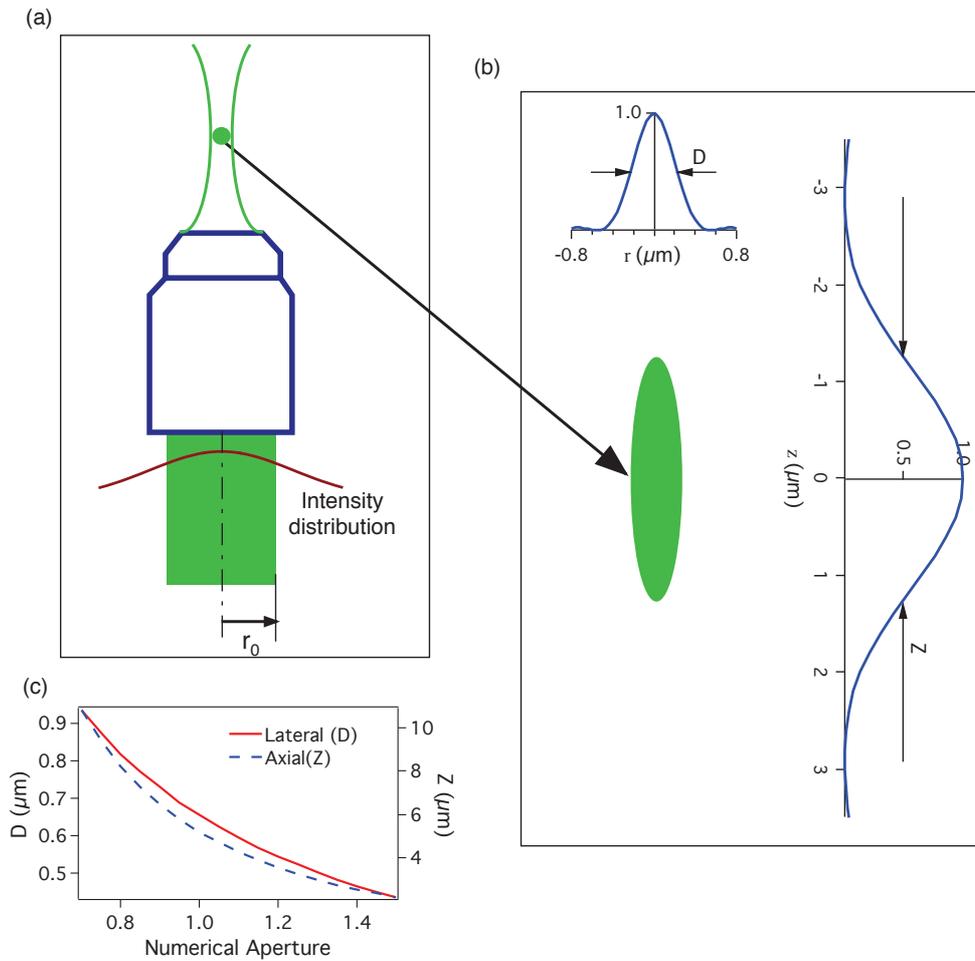
**Figure 4.2:** Calculation of intensity distribution of the focus region of a high NA circular OL. (a) Illustration of a gaussian beam focused by an objective lens. (b) Zoom in of the focusing point with corresponding transverse and longitudinal intensity distribution. D and Z are lateral and axial diameters of the focal spot, calculated △ FWHM of the distributed intensity. (C) Calculation of D and Z as a function of NA. The circular OL is supposed immersed in oil with n=1.515, and the illumination wave length $\lambda = 532$ nm.

The intensity distribution and the focusing point size of the OL can be calculated by using equation 4.5. In our study, $\lambda = 532nm$ corresponding to the wavelength of the excitation laser. The circular OL is supposed to be immersed in oil with n=1.515. Figure 4.2 depicts the focusing point size of the objective lens of different NAs. A higher numerical aperature OL can focus the light to a smaller size and increase the resolution. The aspect ratio (Z:D) of the focusing point is about 5. The transverse size of the focusing point is in the order of the excitation wavelength of the illumination beam.

## 4.2 Resolution improvement with an annular shaped illumination beam

As discussed in the last section, one has the common sense that the resolution of optical microscopy depends on the dimension of the focusing area, hence decreasing the size of the focusing area is the most direct way to increase the optical resolution. The annular beam is a simple way commonly used to increase the lateral resolution of the far field confocal microscope [65, 147].

For an annular shaped beam with $r_1$ as the radius of the annular mask (Figure 4.3 (a)), the complex amplitude distribution of the focusing area of a monochromatic plane wave can be written as [76]:

$$A_{\text{annular}}(r, z) = \frac{2\pi i}{\lambda} \int_{\gamma}^{\alpha} P(\theta) J_0(kr \sin\theta) \times \exp(-ikz \cos\theta) \sin\theta d\theta, \qquad (4.7)$$

where $\gamma = \tan^{-1}(\varepsilon \tan\alpha)$ with $\varepsilon = r_1/r_0$. The calculation result shows that the full width of half maximum (FWHM) of the focusing point of an annular beam is smaller comparing with the one of a gaussian beam (Figure 4.3b). It means that we can increase the resolution of the OL simply by transforming the pattern of the illumination beam, this is an economical way to increase the optical microscope resolution. The circular amplitude mask stops the central part of the gaussian beam from arriving to the objective lens. Consequently, it causes power loss of the incident light. Figure 4.3 (c) demonstrates the size reduction and transmission ratio as a function of the annular mask size. This problem can be solved with a loss-free optical system as shown in Figure 4.4 [68]. The incident beam from a light source is made into an annulare beam by a combination of a convex conical mirror 1 and a concave conical mirror 2.

From the calculation above (Figure 4.3 (c)), one can figure out that by using an annular beam, the focusing point shrinks in transverse direction. Hence it can be used to increase the resolution of 2D optical imaging. To demonstrate this technique, NV color centers associated with diamond nanocrystals which are spin coated on a quartz
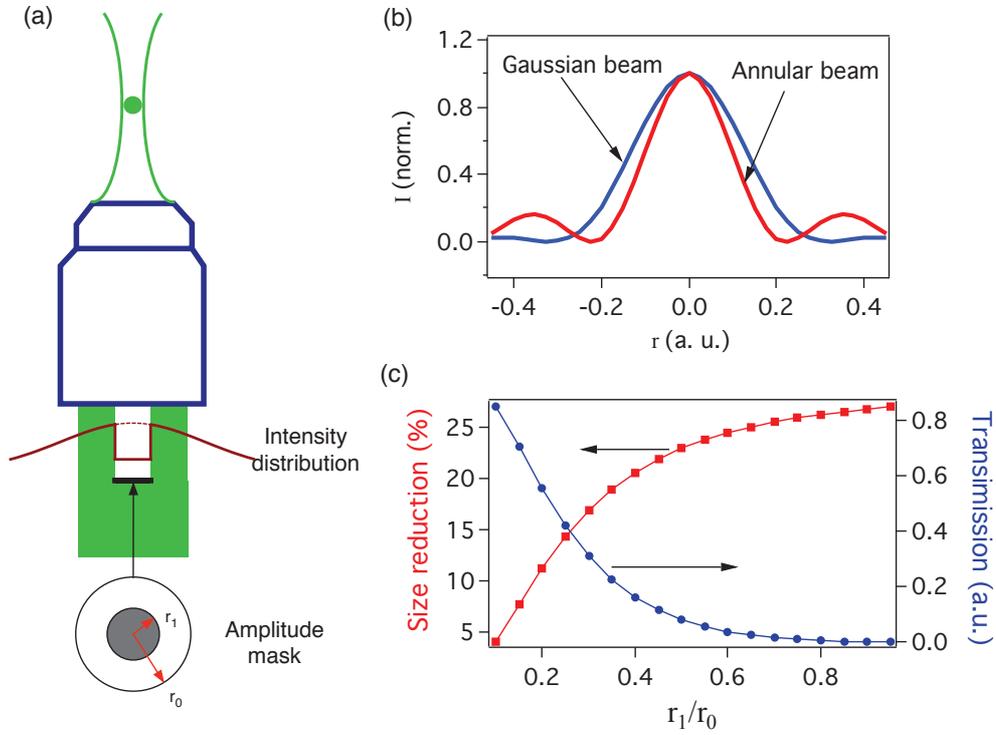
**Figure 4.3:** Calculation of intensity distribution of the focus region of a high NA OL using an annular beam. (a) A gaussian beam with the central part blocked by a circular amplitude mask of radius $r_1$ forms an gaussian beam; Figure (b) depicts the transverse intensity distribution of the focusing point of an annular beam and a circular beam, the FWHM of focusing point of an annular beam is smaller comparing with the one of a gaussian beam. (c) Calculation of the size reduction and transmission ratio as a function of the mask size.
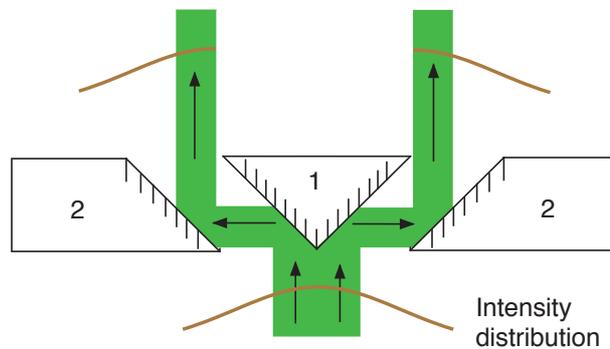


**Figure 4.4:** A loss free optical system for making an annular beam.

substrate are used as photoluminescence sources. A standard scanning confocal setup is used for sample imaging (See Chapter 1). In this work, a 532 nm CW laser is focused on to the sample through high aperture air objective lens (NA=0.95) to excite NV color centers. The photoluminescence light from NV color center is collected by the same objective lens, and detected by an avalanche photodiode. A transparent plastic paper with a designed black spot printed on it (Figure 4.3(a)) is placed in the excitation light path in front of OL to obtain an annular beam. In this experiment, $r_0 = 3$mm, $r_1 = 1.2$ mm. Figures 4.5(a) and 4.5(b) depict the photoluminescence images obtained with a gaussian beam and an annular beam, respectively. Figure 4.5(c) shows the profile of the NV center emission spot, scanned with these two kinds of excitation beams.
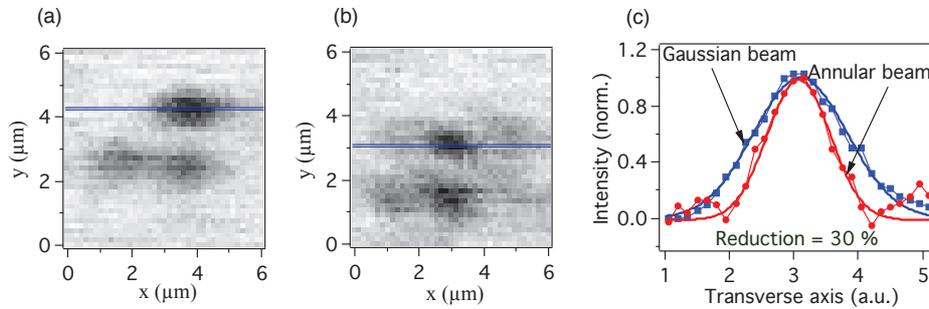


**Figure 4.5:** Super-resolution with an annular beam. Photoluminescence scanning image obtained with a gaussian beam (a) and with an annular beam (b). (c) Profile of the photoluminescence spot of a NV color center corresponding to the lines in (a) and (b).

A 30% higher resolution in transverse direction comparing with a circular beam can be achieved by an annular beam. This technique is not only suitable for optical imaging but also for microelectronics industries, such as marking, drilling, annealing and surface modification. Furthermore, one has to consider that an increase in axial resolution costs considerably the lateral resolution, this fact severely hampers isotropic 3D imaging of biological samples. In contrast, optical imaging of fluorescence particles with a doughnut beam to locally turn off the fluorescence emission of fluorophores and hereby to bypass the diffraction limit was proposed and demonstrated to achieve a super-resolution both in transverse and longitudinal directions.

## 4.3 Super-resolution imaging with a focused doughnut spot

Recently, a phase modulated beam, namely doughnut beam has played an important role in far-field super-resolution imaging of fluorescence particles, possessing the ability to break the diffraction limit. Techniques such as stimulated emission depletion

(STED) [64], reversible saturable optical fluorescence transitions(RESOLFT) [66, 67] and photoswichable fluorophores in combination with phase mask [36] has been applied to achieve a nano scale optical resolution. The concept for these techniques is to confine the emergence of the "on" state of the fluorophore to a region of a diameter

$$\triangle r \approx \frac{\lambda}{2n\sin\alpha\sqrt{1 + I_\mathrm{m}/I_\mathrm{s}}}, \tag{4.8}$$

where $I_\mathrm{m}$ is the crest intensity of the doughnut beam and $I_\mathrm{s}$ is the characteristic "saturation" intensity of the fluorophore. When $I_\mathrm{m}$ satisfies the condition of $I_\mathrm{m} \gg I_\mathrm{s}$, the resolution $\triangle r \to 0$

The setup used for this experiment is similar as the one in Figure **??** except that the mask used to to form a doughnut focus spot is a $2\pi$ phase modulating mask as illustrated in Figure 4.6 (e). For NV color centers in diamond, the photoluminescence emission is saturated at rather low excitation power (about 1 mW, corresponding to a saturation intensity of about 105 W/cm$^2$). The emission rate therefore does not increase for the excitation power above 1 mW. By using a doughnut-shaped excitation beam, the saturation is only reached in the doughnut region while the doughnut center remains dark. When the NV color center is positioned in this dark spot, there is no excitation and no emission. The emission of a NV color center is then also represented by a doughnut form, with a dark spot in the center. The size of the dark spot gets smaller with excitation power at the saturation regime, and can become nanoscale if the excitation power is very high compared to the excitation saturation level (Figure 4.6(c)). By scanning the diamond nanocrystals sample using the doughnut focused spot, we could therefore determine precisely the position of each NV color center, which can be separated from others by a nanometer distance.

Figure 4.7 shows the photoluminescence images of NV color centers, obtained with a gaussian excitation beam (standard confocal microscope) and with a doughnut excitation beam (STED-like microscope). It is difficult to distinguish the position of NV color centers with a commonly used confocal technique (Figure 4.7 (a) and (b)). In contrast, by using a doughnut-shaped excitation beam, each NV color center is represented by a dark spot and distinguished from others (Figure 4.7(c)). Moreover, with an excitation power of 13 mW, the size of the dark spot becomes effectively nanometric, and two NV color centers separated by only about 250 nm are clearly identified (Figure 4.7(d)). This imaging technique is effectively very useful to determine the position of NV color centers, with a precision well below the diffraction limit of regular confocal microscopy. In order to achieve an even higher resolution, it is necessary to improve the quality of the doughnut beam, *i.e.*, optimize the phase mask for the excitation wavelength.
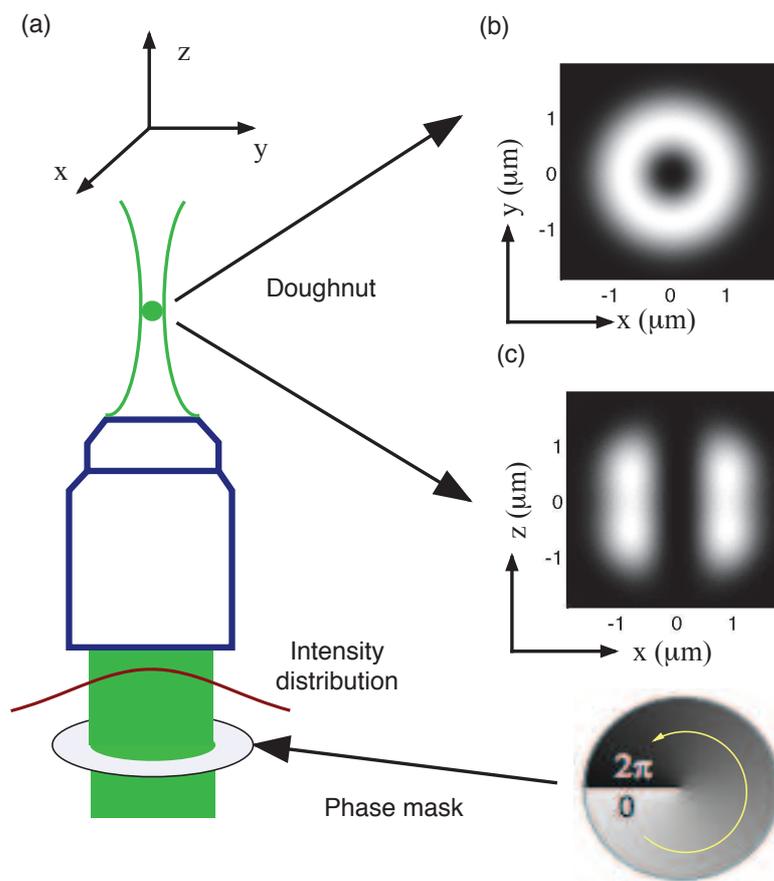
**Figure 4.6:** (a)A doughnut shaped focal spot is formed by using a $2\pi$ phase modulating mask, Calculated intensity distribution of the focusing point in the transverse direction (b), and in the longitudinal direction (c).
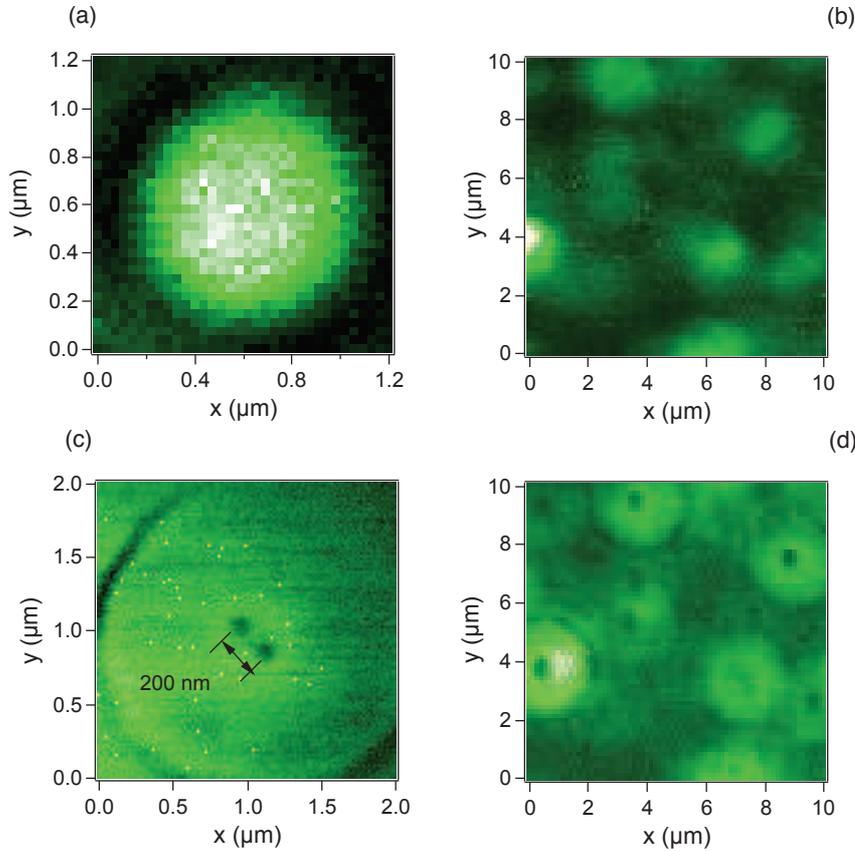
**Figure 4.7:** Super-resolution PL imaging with a doughnut focused spot. (a) and (b) PL images scanned with a gaussian beam. (c) and (d) PL images scanned with a doughnut focused spot. Two NV centers separated by 250 nm which are undistinguished by using a traditional confocal system (a) could be clearly identified (c) by using the douthnut focused spot .

## 4.4 Super-resolution imaging based on IR pulsed excitation quenching effect

The electron depletion quenching has been use for a super-resolution microscopy namely STED, can we also apply the IR thermal quenching effect for super-resolution microscopy as STED? First, let's recall the working principle of STED, which is to phase modulate the quenching beam into a doughnut shape, in the doughnut area, the fluorescence particle i.e. NV color center is "switched off", only the center of the doughnut is in the "on" state, when the quenching beam is working at the saturation regime, the emergence of the "on" state is confined to nanometer scale,Scanning the STED beam with a co-aligned beam for excitation across the sample yields images of sub-diffraction resolution. However, in the case of IR thermal quenching effect, due to the

super-conductivity of diamond, the heat will propagate rapidly from illuminated area to the ambient areas, then in bulk diamond, the "dark center" of the doughnut beam is no longer "dark". For nanodiamonds, when the diamond is in the doughnut area, it is switched off due to thermal effect, when the diamond is in the dark center of the doughnut beam, it can return to the "on" state, Figure 4.8 shows how the IR doughnut modulates the PL intensity of nanodiamonds. The IR doughnut beam can be formed by placing a 2Pi phase mask in the optical path of IR beam, the doughnut can be obtained only when the center of the phase plate and the IR beam are well aligned, by translating the phase mask, the nanodiamond is irradiated by a sequence of **gaussian IR-doughnut IR center-gaussian IR**. Since the IR beam and the VIS beam are co-aligned, when the IR is in Gaussian form, we can observe a strong modulation of PL intensity as shown in the curve edge of Figure 4.8 (b) and (c), when the IR is in Doughnut form, the nanodiamond is in the dark center of the doughnut, the PL intensity is as high as without IR irradiation. This fact enables the IR thermal quenching be used for super-resolution imaging of diamond nanocrystals. Indeed, we have increases the resolution by a factor of 30% with the IR thermal quenching effect as shown in Figure 4.9.

Since the diffraction limit for 1064 nm light is twice larger than 532 nm, the dark area of the doughnut beam is indeed diffraction limited, it will cost quite a lot of IR power to obtain a super-resolution image, that may be the main reason why we didn't get a resolution as high as nanoscale. In the case of traditional STED microscopy, the wavelength of STED beam is very close to which of excitation beam, the STED beam power for super-resolution image should be much lower.

In order to support the above argument, we did some simulations to see how is the size of the doughnut spot at 1064 nm with respect to the Airy spot at 532 nm. Figure 4.10 (a) and (b) shows the doughnut size for wavelength of 532 nm and 1064 nm lasers respectively. Figure 4.10 (c) is the focusing spot of the gaussian beam of 532 nm laser, Figure 4.10(d) shows the comparison of the doughnut spot at 1064 nm and the Airy spot at 532 nm. It is clearly that the size of the dark area of the doughnut spot at 1064 nm is large comparing with the Airy spot at 532 nm.

## 4.5   Conclusions

Three different approaches have been demonstrated to achieve the super-resolution of optical microscopy. The first one is amplitude modulated annular beam, which can increase the lateral resolution by 30%, this technique is suitable for 2D imaging, nano-fabrication, data storage et. al. The second one is making a phase modulated doughnut beam work at the saturation regime of fluorophore (i.e., NV color center), this technique is able to distinguish two NV colors 250nm apart. The third one is a
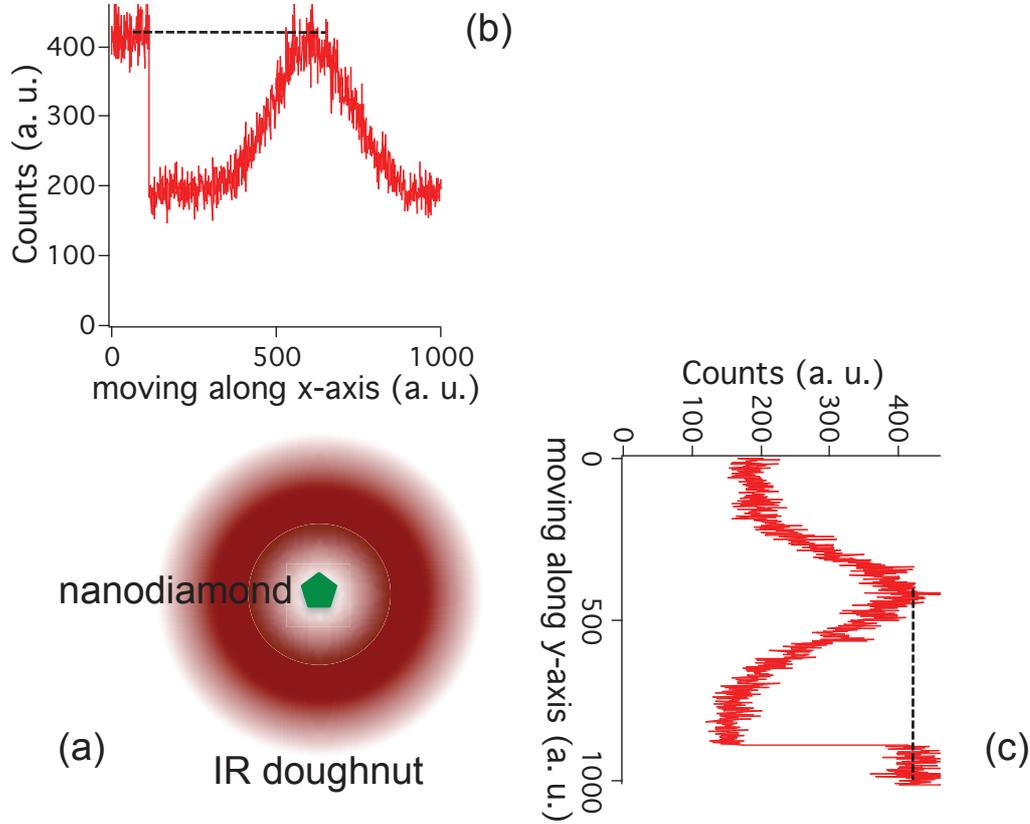
**Figure 4.8:** A luminescence nanodiamond is excited by a combination of an Airy green beam and a doughnut IR beam. (a) When the IR doughnut beam is well aligned with nanodiamond, there is no IR excitation and no thermal effect. When the nanodiamond is raster scanned by this combination, the photoluminescence is modulated as shown in (b) for the a moving in x-direction and in (c) for a moving in y-direction.

STED-like super resolution imaging based on the IR thermal quenching effect of NV color center in diamond, the nature of thermal effect makes it can only be applied for the diamond nanocrystals.

Besides, to address optically a single color center without perturbing the neighbours and to obtain directly the photoluminescence from nanospot, the realization of a so-called positive STED will be necessary, by considering for example two alternative excitations, one has a gaussian form and another has doughnut form. The success of this imaging technique will open the way to single spin optical addressing in the realization of diamond-based quantum computer functioning at room temperature.
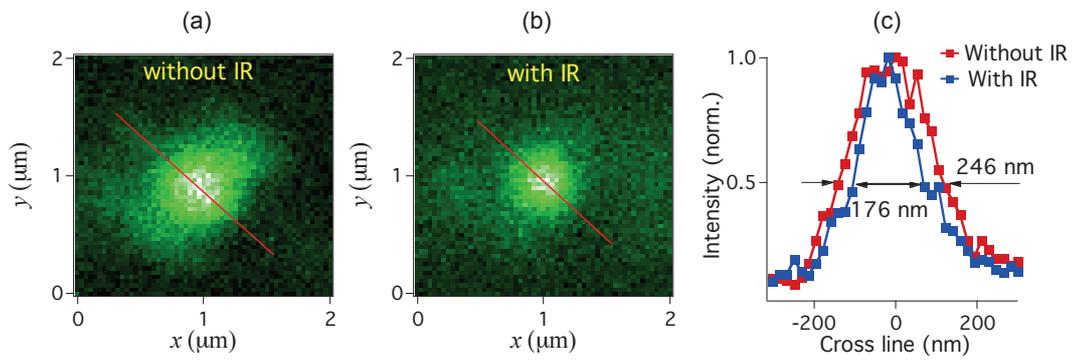
**Figure 4.9:** Optical imaging resolution improvement by IR excitation quenching effect. (a) Scanning image obtained with only a green excitation beam. (b) Scanning image obtained with a combination of a green and an IR doughnut excitation beams. (c) Comparison of the profiles of the photoluminescence spots obtained by two excitation schemes, showing a superresolution of 30 %.
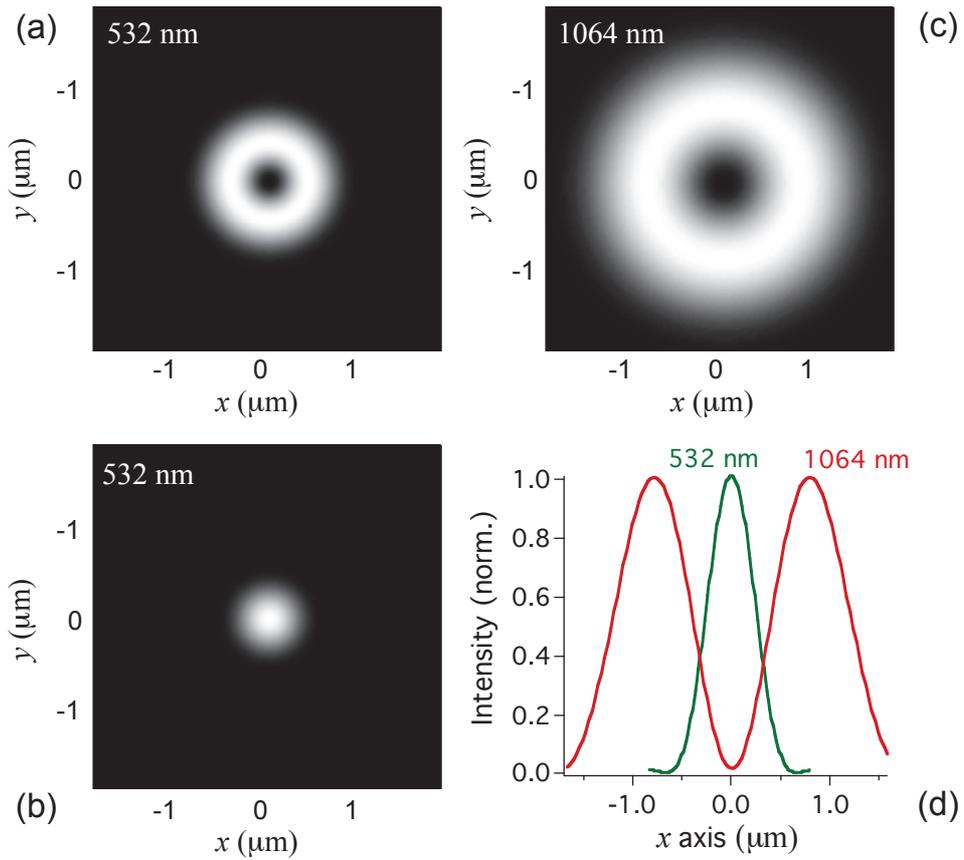
**Figure 4.10:** Theoretical calculation of the Airy and doughnut spots. (a), (b) Doughnut and Airy spots of 532 nm beam, respectively. (c) Doughnut spot of 1064 nm beam. (d) Comparison of the size of the 532 nm Airy spot and 1064 nm doughnut spot. The dark area of the IR doughnut spot is large comparing with the 532 nm Airy spot size. Parameters used for calculations (oil objective microscope): NA (numerical aperture) = 1.4; n (refractive index) = 1.515.

# Part II

# Spin property of NV color centers

# Introduction of ODESR experiment

## Contents

## 5.1 Introduction

One of the most important aspect of NV color center is the electron spin resonance (ESR) of it's negative charge state can be read out optically and can be carried out at room temperature. Which has attracted considerable research interests for applications of quantum information and magnetic field sensing. In the second part of our dessertation, we mainly focus on the ESR manipulation of NV$^-$ electron spin, and they will be referred simply as the NV center or NV spin. In this chapter, we will introduce the spin property of NV color center and the experimental setups for the study of ODESR.

## 5.2   Energy calculation of $NV^-$ color center in the ground state

### 5.2.1   NV spin Hamiltonian

The negatively charged NV center has trigonal $C_{3v}$ symmetry and $^3A_2$ ground state with total electronic spin $S = 1$. Spin-spin interaction leads to a zero-field splitting, $\Delta = 2.87$ GHz, between the $m_s = 0$ and $m_s = \pm 1$ manifolds, where the quantization axis is along the NV-axis. This spin triplet interacts via hyperfine interaction with a spin bath composed of the adjacent $N^{14}$ and the naturally occuring 1.1% $C^{13}$ which is randomly distributed in the diamond lattice. In the presence of an external magnetic field, the dynamics is governed by the following Hamiltonian,

$$
\begin{aligned}
H &= H_{ZF} + H_{eZeeman} + H_{hf} + H_Q + H_{nZeeman} \\
&= \mathbf{S} \cdot \mathrm{D} \cdot \mathbf{S} + g_e \mu_B \mathbf{B} \cdot \mathbf{S} + \sum_k [\mathbf{S} \cdot A_k \cdot \mathbf{I}_k + \mathbf{I}_k \cdot P \cdot \mathbf{I}_k - g_{n,k} \mu_n \mathbf{B} \cdot \mathbf{I}_k]
\end{aligned}
\tag{5.1}
$$

The terms in the Hamiltonian describe the following interactions:

$H_{ZF}$: the zero field splitting.

$H_{eZeeman}$: the electron Zeeman interaction.

$H_{hf}$: the hyperfine interactions.

$H_Q$: the quadrupolar interactions for nuclei with $I > 1/2$.

$H_{nZeeman}$: the nuclear Zeeman interactions.

$\mu_B$ is the Bohr magneton, $\mu_n$ is the nuclear magneton, $g_e$ and $g_n$ are the $g$-factors for the electron and nuclei respectively, $A_k$, the hyperfine coupling tensor, $P$, quadrupole coupling tensor, and $\mathbf{S}$ is the external magnetic field applied to the system. $\mathbf{S}$ is the electron spin vector with magnitude $S = 1$, $\mathbf{I}$ is the nuclear spin vector. The spin matrices for $S = 1$ are:

$$
S_x = \begin{bmatrix} 0 & 0.707 & 0 \\ 0.707 & 0 & 0.707 \\ 0 & 0.707 & 0 \end{bmatrix}
$$

$$
S_y = \begin{bmatrix} 0 & -0.707i & 0 \\ 0.707i & 0 & -0.707i \\ 0 & 0.707i & 0 \end{bmatrix}
$$

$$
S_z = \begin{bmatrix} 1 & 0 & 0 \\ 0 & 0 & 0 \\ 0 & 0 & -1 \end{bmatrix}
$$

The energy levels structure can be obtained by diagonalizing the Hamiltonian corresponding to a specified system. For this purpose the Hamiltonian must first be setup within the appropriate coordinates for the system and then eigenvalues and eigenfunctions can be extracted numerically, using any linear algebra package. In the Hamiltonian 5.1, the zero-field splitting $H_{ZF}$ and the Zeeman effect of electron spin $H_{eZeeman}$ are much stronger than other interactions. The general ESR result can be interpreted simply by the first two terms, and the other terms are perturbations which can lead to additional energy levels and spin decoherence. In our calculation, we simply consider the zero-field splitting and the Zeeman effect on the NV electron spins. The zero-field splitting Hamiltonian can be written as:

$$
\begin{aligned}
H_{ZF} &= D_x S_x^2 + D_y S_y^2 + D_z S_z^2 \\
&= D[S_z^2 - \frac{1}{3}S(S+1)] + E(S_x^2 - S_y^2)
\end{aligned}
\tag{5.2}
$$

Due to the axial symmetry of the NV center, E=0. The ground state of NV center is degenerated into $m_s = 0$ and $m_s = \pm 1$ state due to the anisotropic dipolar interaction of the unpaired electron spins, the zero-field splitting $D = 2.87$ GHz. The Hamiltonian thus be rewritten as:

$$
H = D[S_z^2 - \frac{1}{3}S(S+1)] + g\mu_B \mathbf{B} \cdot \mathbf{S},
\tag{5.3}
$$

Figure 5.1 (a) and (b) are the calculated result of the energy levels of the NV spins in different $\mathbf{B}$-fields by the Hamiltonian equation 5.3, Apparently, they are quite sensitive to the $\mathbf{B}$-field. The energy difference between $m_s = 0$ and $m_s = +1$ (or $m_s = 0$ and $m_s = -1$) levels, or equivalently the resonance frequency , therefore varies in function of the $\mathbf{B}$-field magnitude and orientation as shown in Figure 5.1 (c) and (d).

## 5.3   Working principle of ODESR experiment

Our ODESR experiment is mainly based on the manipulation of the NV electron spin in the ground sublevels. Figure 5.2 is the schematic energy level structure of $NV^-$ center, electron transitions between the ground $^3A$ and excited $^3E$ states produce absorption and luminescence, with the ZPL at 637 nm (1.945 eV). The ground electronic state of the $NV^-$ center is known to be a spin triplet (overall electron spin $S = 1$), the degeneracy of the spin sub-levels of this triplet ground state is lifted to the singlet Z ($m_s = 0$)and the doublet X, Y ($m_s=\pm 1$) spin states because of the anisotropic dipolar interaction of the unpaired electron spins. The zero-field splitting between them is 2.87 GHz, corresponds to the microwave region. The excited electronic triplet state $^3E$ of the center has a rather complicated fine structure originating from the spin-spin and spin -orbit interactions, as well as from the strain in the crystal, some recent studies have been investigated to revealed the fine structure of the $^3E$ excited state [93, 104].
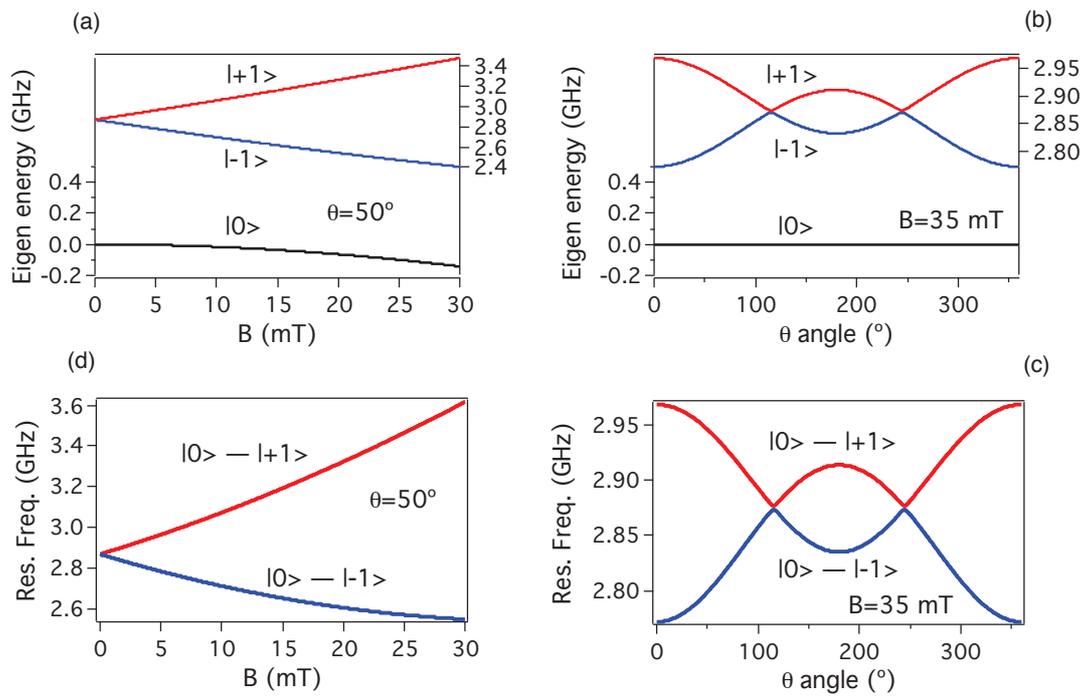
**Figure 5.1:** The calculated energy levels ((a) and (b)) and the resonant frequencies ((c) and (d)) of each states in the presence of a static magnetic field. **B**-magnitude change in (a) and (b), **B** rotates in (b) and (d).

The fine structure of the $^3E$ state will be ignored in our work. In addition to the discrete electronic excited states which contribute to the ZPL, there are a continuum of vibronic excited states which extends the fluorescent spectrum from 650-800 nm at room temperature. Furthermore, a metastable spin singlet $^1A_1$ state is postulated to play an important role in the dynamics of the NV center under optical illumination [38]. Non-resonant excitation excites both the $m_s = 0$ and $m_s = \pm 1$ optical transitions.
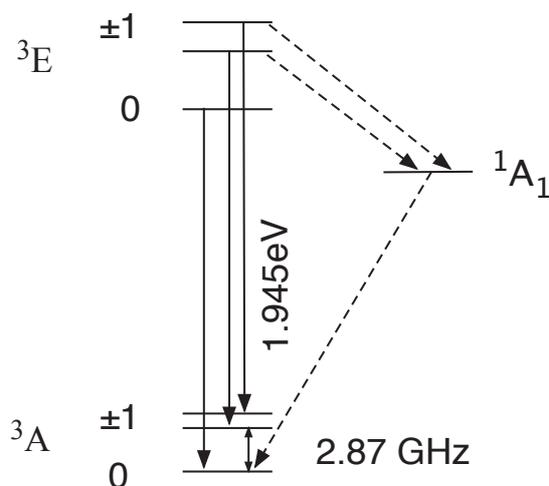


**Figure 5.2:** Schematic energy level structure of NV$^-$ color center, the transition from the excited state ($^3E$) to the ground state ($^3$A) is spin preserving and produces broad band PL with ZPL at 637 nm, $^1A_1$ is a dark state. The electron relaxation through this state is no radiation and non spin preservation. The ground state is a triplet. The zero field splitting between $|0\rangle$ ground state and $|\pm 1\rangle$ ground is 2.87 GHz.

However, because the intersystem crossing occurs primarily from the $m_s = \pm 1$ excited state, population in $m_s = \pm 1$ ground state undergoes fewer fluorescence cycles before shelving in the single state. The $m_s = \pm 1$ states thus fluorescent less than the $m_s = 0$ state, with a difference in initial fluorescence of $\sim 20 - 40\%$ [92, 53, 28].

The optical pumping cycle of the N-V center does not conserve spin angular momentum, leading to spin-selective population of the ground triplet sub-states of the excited defects. Under continued optical illumination, the spin eventually polarizes into the $m_s = 0$ state. By tuning an applied microwave field in resonance with its transitions, the spin can also be readily manipulated. When the NV spin suffers an external microwave frequency which is resonant with one of the spin transitions $m_s = 0 \rightarrow m_s = \pm 1$, the population is redistributed between the two levels and the fluorescence level decreases.

Figure 5.3 presents the ESR spectra of an individual NV spin without and with

the presence of the magnetic field. The continuous 532 nm laser excitation prepares the electron spin into the brighter $m_s = 0$ state by an optical pumping process. When the microwave is applied to the NV center and its frequency is resonant with one of the spin transitions $m_s = 0 \to m_s = \pm 1$, the population is redistributed between the two levels, and the PL decreases . A static magnetic **B** field induces the Zeeman effect of an electron spin, the resonance frequencies between $m_s = 0$ and $m_s = \pm 1$ will be separated into two. Figure 5.3 (b) shows as an example of the photoluminescence versus the scanned microwave frequencies, with an applied magnetic field magnitude B = 4.9 mT. The two dips in photoluminescence from lower to higher microwave frequencies correspond to the resonances $m_s = 0 \leftrightarrow m_s = -1$ and $m_s = 0 \leftrightarrow m_s = +1$, respectively.
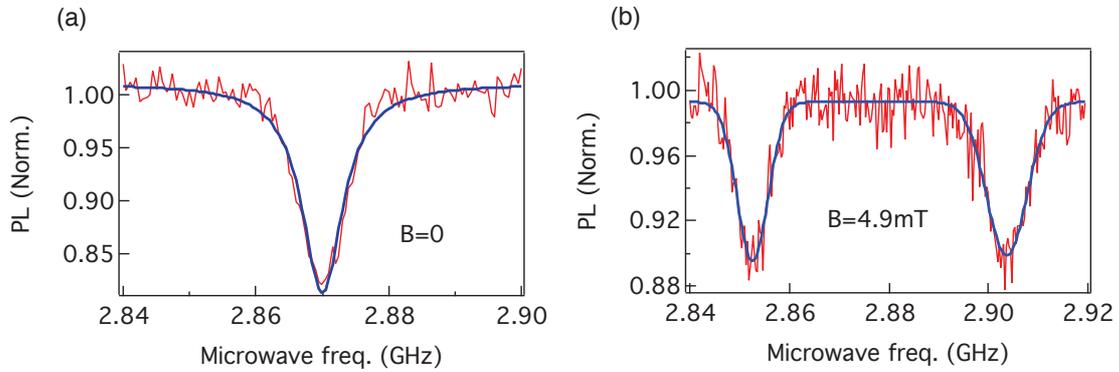
**Figure 5.3:** ESR spectrum of a NV color center, when the microwave frequency (Microwave freq.) is resonant with the NV spin transitions $m_s = 0 \to m_s = \pm 1$, the population is redistributed, and the PL decreases. Figure (a) is ESR spectrum without external magnetic field, the $|+1\rangle$ and $|-1\rangle$ state are degenerate. The static magnetic field induces the Zeeman effect and splits the resonance dip in to two.

The NV spin state can be manipulated and read out using optical excitation as mentioned above, this technique is called optically detected electron spin resonance (ODESR). The ODESR spectra contains a great variety of structural information, for example, the distribution of other impurities around the center[108], the local strain in the diamond lattice[53]. Further more, it can also be used to detect the magnetic field distribution of object surface with a high sensitivity of nanoscale. The density functional theory has been employed to simulate the electron spin density distribution of NV color center. In bulk diamonds, the spin density of the ground state is spread in the lattice, mostly on a plane perpendicular to the (111) direction defined by the positions of the N atom and the vacant site [51]. In nanostructured diamond, the spin density of the NV centers located near the surface (111) is redistributed such that it is mainly localized at the three C atoms that are the nearest neighbors of the N atom and that for the first atomic layer of the (111) surface of the nanocrystal [116].

### 5.3.1 ODESR experimental setup

### 5.3.2 Sample discription

In the second part of this dissertation, the ODESR experiment will be imposed on NV color centers of two different samples,

The first one is ensemble of NV centers in bulk diamond, which will be referred as "ensemble of NV". We start from a type-Ib HPHT [110] oriented single-crystal diamond sample. NV centers are then created from the initially embedded nitrogen impurities, by irradiation with a high-energy electron beam and annealing for 2 hours at 850 °C. With the applied irradiation dose of $10^{13}$ electrons/cm$^2$, a density of about 200 NV centers per $\mu$m$^3$ can be created.

The second one is single NV centers in diamond nanocrystals, which will be referred as "single NV". The type Ib HPHT synthetic diamond nanocrystals (de Beers, Netherland) with 90 nm mean diameter are dispersed in a polymer solution (Polyvinylpyrrolidone, 1 % weight in propanol) to form a stable colloidal suspension, which is spin-coated on a dielectric mirror and form a 30 nm thick layer holding the nanocrystals. The nanoparticle concentration is optimize to achieve a surface density of about one nanocrystal per 10 $\mu$m$^2$ in the polymer layer. Note that the use of the dielectric mirror with a maximum reflectivity 99.97 % in $630 - 750$ nm range corresponding to the NV center photoluminescence spectrum is to increase the light collection efficiency.

### 5.3.3 Excitation lasers

Two exciting lasers will be used in this part: continuous laser (cw laser) and pulsed laser. The cw laser is Verdi V-2 Diode-pumped laser operating at 532 nm wavelength. The pulsed excitation consists of a home build source [17] operating at 532 nm, the pulse width is about 800 ps with a 4-MHz repetition rate.

### 5.3.4 Microwave generation and detection

Microwave signal is generated by Giga-tronics 12000A microwave synthesizer with a resolution of 0.1 Hz, the cw output power range is -20 to +25 dBm. The microwave amplifier shown in Figure 5.4 has a nonlinear amplify factor. The BOONTON 4530 RF powermeter is used to measure the output of microwave power. The freqency range is 10 kHz to 40 GHz for cw signal, the dynamic range is 90 dB.

### 5.3.4.1   CW ESR experiment

The experimental setup used for the ODESR experiment is depicted in Figure 5.4. The home-built confocal system is used to scan the sample, the objective lens used here is air objective lens with NA=0.85. To apply the microwave signal for the electron spin resonance (ESR), the sample is placed on a circuit board with a microwave strip line for input-output connection. The signal from the microwave generator is sent to the input connection (no amplification for cw ESR) and measured at the output. A 20-$\mu$m copper wire placed over the sample is soldered to the strip lines. The wire is positioned within 20 $\mu$m from the optically addressed NV color center. the optical system used for excitation and detection of the PL of NV center is introduced in Figure 2.5 Chapter 2. The ESR measurement is then realized by sweeping the microwave frequency with a step of 0.3 MHz/channel. The external static magnetic field (**B**) applied to the NV center can be varied in magnitude and in orientation by moving and rotating a permanent magnet with respect to the sample. For this purpose, the magnet is mounted on three-axis translation and rotation stages.

### 5.3.4.2   Pulsed ESR experiment

The optical setup for the pulsed ESR experiment is similar as the one for cw ESR experiment. The microwave, and Acousto-optic modular (AOM) are triggered by by a digital signal generator interfaced with a computer. as shown in Figure 5.5. The microwave signal from the microwave generator is amplified before sending to the copper wire, due to the resistance of the copper wire, the maxima mean power sent to the copper is 1 W. All the irradiation microwave powers in the following is the mean power read from the microwave generator, before being amplified. The excitation laser is switched on or off by the AOM. The PL from NV center is collected by the confocal microscope and detected by APD.

The instrument response time to the microwave is measured to be less than 100 ns. Figure 5.6 shows the response time of the instrument when the microwave signal is switched on and off. This response time has been taken into account for the pulsed ESR sequence.

### 5.3.4.3   Lifetime measurement

The lifetime measurement is depicted in Figure 5.7 (a). We excite the NV center with a 4MHz pulsed laser, the laser pulse is used to synchronize the data acquisition. The fluorescence intensity as a function of delay time to the laser pulse will be measured and accumulated to a histogram. The PL decays after the laser pulses as shown in Figure
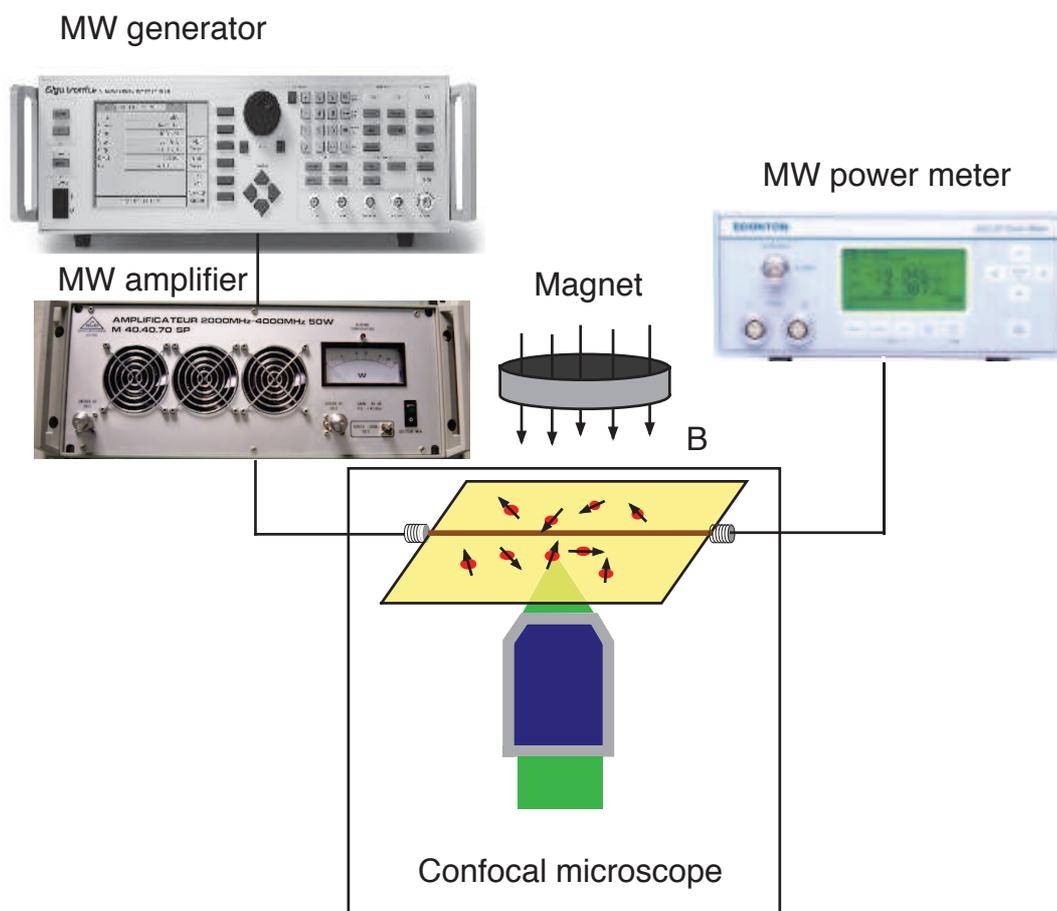
**Figure 5.4:** The setup for NV spin manipulation, the microwave is sent through a thin copper wire which is close to the sample surface. The magnetic field is applied with a magnet, the magnetic field can be controlled by moving the magnetic in 3D space.
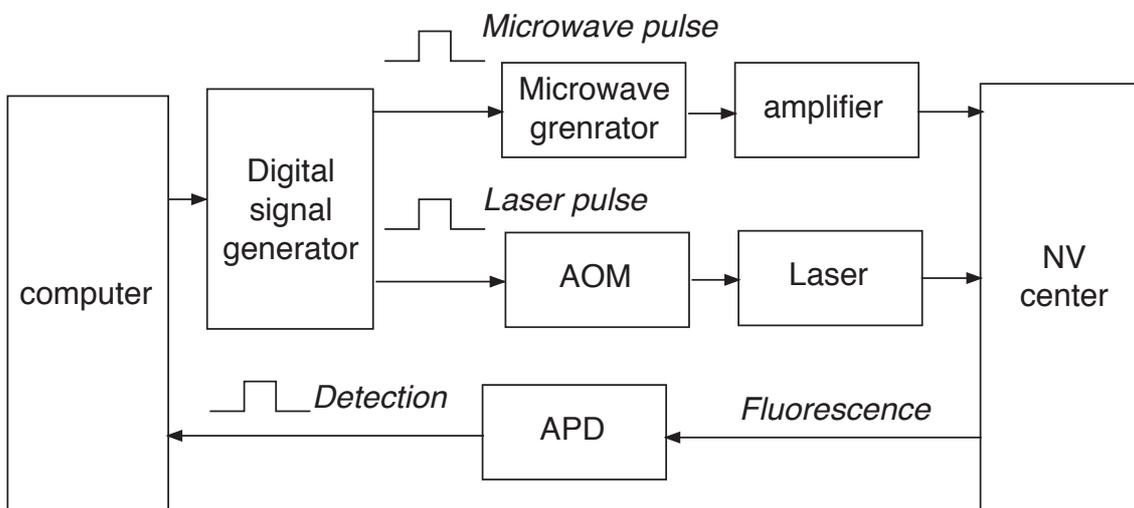
**Figure 5.5:** Pulsed ESR hardware scheme. The microwave generator is triggered b a digital signal generator interfaced with a computer, and the output is amplified by an amplifier. Laser is switched by AOM which is also triggered by the digital signal generator. The fluorescence is detected by the APD.
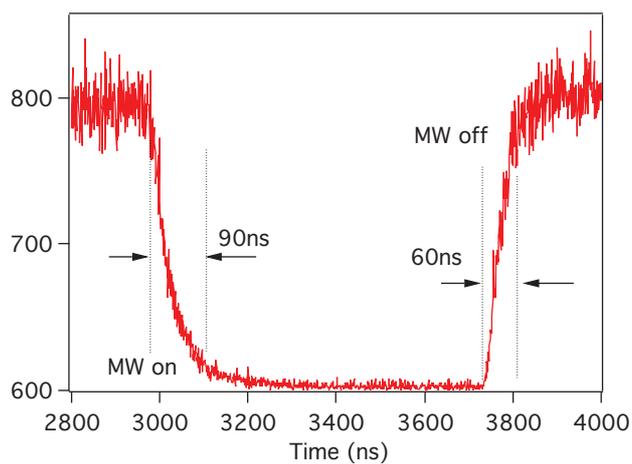


**Figure 5.6:** The instrument response time to the microwave signal. When the microwave signal is switched on the response time is about 90 ns, when the microwave signal is switched on the response time is about 60 ns.

5.7 (b). By fitting the PL decay curve exponentially, the decay rate is considered as the PL lifetime. This measurement will take several minutes depending on the fluorescence intensity.
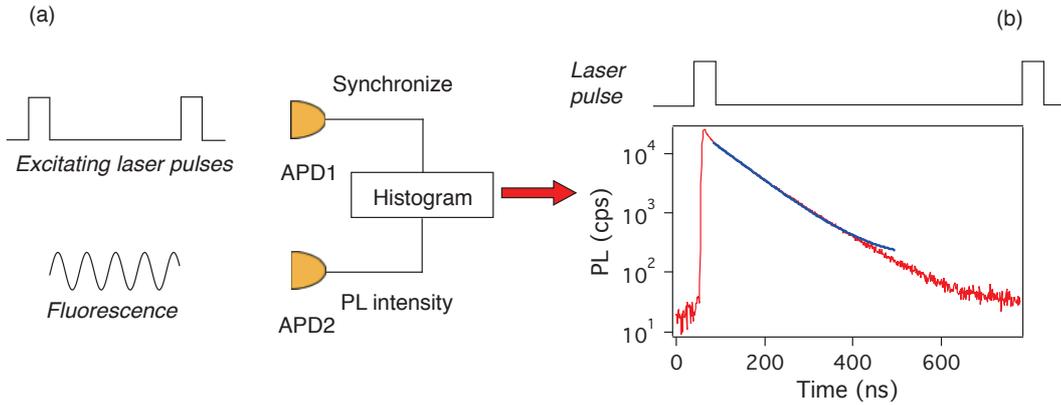


**Figure 5.7:** Lifetime measure of NV color center. The laser pulse is used to synchronize the data acquisition, the PL decays after the laser pulses. By fitting the PL decay curve exponentially, the decay rate is considered as the PL lifetime.

## 5.4   Conclusion

The PL intensity of NV color centers prepared in $|0\rangle$ state is higher compared to those prepared in $\pm 1\rangle$ states. This feature makes it possible to determined the NV electron state from it's optical behavior. The decay rate of $|0\rangle$ and $\pm 1\rangle$ excited state are also different, results in different PL lifetime. The experimental setups of ODESR have been presented. In the following chapters, the NV color centers will be manipulated with microwave field and magnetic field. In Chapter 6 and Chapter7, the ensemble of NV color centers in bulk diamond and single NV centers in diamond nanocrystal will be studied respectively.

CHAPTER 6

# Manipulation of NV color centers

---

**Contents**

## 6.1   Introduction

The NV spin manipulation is generally realized by applying magnetic field and microwave field and read out by its PL intensity perturbation. In this chapter, we will study the interaction of NV spin with the magnetic field, microwave field and excitation laser. The PL lifetime of NV color center will also be investigated as a new technique for the spin study without microwave field.

## 6.2   The modulation study of ODESR spectrum

The ODESR experiment is a time consuming work. The modulation of PL intensity within one loop of microwave frequency detuning is quite modest. In order to suppress the noise and obtain a clear ESR spectrum, it is necessary to apply repetitively the microwave frequency loop and superimpose the signal of each loop. Figure 6.1 shows the ESR signal for different microwave sweeping loop numbers in the same working condition. For the following ODESR experiment in our work, the ESR spectrum are taken with 40 loops of microwave sweeping loops. The modulation of ODESR spectrum is a very important factor for the study of spin property of NV color centers. A
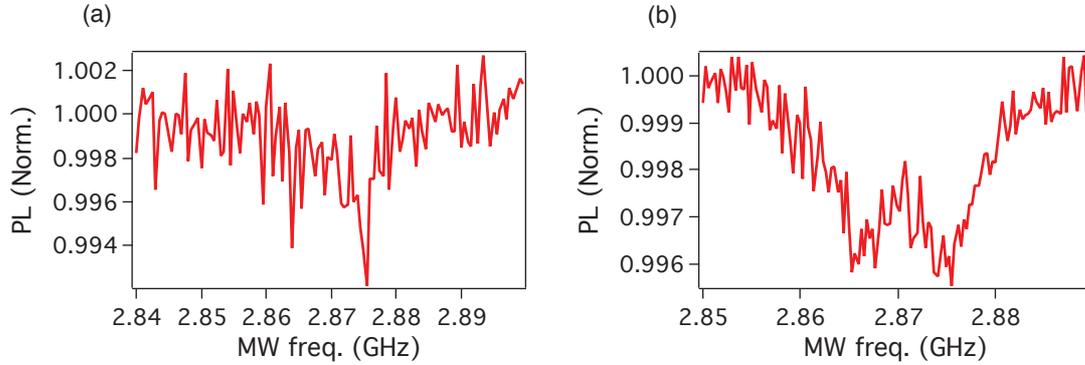
**Figure 6.1:** ESR spectrum of an ensemble of NV centers in a type Ib bulk diamond with (a) 40 loops and (b) 300 loops of microwave frequency. The excitation laser power is 700 $\mu$W, the microwave power is -10 dBm.

high ODESR spectrum modulation can reduce the acquisition time, and increase the sensitivity of the experimental setup. The ODESR spectrum modulation is generally related to the population of $|0\rangle$ state which is transferred to $\pm 1$ state by resonant microwave power, and can be controlled with various methods as following:

1. **Microwave power** The resonant microwave drives the rabi-oscillation of the NV electrons among the ground sub-states. The higher the microwave power, the more population of the $|0\rangle$ state can be transferred to the $|\pm 1\rangle$ states, results in a higher ODESR modulation as shown in Figure 6.2(a). This is a very efficient way to increase the ODESR modulation.

2. **Excitation laser power** By decreasing the laser power, the pumping rate decreases, more population of the $|0\rangle$ state are transferred to the $\pm 1$ states before being pumped. The ESR spectrum of an ensemble of NV color centers for different excitation power is shown in Figure 6.2(b). The microwave power is 20 dBm.

3. **Magnetic field** When the intensity of the external magnetic field increased to a very high value, the $|0\rangle$ state mixes with the $|\pm 1\rangle$ state and the laser cannot prepare a "pure" $|0\rangle$ state. the ESR modulation of NV center decreases as shown in Figure 6.3.
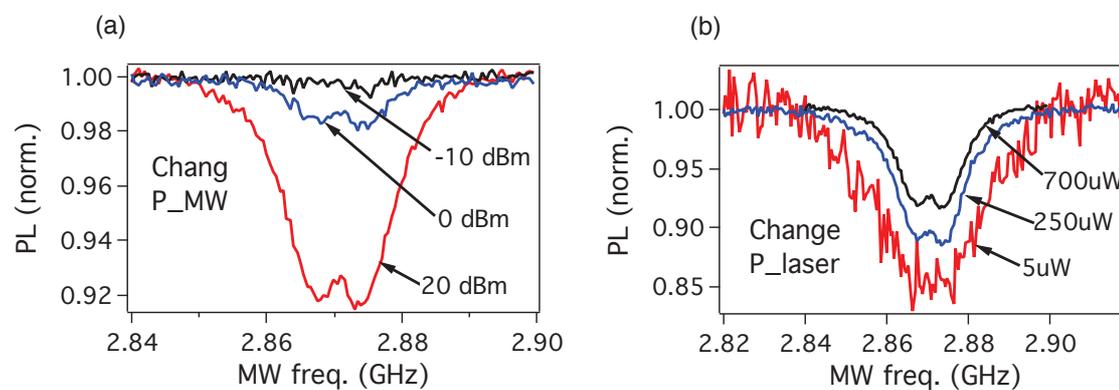
**Figure 6.2:** Modulation ESR measurement changes with Microwave power (a) and Laser power (b).
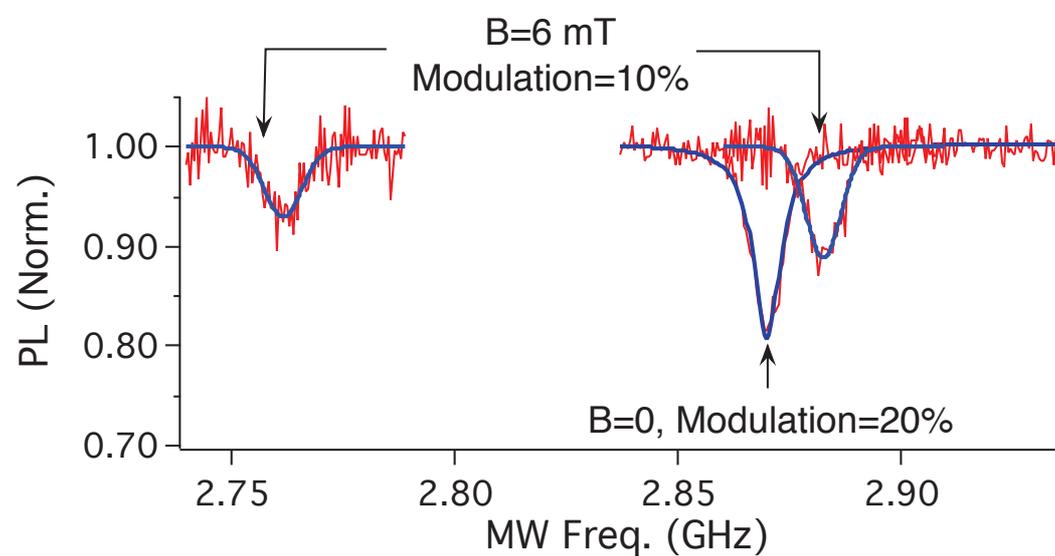


**Figure 6.3:** ESR measurement with and without external magnetic field, the modulation changes due to spin mixing.

## 6.3   NV spin manipulation

### 6.3.1   NV spin manipulation with a continuous microwave field

As we all know, the resonant microwave field will induce the population redistribution among sub-levels of the NV ground state. Without microwave field, the NV center's lifetime decreases with the excitation laser power as shown in Figure 6.4(a), because the excitation laser can polarize the NV center to $|0\rangle$ state, higher excitation makes $|0\rangle$ state saturate, and the populations of $|\pm 1\rangle$ states increase, more electrons are trapped in the metastable $^1A_1$ state. However, when we apply the microwave power onto the NV center, the population distribution of the NV center is modulated, higher excitation power can increase the $|0\rangle$ state population, and the PL lifetime increases as shown in Figure 6.4(b). Under the same excitation power, when the microwave powers increases, the transference from $|0\rangle$ state to $\pm 1\rangle$ state is faster, and the lifetime decreases as shown in Figure 6.4(c).
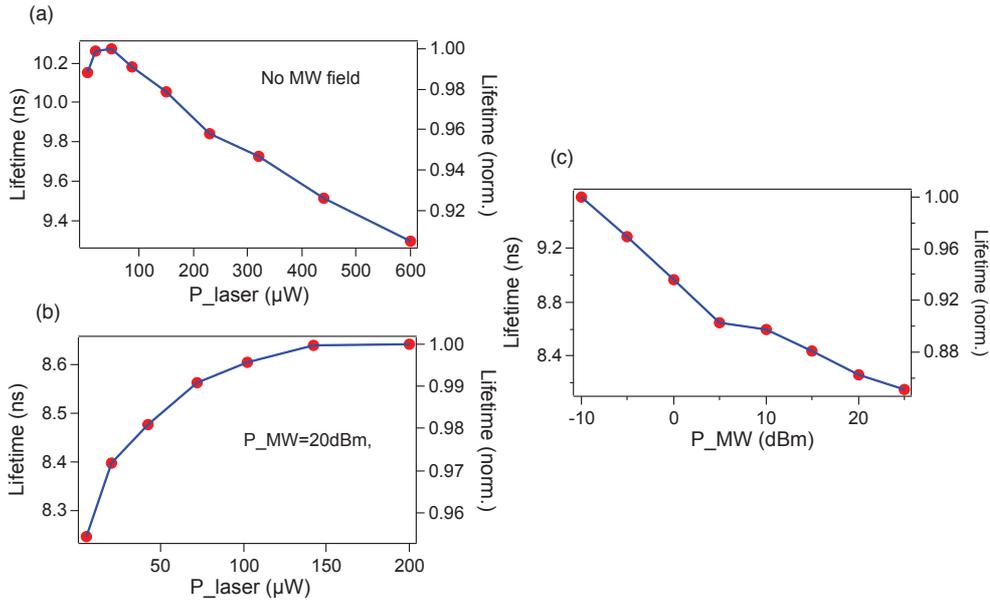


**Figure 6.4:** (a) without applying microwave field, the lifetime of NV color center decreases with excitation laser power. (b) When a ESR resonant microwave field is applied, the lifetime of the NV center increases with the excitation laser power. (c) The lifetime of NV center decreases with microwave power.

When we detune the microwave frequency around the spin resonance frequency of a single NV center, and measure its PL lifetime and PL intensity (ESR specturm) simultaneously. The modulations of these two measurements both increase with the microwave power as shown in Figure 6.5. The modulations of PL intensity and PL

lifetime measurements are similar. However, at low excitation, when the signal to noise ratio of PL signal decreases, the PL intensity measurement become noisy, either a longer acquisition time or a high microwave power will required to reduce the noise. Meanwhile, the lifetime measurement can remove unwanted the background luminescence signal and presents a smoother curve.
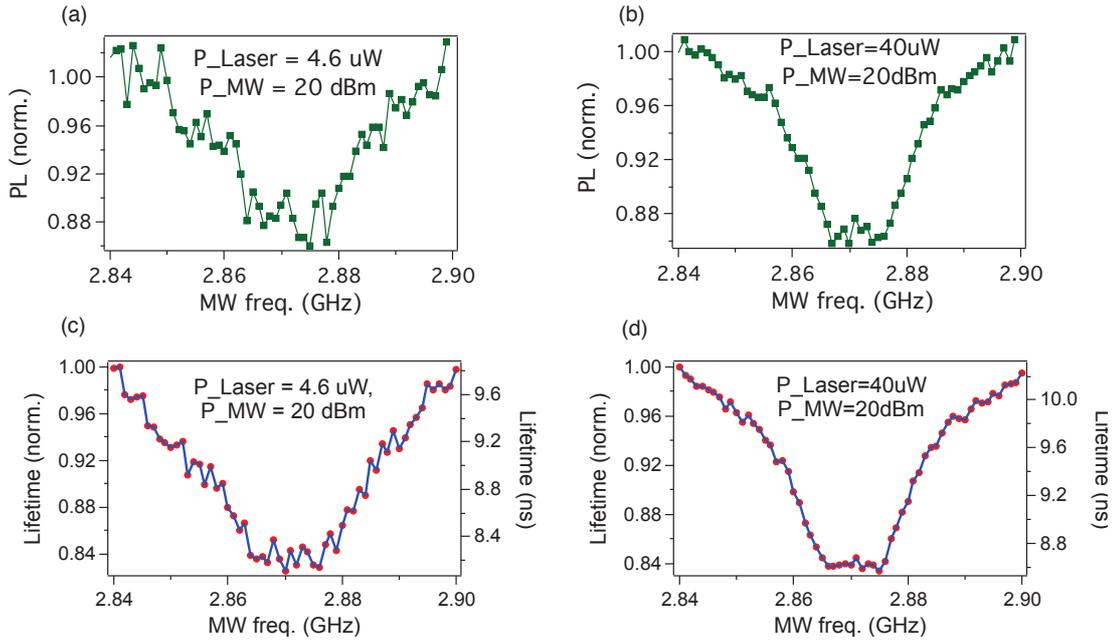


**Figure 6.5:** Measurement of PL intensity and PL lifetime of NV color by sweeping the microwave frequency around the ESR resonance frequency. (a) and (b) are PL intensity measurements with excitation laser power of 4.6 $\mu$W and 40 $\mu$W respectively. (c) and (d) are PL lifetime measurements with excitation laser power of 4.6 $\mu$W and 40 $\mu$W respectively.

### 6.3.2 NV spin manipulation with a static magnetic field

The magnetic field applied with a non-zero orientation in respect with the spin axis, leads to a change in the eigenstates composition of the $|0\rangle$ level. As a consequence, the $|0\rangle$ level will be described by (mostly) $m_s = 0$ eigenfunctions, as well as a $m_s = \pm 1$ component, which under the influence of the magnetic field will result in a Zeeman shift. The effect is maximum for a perpendicular field. To demonstrate this effect, we measure the PL intensity as well as the PL lifetime of NV center at different static magnetic field without applying the microwave power. In the setup of Figure 5.4, we switch off the microwave power. Figure 7.4 (a) and (b) show the dependence of the PL lifetime and PL intensity of a single NV center and an ensemble of NV centers on B-magnitude. The PL intensity changes with a clear correlation with the lifetime

modification both of them decrease with the magnetic field intensity. They are both result from the mixing of the spin states. For the single NV center, the decreasing rate varies with the **B**-orientation, when **B** is along the NV axis, the spin mixing will disappear the PL intensity and PL lifetime will not decrease.
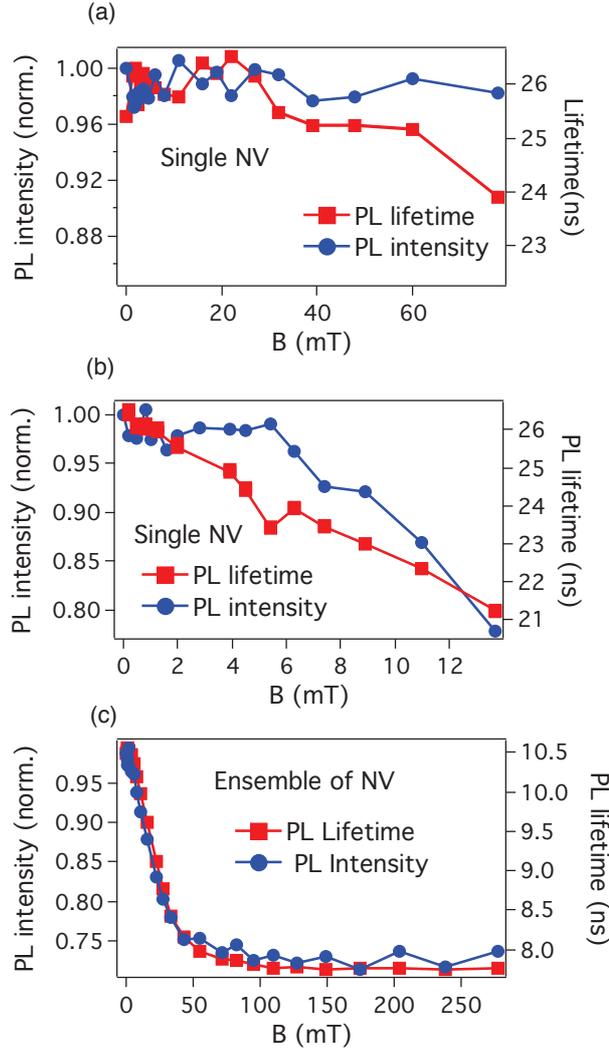


**Figure 6.6:** PL intensity and PL lifetime of as a function of **B**-magnitude. (a) Measurement of single NV center when B has small angle to the NV axis. (b) Measure of single NV center when B has larger angle to the NV axis. (c) Measurement of an ensemble of NV center.

In fact, by solving the hamiltonian of equation 5.3, we can find that each of the ground sub-states have components of other states. When the **B**-magnitude increases, we consider that the $|0\rangle$ state mixes with the $|\pm1\rangle$ state and the laser cannot prepare a "pure" $|0\rangle$ state. Consequently the PL intensity and PL lifetime of NV center decrease.

### 6.3.3 NV spin manipulation with a pulsed microwave field

#### 6.3.3.1 Rabi oscillation

The Rabi oscillation is the cyclic behavior of a two-state quantum system in the presence of an oscillatory driving field. In the case of NV electron spin, when the microwave field is tuned to the resonance frequency between the $|0\rangle$ and $|+1\rangle$ ($|-1\rangle$) state, the probability of finding the atom in the $|0\rangle$ state is found from the Bloch equations to be:

$$|c(t)^2| = \cos(\omega t)^2 \qquad (6.1)$$

where $\omega$ is the Rabi frequency. In another word, for the two level system of NV ground state, if the system is initialized in one of these levels, the resonant microwave field will make the population of each of the levels oscillate with some characteristic frequency which is the Rabi frequency.

To measure the Rabi frequency experimentally, the NV spin is first optically pumped into the $m_s = 0$ sublevel (Figure 6.7). Then pulsed microwave radiation is used to coherently manipulate the spin in the dark. Finally, readout is performed by measuring the photoluminescence rate, which reflects the spin state. The photoluminescence rate is normalized using the signal levels right after the initialization (when $p(m_s = 0) = 1$, where $p(m_s = 0)$ is the probability to be in the state $m_s = 0$) and after a $\pi$ pulse (when $p(m_s = 0) = 0$).
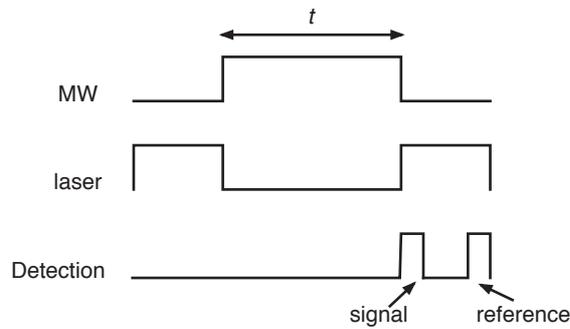


**Figure 6.7:** Pulse sequences for Rabi oscillation. The NV spin is first optically pumped into the $m_s = 0$ sublevel. Then pulsed microwave radiation is used to coherently manipulate the spin in the dark. Finally, readout is performed by measuring the photoluminescence rate.

Figure 6.8 (a) shows the Rabi oscillation of a single NV color center for different irradiating microwave power. The rabi frequency increases with the microwave power. Interestingly, when we compare the Rabi frequency of a single NV center with its ESR modulation, we find that their values are direct proportional. The ratio of Rabi frequency to ESR modulation keeps constant at 18, with standard division of 0.016.
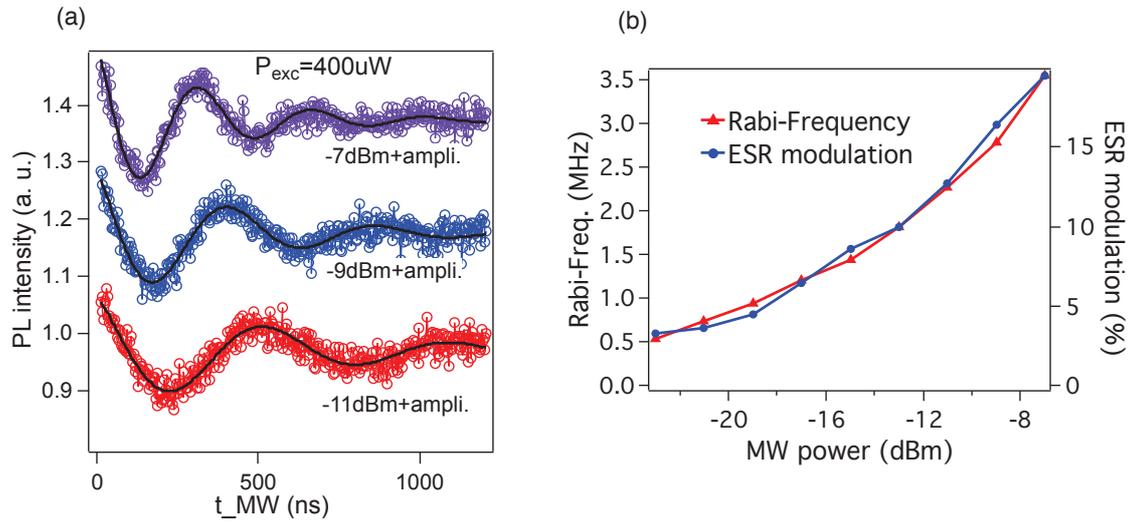
**Figure 6.8:** (a) Rabi oscillation of a single NV color center for different irradiating microwave power. (b) Rabi frequency and ESR modulation of a single NV center as a function of microwave power.
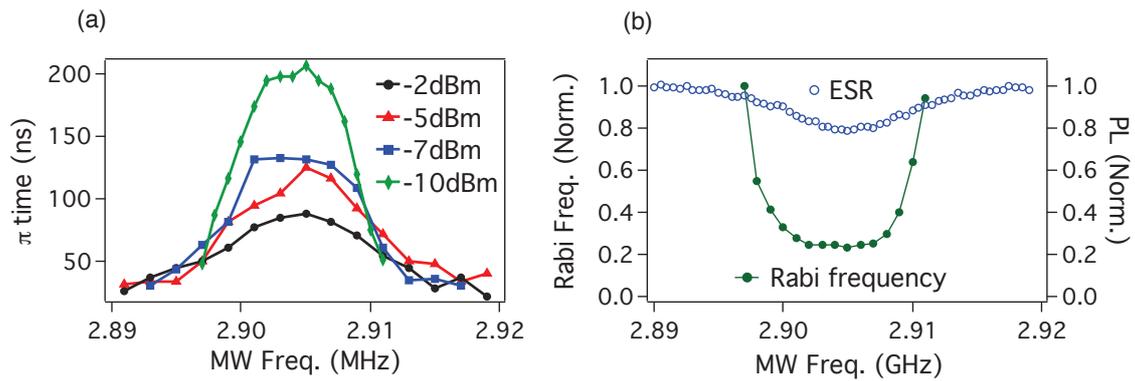


**Figure 6.9:** (a) Measuring $\pi$ time of a single NV center when microwave frequency is detuned out of resonance. (b) Rabi frequency of a single NV center when microwave frequency is detuned out of resonance and ESR spectrum.

Figure 6.9 (a) shows $\pi$ time of a single NV center for microwaves around the ESR resonant frequency. By detuning the microwave frequency around the ESR resonant frequency of NV center, *pi* time is maxima at the resonant frequency, and dramatically increase when the microwave frequency is out of resonance. Figure 6.9 (b) shows the modulation of Rabi frequency and ESR spectrum, the former one can reach about 77% which is very high compared with the ESR spectrum which is predicted to never exceeds 30% under stationary conditions [13].

When we increase the magnetic field intensity, the ESR resonance frequency increases with the magnetic field due to the Zeeman effect. The rabi frequency is measured by fixing the microwave frequency to the ESR resonance frequency. We observe that the NV spin will absorb more microwave power at higher **B** field, in order to get the same output power, the input power should be increased as shown in Figure 6.10 (a). We increase the **B** intensity and keep the output microwave power measured by the power meter in Figure 5.4 as 5 dBm, the Rabi frequency increases with magnetic field intensity as shown in Figure 6.10 (B).
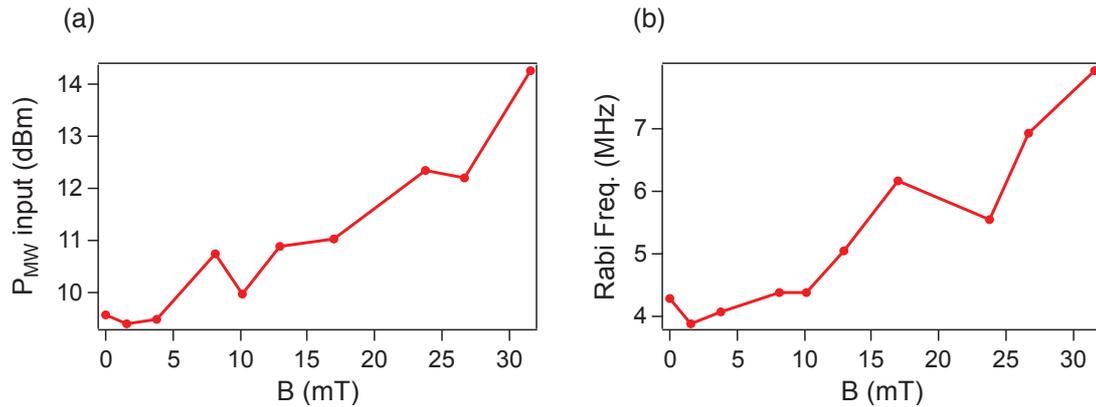


**Figure 6.10:** (a) increasing the magnetic field intensity, in order to have the same output microwave power, the input microwave power is increased. (b) Rabi frequency of NV center as a function of the **B**-magnitude with the input microwave power of Figure (b).

### 6.3.3.2 Hahn-echo experiment

The Rabi oscillation experiments will not give a correct value for the spin dephasing time. To determined the decoherence time for the single electron spin, a Hahn echo procedure was approached. The conventional spin echo method helps eliminate the inhomogeneities related to the system. However, for the actural purpose, the conventional pulse echo sequence has to be modified in order to provide optical readout.

The sequence applied to a single NV consists of the sequence $\pi/2 - \tau_1 - \pi - \tau_2 - \pi/2$

(Figure 6.11 (a)), where $\pi$ represents a microwave pulse of sufficient duration to flip the electron spin from $m_s = 0$ to $m_s = 1$. $\tau_1$ and $\tau_2$ are durations of free evolution times. The first laser pulse is used to polarize the system in its $|0\rangle$ state. The next pulses follow according to the conventional scheme. The first microwave pulse excites the coherences, i.e., the populations are converted into coherences between sublevels of the triplet state. In classical terms, this corresponds to changing the direction of the magnetization vectors, from longitudinal to transversal. For a fixed time period $\tau_1$, the system is left un perturbed and the coherences evolve in the transverse plane. Refocusing of the coherences is done by applying a microwave $\pi$ pulse. The last $\pi/2$ microwave pulse ideally brings the system back to the initial state $m_s = 0$. When $\tau_1$ is fixed and $\tau_2$ is varied as shown in Figure 6.11 (b), a clear echo signal is obtained whenever $\tau_1 = \tau_2$, demonstrating that part of the dephasing can be reversed. By setting $\tau_1 = \tau_2 = \tau$ and varying the total free evolution time $2\tau$, a decay of the primary echo can be observed. The exponential decay will give the decoherence time ($T_2$) of the system. This sequence removes static magnetic shifts caused by a spin bath, allowing to measure the dynamical change of the bath. In this measurement, $T_2 = 1\mu s$, the value will change with the working condition such as magnetic field.
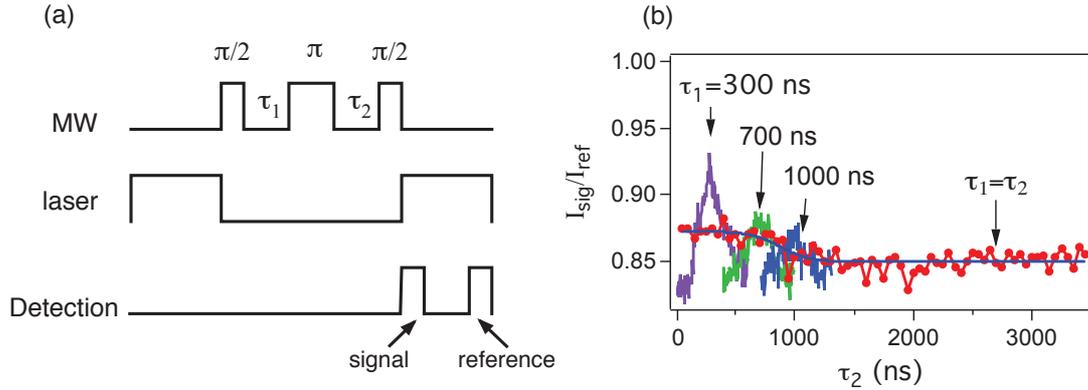


**Figure 6.11:** (a)Pulse sequences for Hahn-echo experiment. (b) Hahn-echo measurement, when fix $\tau_1$ and change $\tau_2$ the echo signal is maximum when $\tau_1 = \tau_2$. By setting $\tau_1 = \tau_2 = \tau$ and varying the total free evolution time $2\tau$, a decay of the primary echo can be observed.

## 6.4  Conclusions

We have manipulated the NV spin with cw microwave field, pulsed microwave sequence, and magnetic field. The NV electron spin state and the population oscillation between ground substates are investigated. Due to the selection rule, the transitions involving $|0\rangle$ and $|\pm1\rangle$ spin states have different PL properties, i.e., PL intensity and PL lifetime. We therefore are able to study the interaction mechanic optically.

The fluorescence cycle and Rabi oscillation are competing in the aspect of population distribution. The fluorescence cycle polarizes NV center into $|0\rangle$ state, by increasing the excitation power, the fluorescence cycle is accelerated and the spin will be polarized to $|0\rangle$ state quickly. In contrast, the resonant microwave field induces the Rabi oscillation between $|0\rangle$ state and $|\pm 1\rangle$ states. Increasing the microwave power will increase the Rabi frequency, and the population will be redistributed in a smaller period. Which results in lifetime decrease and higher ESR modulation. Without the resonant microwave field, the NV will be polarize to $|0\rangle$ state by fluorescence cycle. If increase the excitation power, the fluorescence cycle accelerated, PL intensity increases. However, the $|0\rangle$ state is saturate, and $\pm 1\rangle$ state populations will increase, the PL lifetime decreases. With the resonant microwave field, the population will be redistributed by the microwave field, so increasing the excitation will increase both the PL intensity and PL lifetime.

The static magnetic field induces Zeeman effect, the energy levels of the spin substates will be splitted. Besides, if the magnetic field is not aligned along the NV axis, it will change the eigenstates composition, the $|0\rangle$ state will be described by (mostly) $m_s = 0$ eigenfunction, as well as a $m_s = \pm 1$ component. As a result, the fluorescence cycle cannot totally polarize the $|0\rangle$ state. Increasing the magnet field will reduce both the PL intensity and PL lifetime.

# The ensemble of NV spins in diamond single crystal

## Contents

## 7.1 Introduction

Due to the $C_{3v}$ symmetry of the NV-center in the diamond crystal, each defect has four possible orientations associated to the [111] axis of the crystal [42]. Figure 7.1 (a) shows the structure of a NV color center in a diamond lattice. In the ensemble NV centers, we consider that four groups of NV spins are excited simultaneously, corresponding to the four possible orientation of NV as depicted in Figure 7.1 (b). Here we discuss the influence of an external static magnetic field on the electron spin resonance of an ensemble of NV color centers. We also measure the magnetic field influence on the average photoluminescence lifetime.

(a)                                                                                                (b)
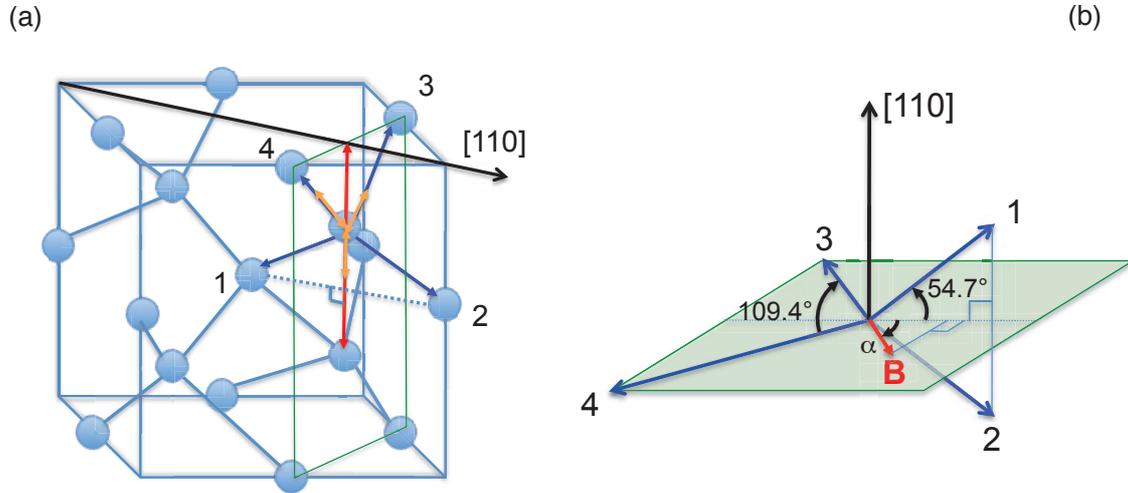


**Figure 7.1:** (a) NV color center in diamond. (b) 4 possible NV axis orientations corresponding to [110] oriented diamond structure.

## 7.2  ODESR of an ensemble of NV color center in bulk diamond

### 7.2.1  ESR measurement

The NV centers are excited with a pulsed laser, Figure 7.2 (a) shows as an example of ESR signal recorded by sweeping the microwave frequency. Without applying the external magnetic field, we observe a drop of luminescence intensity at the microwave frequency 2.87 GHz due to the induced change in populations of $m_S = 0$ and $m_S = \pm 1$ spin sublevels.[2] By applying the static **B** field, the resonance peak splits by the Zeeman effect. For the [110] oriented diamond, by translating the magnet perpendicular to the diamond surface i.e. along the [110] direction, the **B** field orientation is kept unchanged and the **B** field magnitude is modified for the NV centers. From Figure 7.1(b), we can see that the magnetic field effect on group 1 is equivalent to group 2, while group 3 is equivalent to group 4. As a result, the ESR spectrum of NV color centers in this sample has totally two groups of resonant curves as shown in Figure 7.2b. The frequency of these resonance peaks as a function of B magnitude is shown in Figure 7.2 (b). By fitting these data, we find out the $\theta$-angle between **B** and the axis of NV centers, which are $\theta(3,4) = 90°$ and $\theta(1,2) = 35.3°$. These values agree with the crystal structure for the [110] orientation of the NV centers indicated on Figure 7.1 (b).

The Zeeman effect depends not only on the magnetic field magnitude but also on its orientation. We there for carried out a complementary experiment, in which the
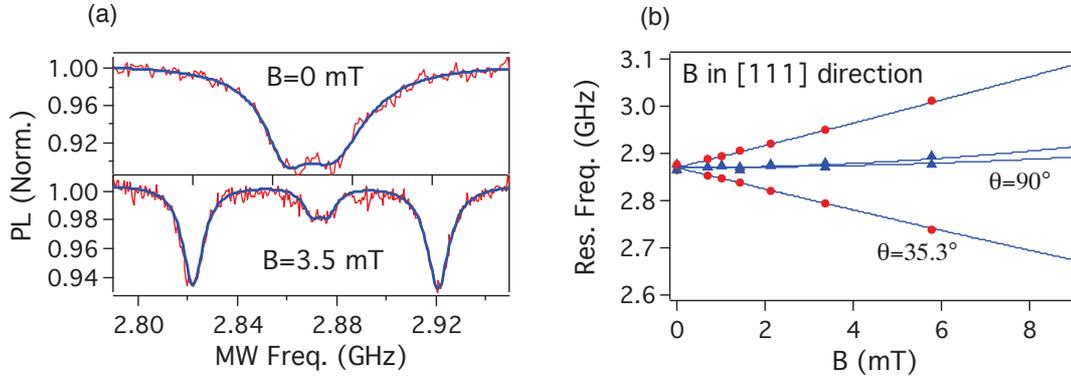
**Figure 7.2:** ESR measurement by increase the **B**-magnitude. (a) When **B** = 0, the ESR resonant frequency is about 2.87 GHz. By increasing **B**-magnitude, the ESR resonant frequency splits due to Zeeman effect, each spin group has special resonance frequency. (b) When the magnetic field is along the [110] orientation, group 1 and 2 are equivalent, meanwhile group 3 and 4 are equivalent.

magnetic field magnitude is kept at a fixed value ($B_2$=3.5 mT), by keeping a constant distance between the magnet and the sample, and in which we move the magnet in such a way that $B_2$ lies in the plane (3, 4) and is rotated around the [110] axis (see Figure 7.1 (b)). By computing the Zeeman effect for all possible orientations, the ESR frequency is evaluated as a function of the rotation angle $\alpha$. The calculation agrees with the experimental results as shown in Figure 7.3, except for a small separation observed between the resonance peaks corresponding to the two orientations 1 and 2 of the NV center. This discrepancy is due to the slight mismatch of the $B_2$ field position in the plane containing the orientations 3 and 4.

## 7.3   Lifetime measurement

Using the picosecond laser, we can also investigate the influence of the applied magnetic field on the emission rate and on the photoluminescence lifetime. The lifetime is determined by using excitation pulses as starts and photoluminescence photons as stops in the intensity time-correlation measurement setup. Due to different leaking rates toward the spin singlet level $^1$A,[2] the lifetime associated to transition between $m_S = 0$ levels is longer than the one associated to transitions between $m_S = \pm 1$ levels.[14] The mixing of these states, induced by the magnetic field, can therefore lead to a modification of the photoluminescence lifetime. By applying the static magnetic field, we indeed observe that the average lifetime for the ensemble of NV centers is changed, depending on the magnitude and orientation of the **B**-field. Figures 4(a) and (b) show the dependence of the lifetime on **B**-magnitude for two particular orientations of the **B**-field, *i.e.*, parallel
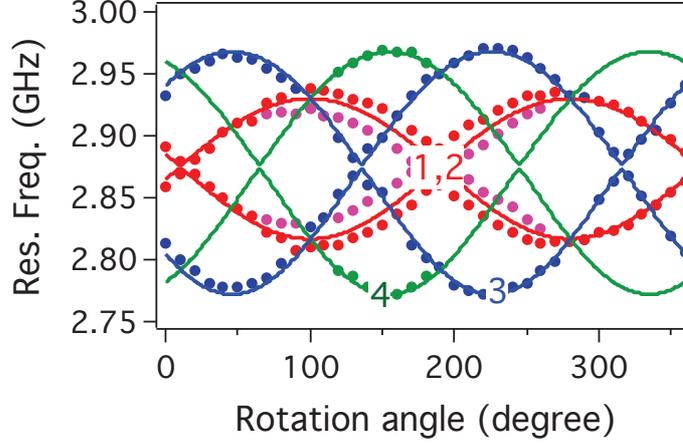
**Figure 7.3:** The ESR spectrum of the ensemble of NV centers in bulk diamond, when the magnetic field is rotate on the [110] surface, group 1 and 2 are equipment, however, group 3 and 4, have 109° phase different, while their amplitude keeps the same.

and perpendicular to the [110] crystal axis. Since the lifetime associated to $m_S = \pm 1$ states is smaller than the one associated to $m_S = 0$ states,[14] the mixed state due to magnetic coupling has intermediate lifetime. By recording the photoluminescence signal while changing the magnetic field magnitude, the luminescence intensity is also changed with a clear correlation with the lifetime modification, as shown in Fig. 4(a) and Fig. 4(b). This effect is similarly explained by the mixing of the spin states.[6] We therefore expect that the measurement of the NV-center lifetime can be applied to either increase the ESR-signal visibility or decrease the ESR measurement time in case of weak luminescence signal. Furthermore, the lifetime is sensitive to **B**-orientation. By keeping **B**-magnitude constant and changing **B**-orientation in the plane perpendicular to [110] crystal axis, we indeed observe a correlated modification of the NV-center radiative lifetime, as shown in Fig. 4(c).

Further more, the lifetime is sensitive to **B**-orientation. By keeping **B**-magnitude constant and changing **B**-orientation in the plane perpendicular to [110] crystal axis. The measurements are made under 4 different **B**-magnitudes: 19.4 mT, 34.9 mT, 49.2mT and 72.5 mT as shown in Figure 7.5(a). Two peaks separated with 180° are very clear. They become sharper when the **B**-magnitude increases. When B=72.5 mT, the lifetime keeps almost unchanged for different B orientations. In addition, there are two other small peaks appear when B=34.9 mT and 49.2 mT. The relative angle between the small peak and the main peak is about 109°.

In calculation, the NV spins are categorized into four groups as introduced in Chapter 5. We assume that the lifetime of $|0\rangle$ and $|\pm 1\rangle$ states are 10.5 ns and 7 ns respectively
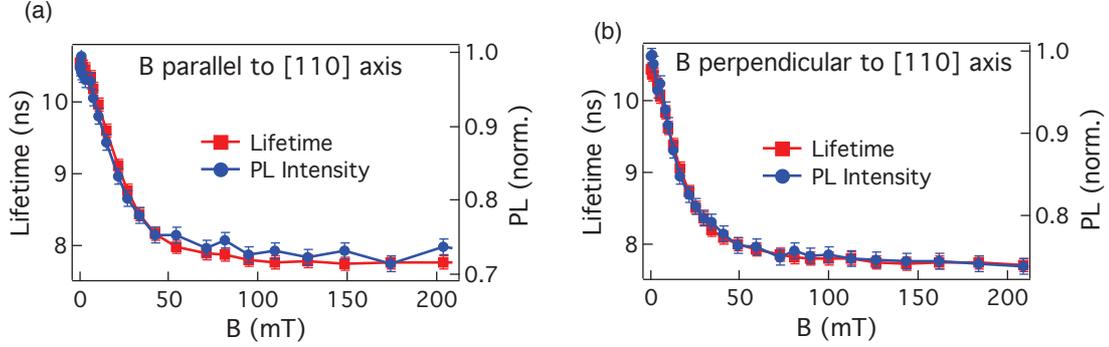
**Figure 7.4:** Measurement of PL intensity and PL lifetime as a function of **B** magnitude. (a) **B** is parallel to the [110] axis. (b) **B** is perpendicular to the [110] axis. The PL intensity changes with a clear correlation with the lifetime modification, both of them decrease obviously with the magnetic field intensity.

(for different samples, the lifetime will be different). When B=0, the NV centers are in $|0\rangle$ state, when B$\neq$ 0, the population for each eigenstate is calculated according to the hamiltonian in equation **??**. The lifetime for each group is given as:

$$T = (10.5 * n_0 + 7 * (n_{+1} + n_{-1}))/(n_0 + n_{+1} + n_{-1}) \tag{7.1}$$

where $n_0$, $n_{+1}$ and $n_{-1}$ are the population of $|0\rangle$, $|+1\rangle$ and $|-1\rangle$ states respectively. The PL lifetime is the average of the four groups of the NV centers. The calculated result is shown in Figure 7.5(b). The group 1 and 2 NV centers has an angle of 54.7° angle to the [110] plane, the effect of **B** field to these two groups are much smaller than group 3 and 4. The 4 peaks are in fact corresponding to group 3 and 4, each of them has two peaks when **B** makes 0 and 180° angle with them. When **B**-magnitude increases, the peaks become sharper as the experimental result. In the experimental result, the peaks corresponding to group 3 are very clear while those corresponding to group 4 are not clear and almost invisible. This might be due to there are not enough NV centers in group 4. Indeed, from Figure 7.3, we can also see that there are not many points on the curve 4, which is also an evidence supporting our explanation.

High sensitivity magnetic imaging using an ensemble of NV centers in diamond acting as magnetic field sensors has been demonstrated recently. The technique offers full reconstruction of the magnetic field vector and improved temporal resolution. The sensitivity and readout fidelities of this apparatus depends largely on the uniformity of the NV spin distribution. The uniformity of the sample is commonly evaluated through the PL intensity distribution. However, as we have discussed in Chapter 5, the NV color center's orientation with respect to the magnetic field orientation strongly
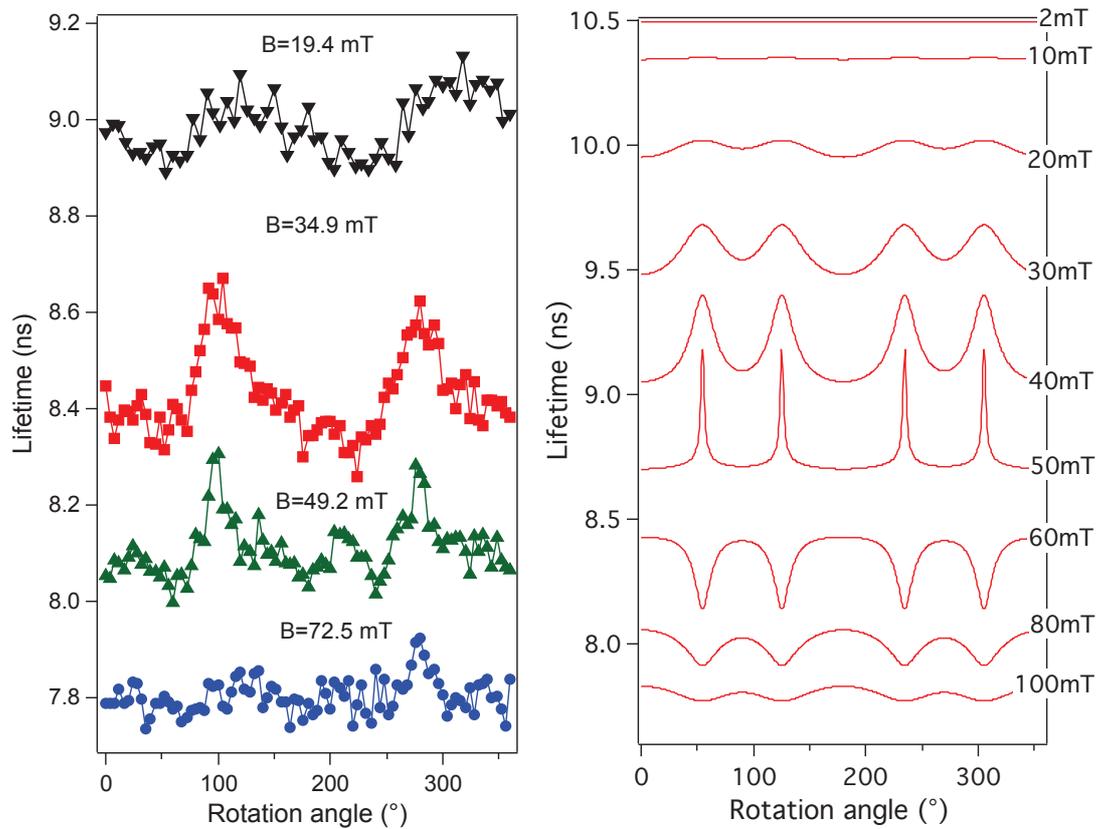
**Figure 7.5:** Lifetime measurement by rotating **B**-orientation on the [110] plane. (a) Experimental result, the measurements of 4 different **B** magnitudes (19.4 mT, 34.9 mT, 49.2mT and 72.5 mT) are made. (b) Calculation result of the ideal case: all the NVs including the density and orientations are uniformly distributed. Lifetime of $|0\rangle$ and $|\pm 1\rangle$ states are 10.5 ns and 7 ns respectively.

influences the ESR result. In fact, certain fabrication techniques are possibly create NV centers in preferential orientations. From the lifetime study of ensemble of NV centers suffered an external magnetic field, we are able to evaluate the preferential NV axis orientations.

## 7.4 Conclusions

In conclusion, we have demonstrated the effect of a static magnetic field $\mathbf{B}$ on the electron spin resonance of an ensemble of NV centers oriented in the four possible directions in a bulk diamond crystal. The resonance frequency associated to each orientation has specific dependency with $\mathbf{B}$-magnitude and $\mathbf{B}$-orientation. These results have direct application to spin-resonance-based magnetometry with NV centers. Furthermore, the average radiative lifetime of the NV ensemble can be modified by a microwave-free technique, thanks to the mixing of the $m_S = 0$ and $m_S = \pm 1$ spin states by an external magnetic field. This effect can be used for a detection of the magnetic field, without the requirement of a microwave antenna. The PL lifetime of an ensemble of NV centers in the presence of magnetic field has been simulated, and supposed to be able to evaluate the orientation uniformity of NV color center distribution.

# single NV spin orientation in diamond nanocrystals

## Contents

## 8.1 Introduction

The orientation of a diamond nanocrystal crystallographic axis relative to the substrate surface is randomly distributed. Due to the $C_{3v}$ symmetry of the NV-centers in the diamond crystal, a single NV-center is aligned along one of four possible orientations[77] associated to the [111] axis of the crystal, which is undetermined due to the arbitrary orientation of the diamond nanocrystal. In this chapter, we will investigate the optical transition dipoles and the orientation of an electron spin associated to a single nitrogen-vacancy (NV) color center in diamond nanocrystals. By simply using the polarization analysis, we are able to determine the optical transition dipoles of a randomly oriented NV color center and their orientations in free space. Indeed, by changing the polarization of the excitation laser, we experimentally demonstrated that the NV color center has two orthogonal dipoles. By analyzing the polarization of the photoluminescence light while keeping unchanged the excitation polarization, the orientation of each optical transition dipole is well identified. The determination of optical dipoles orientations is neccessary to allow an efficient coupling of NV color centers to microstructures, such

as plasmonic nanostructures and photonic crystals. Moreover, this all-optical measurement technique also allows to find out the orientation of the NV-axis, with an angle uncertainty of $\pm 2°$. This information is then accurately determined by an alternative methode based on the electron spin resonance of a single NV color center. Indeed, the electron spin state associated to a single NV color center is optically readout by monitoring the photoluminescence intensity while sweeping the frequency of a micro-wave field around the spin resonance. By applying to a single NV center an external magnetic field of adjustable magnitude and orientation, and by following the subsequent Zeeman shift of its spin resonance, we infer the orientation of a single electron spin associated to a single NV color center in randomly oriented diamond nanocrystal in the laboratory reference frame, with an angle uncertainty of less than $\pm 1°$. This information is of great interest for numerous applications such as high sensitive magnetometry based on single spin resonance or in quantum information processing based on multiple-electron-spins coupling. Furthermore, this electron spin resonance measurement yields results that are in agreement with the polarization analysis, confirming that two optical transition dipoles are in a plane perpendicular to the NV-center spin axis.

## 8.2   Experimental setup

The home-built confocal setup in Figure 2.5 is used for optical excitation and detection of the NV center PL properties. the polarization of the excitation light is controlled by a half-wave plate (HWP) and the polarization of the photoluminescence is analyzed by a thin polarizer (polaroid sheet). Both the HWP and polarizer angular positions are controlled by a rotation motor. In the following, we will consider a laboratory reference frame $(O, x, y, z)$ with the NV center studied as the origin $O$, and with the $Oz$-axis identical to the microscope objective axis. The ESR setup for NV spin study is introduced in Chapter 5. In the work presented here, we address only single NV color centers in diamond nanocrystals, which were identified by the antibunching measurements, as the one shown in Figure 8.2.

## 8.3   Transition dipoles and spin axis of a single NV center

In the case of bulk diamond crystals, some experimental works[42, 33, 4] indicated that a single NV color center possesses two orthogonal and incoherent transition dipoles, laying in a plane perpendicular to the NV spin axis. In a recent work,[73] it was shown that at cryogenic temperature, one can address each dipole individually, which allows to predict the coupling of these transition dipoles.

We demonstrate here a simple all-optical method, by measuring the polarization de-
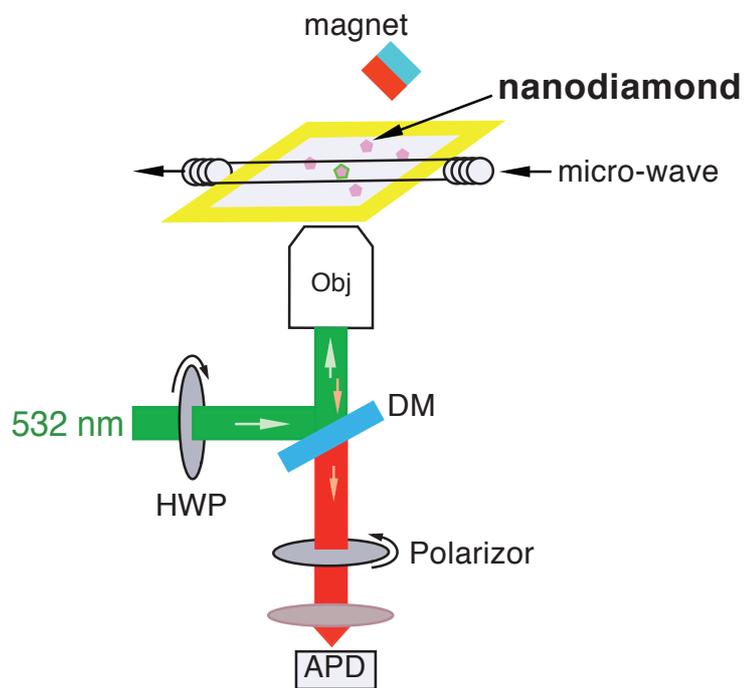
**Figure 8.1:** Experimental setup used to determine the spin orientation and transition dipoles of a single NV color center in diamond nanocrystals. DM: dichroic mirror, high reflection at 532 nm and high transmission in the range $580 - 750$ nm. HWP: half-wave plate at 532 nm-wavelength. Obj: microscope objective, numerical aperture NA $= 0.95$. The magnet is controlled in orientation and in position by a rotation and a translation systems.
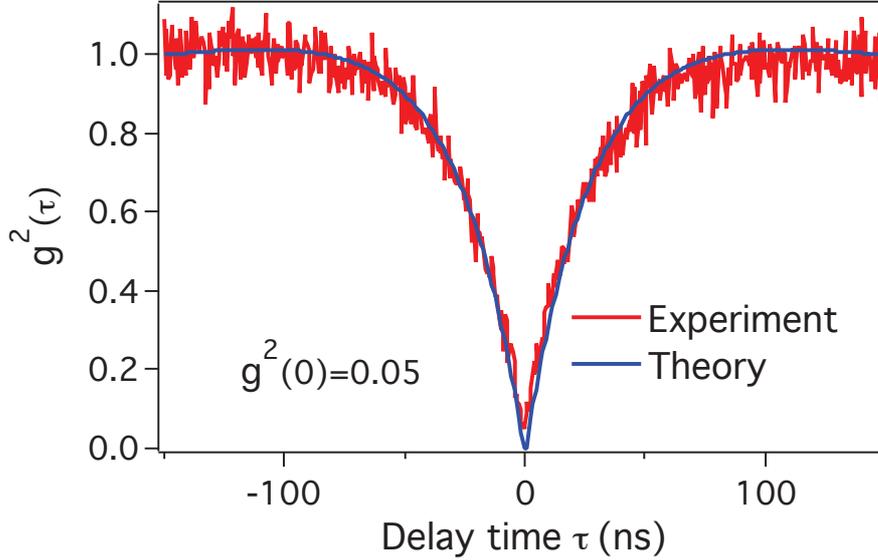
**Figure 8.2:** (a) NV center photoluminescence time intensity correlation histogram showing photon anti-bunching which is the signature of single-photon emission from an individual NV color center. Laser excitation power is 0.1 mW. (b) Optically detected magnetic resonance of the single electron spin associated to this single NV color center, with B = 4.9 mT.

pendence of excitation and emission of a single NV color center in a diamond nanocrystal that is randomly oriented in space, to determine at room temperature the i) optical transition dipoles; ii) the dipoles orientations and their coupling; and iii) the orientation of the NV color center.

### 8.3.1   Analysis of excitation polarization dependence

Single NV color centers are identified with HBT technique, the anti-bunching curve in Figure 8.2 shows that the $g^{(2)}$ value of the studied NV color center is close to 0. We excite the single NV color center with a linearly polarized laser beam and directly detect its photoluminescence intensity without putting the polarizer (see Figure 8.1). The dipole scheme of NV color center is shown in Figure 8.4, S is the spin orientation of NV defect, corresponding to the NV axis, angle $\alpha$ is the polarization of the excitation beam, located in the $x, y$ plane. Figure 8.3(a) displays polar plots of the normalized photon counting as a function of the excitation polarization for different excitation powers. The normalized photoluminescence is maximal ($C_{max}$) at $\alpha = 15°$ and minimal ($C_{min}$) at $\alpha = 105°$. By changing the excitation power, the $C_{min}/C_{max}$ ratio remains constant at power lower than 0.2 mW, then increases, and saturates at power higher than 2 mW, as shown in Figure 8.3(b). Note that the polarization dependence of the

dichroic mirror (DM) for the 532 nm-excitation beam and the 670 nm-PL light is small enough to be neglected.

In order to explain the observed polarization dependance, we consider a model associating two mutually orthogonal transition dipoles ($D_1$, $D_2$) to the NV color center, forming a plane perpendicular to the NV axis, as illustrated in Figure 8.4. This plane has a crossing line L with the $(x, y)$-plane. The polarization direction P of the excitation light is in the $(x, y)$-plane (polarization plane). The energy absorbed by dipole $I_1$ can be calculated as:

$$
\begin{aligned}
I_1 &= (\mathrm{P} \cdot \mathrm{D_1})^2 \\
&= ((\mathrm{P_1} + \mathrm{P_2}) \cdot (\mathrm{D_{11}} + \mathrm{D_{12}}))^2 \\
&= (\mathrm{P_1} \cdot \mathrm{D_{11}} + \mathrm{P_2} \cdot \mathrm{D_{12}})^2 \\
&= P^2 \times D_1^2 (\cos(\alpha - \phi - 90)\cos(\beta) + \sin(\alpha - \phi - 90)\sin(\beta)\cos(\theta))^2
\end{aligned} \tag{8.1}
$$

Similarly, The energy absorbed by dipole $I_2$ can be calculated as:

$$
I_2 = P^2 \times D_2^2 (-\cos(\alpha - \phi - 90)\sin(\beta) + \sin(\alpha - \phi - 90)\cos(\beta)\cos(\theta))^2 \tag{8.2}
$$

where $\alpha$ is the polarization rotation angle, $\beta$ is the angle between the $D_1$-dipole and the L-cross-line, $\theta$ is angle between the $z$-axis and the NV-axis (S), and $\phi$ is angle between the $x$-axis and the projection of NV-axis to the $xy$-plane. The total intensity absorbed by these two dipoles can be: calculated as:

$$
\begin{aligned}
I_{\mathrm{abs}} &= I_1 + I_2 \\
&= I(\sin^2(\alpha - \phi) + \cos^2(\alpha - \phi)\cos^2\theta) \\
&= I(1 - \cos^2(\alpha - \phi)\sin^2\theta)
\end{aligned} \tag{8.3}
$$

We can see clearly that the absorption efficiency is independent of the $\beta$-angle (angle between one dipole, e.g. $D_1$, and the cross-line L, see 8.4). The total absorption energy depends on the orientation ($\theta$, $\phi$) of the NV center, and varies as a function of the linear polarization orientation ($\alpha$-angle) of the excitation light. From equation (3), one can see that when $\alpha = \phi$, the absorption (accordingly the photoluminescence) is minimal ($I_{\mathrm{asb}} = I_{\mathrm{min}} = I\cos^2\theta$) and when $\alpha = \phi \pm 90°$, the absorption (accordingly the photoluminescence) is maximal ($I_{\mathrm{asb}} = I_{\mathrm{max}} = I$). This remark explains the minimal photoluminescence obtained at $\alpha = \phi = 105°$ as shown in 8.3. Moreover, at low excitation power, e.g. 0.09 mW, corresponding to non-saturation regime, we experimentally obtained $C_{\mathrm{min}}/C_{\mathrm{max}} = 0.36\pm0.04$, equivalent to $I_{\mathrm{min}}/I_{\mathrm{max}} = \cos^2\theta = 0.36\pm0.04$, and leading to $\theta = 53°\pm2°$. This result will be confirmed with the spin orientation of the same NV color center determined by the ODESR experiment which will be discussed in Chapter 7.

However, in order to fully interpret observations depicted in Figure 8.3, one has to take into account the saturation effect of the NV color center photoluminescence at
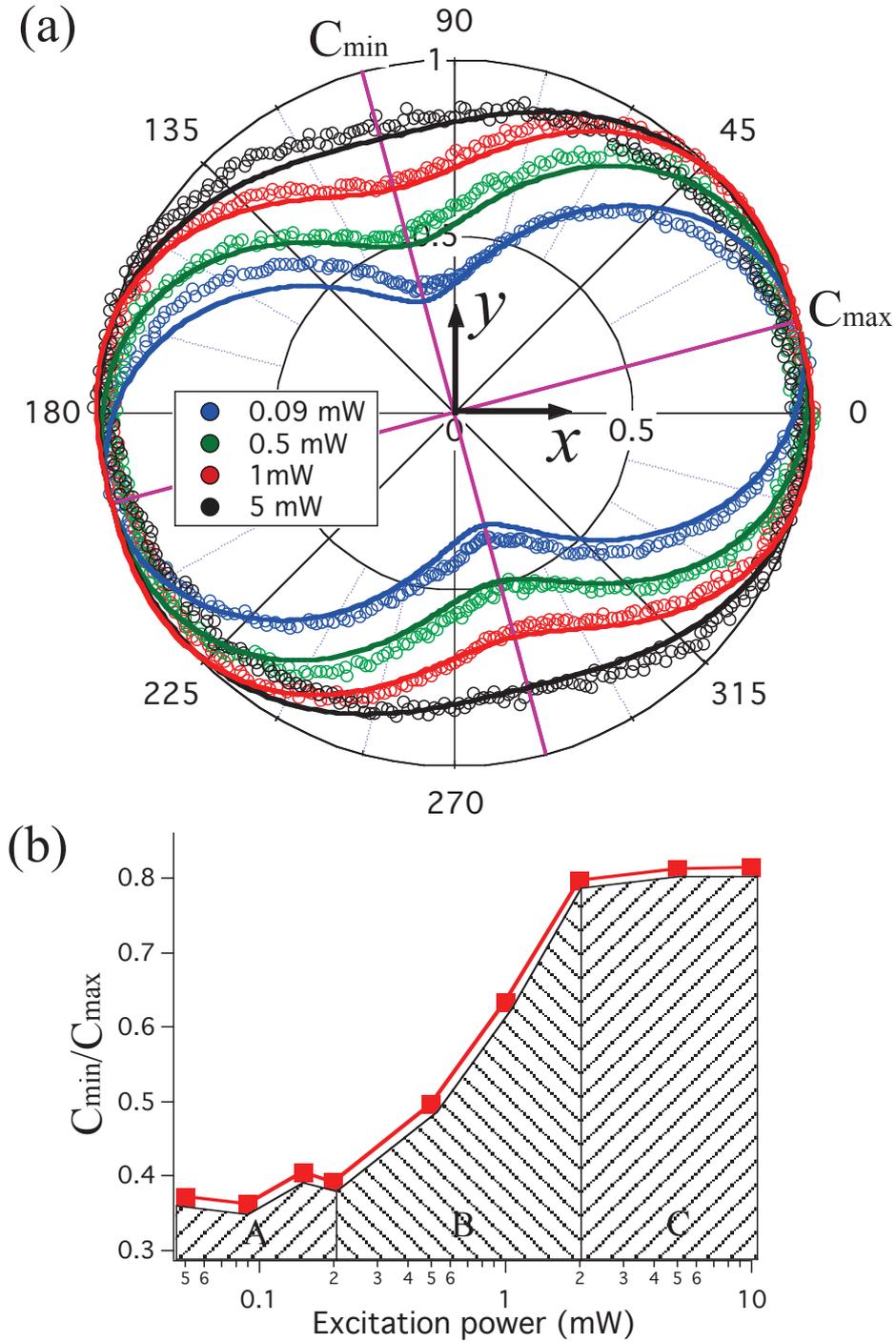
**Figure 8.3:** (a) Normalized photoluminescence of a single NV color-center as a function of polarization orientations of the excitation laser for different excitation powers. The angle between the polarization P corresponding to minimal counts ($C_{min}$) and $Ox$-axis is 105°, in agreement with ODMR measurement (see next Section). (b) Ratio of minimal counts and maximal counts, $C_{min}/C_{max}$, as a function of the excitation power. Three ranges of the excitation power correspond to A: no saturation; B: only one dipole is saturated; and C: two dipoles are saturated.

high excitation power. We model the absorption saturation by considering independent saturations behaviors of each of the two dipoles. Since the two dipoles $D_1$ are $D_2$ are equivalent with respect to the absorption behavior, the interaction between $D_1$ and P will also represent the one between $D_2$ and P. We can set $P = D_1 = 1$ to normalize Equation 8.1 then,

$$(P_1 \cdot D_{11})_{\text{max}} = 1 \tag{8.4}$$

$$(P_2 \cdot D_{12})_{\text{max}} = \cos(\theta) < 1 \tag{8.5}$$

The absorption effect will saturate faster at $P_1$ direction than at $P_2$ direction. In the high power regime, the absorption efficiency can be rewritten as:

$$I_1 = P^2 \times D_1^2 (A \cos(\alpha - \phi - 90) \cos(\beta) + B \sin(\alpha - \phi - 90) \sin(\beta) \cos(\theta))^2 \tag{8.6}$$

$$I_2 = P^2 \times D_2^2 (A \cos(\alpha - \phi - 90) \sin(\beta) - B \sin(\alpha - \phi - 90) \cos(\beta) \cos(\theta))^2 \tag{8.7}$$

Where constant A and B are used to compensate the saturation. The total absorption efficiency become:

$$\begin{aligned} I &= I_1 + I_2 \\ &= P^2 \times D_1^2 (A^2 \sin^2(\alpha - \phi) + B^2 \cos^2(\alpha - \phi) \cos^2(\theta)) \end{aligned} \tag{8.8}$$

The formula representing the total energy absorbed by the two dipoles can be rewritten as

$$I_{\text{abs}} = I_{10} \sin^2(\alpha - \phi) + I_{20} \cos^2(\alpha - \phi) \cos^2 \theta. \tag{8.9}$$

At low excitation power, $I_{10} = I_{20} = I$ and Formula 8.3 is equivalent to 8.9. When the excitation power increases, $I_{10}$ and $I_{20}$ are adjusted independently to fit the saturation level of each dipole. The simulation results using Formula 8.9 are shown in Figure 8.3 (continuous curves) and fit well with the experimental data, for different excitation powers. Three ranges of the excitation power are identified for the studied NV center, namely A (0-0.2 mW): two dipoles are not saturated; B (0.2-2 mW): only one dipole is saturated; and C (>2 mW): two dipoles are saturated.

From this analysis, we come out with two conclusions: i) a single NV color center possesses two orthogonal transitions dipoles, which are in a plane perpendicular to the NV axis; ii) the NV-axis orientation $(\theta, \phi)$ is determined simply by an all-optical method. However, we notice that the total absorption intensity of two dipoles do not depend on angle $\beta$ in their plane. Therefore in order to determine the orientation of each dipole, the analysis of the emission polarization is necessary.

### 8.3.2 Determination of individual dipole orientation

Assuming that the emission dipoles are perfectly superimposed to the absorption dipoles. We choose different configurations of the excitation laser beam polarization,
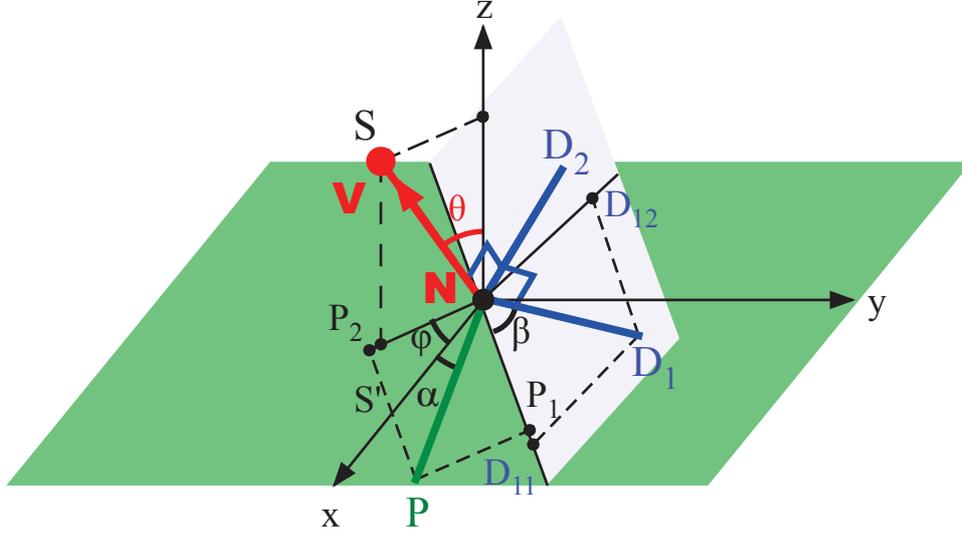
**Figure 8.4:** Modeling of the optical transition dipoles ($D_1$ and $D_2$) associated to a single NV color center and polarizations. $D_1$ and $D_2$ are in the plane perpendicular to NV-axis (**S**). This plane has a cross-line L with the $(x, y)$-plane (polarization plane). P represents the polarization of the excitation light and also the polarizer orientation, see 8.1.

such as linear polarization at maximal absorption ($\alpha=15°$) or at minimal absorption ($\alpha=105°$), or circular polarization, and analyze the polarization of the photoluminescence by rotating the polarizer sheet in front of the avalanche photodiode (Figure 8.1). The angle locating this polarizer axis is called $\alpha'$, which can be viewed in the same scheme as $\alpha$ in Figure 8.4.

Interestingly, the polarization of the emission of a single NV color center keeps unchanged for any excitation laser polarization configurations (linear, circular) and any excitation powers, as shown in Figure 8.5. To explain this independence of the photoluminescence on the excitation laser polarization and power, note that at cryogenic temperature, two dipoles are already weakly coupled,[73], when one of them is excited, 30% of the emission comes from the other dipole. Our experimental observations therefore suggest that at room temperature, these two dipoles are strongly coupled, so that no matter which dipole is excited, both of them emit the same quantity of photoluminescence intensity ($Q$). The emitted photons are detected by the microscope objective, whose optical axis is along the $z$-axis. To simplify, we assume that only the photons emitted along the $Oz$-axis can be detected. The photoluminescence intensities ($E_1$, $E_2$) emitted by each dipole and collected by the microscope objective can be calculated as:

$$E_1 = Q \sin^2 \gamma_1 = Q(1 - \sin^2 \theta \sin^2 \beta) \qquad (8.10)$$

$$E_2 = Q \sin^2 \gamma_2 = Q(1 - \sin^2 \theta \cos^2 \beta) \qquad (8.11)$$
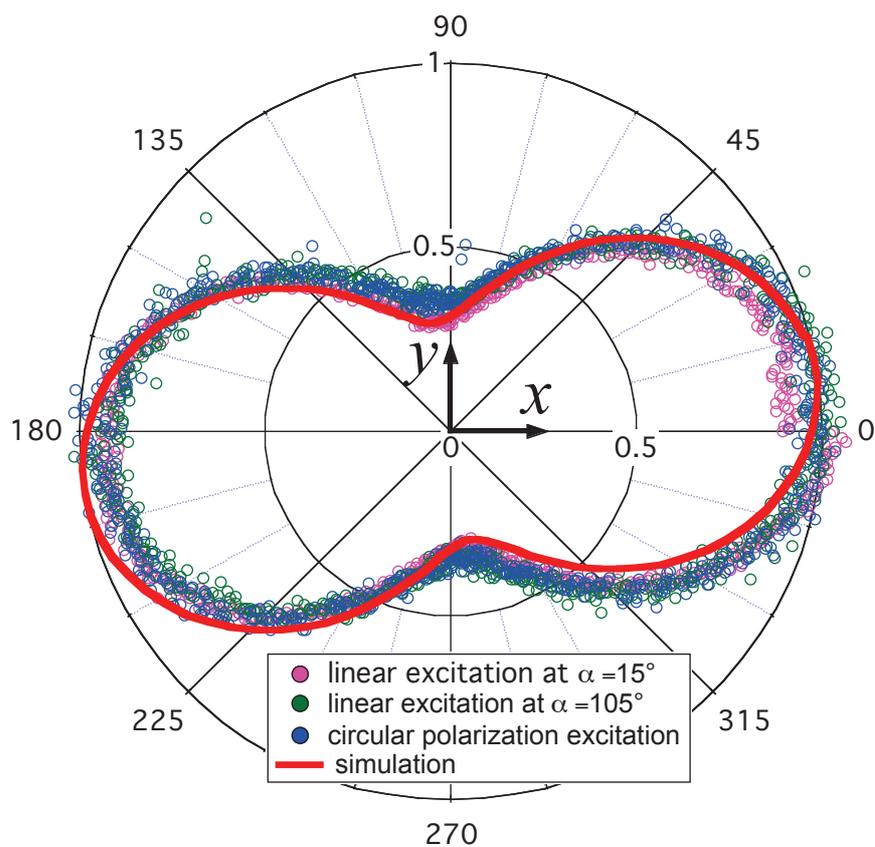
**Figure 8.5:** Normalized NV color center photoluminescence as a function of the analyzing polarizer orientation for three different excitation polarization types. The polarizer is placed in front of the avalanche photodiode and its axis direction is controlled by a rotation motor. The laser excitation power is 0.09 mW.

where $\gamma_1$, $\gamma_2$ are the angles between D$_1$, D$_2$ and the $Oz$-axis, respectively.

As we use a polarizor in front of the photodiode, only the photon whose electric field is along the polarizer axis can be detected. We obtain

$$
\begin{aligned}
E_1^{\text{detected}} &= E_1 \cos^2 \varphi_1 \\
&= Q(1 - \sin^2 \theta \sin^2 \alpha)(\sin(\alpha - \phi) \cos \beta + \cos(\alpha - \phi) \sin \beta \cos \theta)^2
\end{aligned}
\tag{8.12}
$$

$$
\begin{aligned}
E_2^{\text{detected}} &= E_2 \cos^2 \varphi_2 \\
&= Q(1 - \sin^2 \theta \cos^2 \alpha)(\sin(\alpha - \phi) \sin \beta - \cos(\alpha - \phi) \cos \beta \cos \theta)^2
\end{aligned}
\tag{8.13}
$$

where $\varphi_1$ and $\varphi_2$ are the angles between D$_1$, D$_2$ and P, respectively.

The total detected photoluminescence is then

$$
E_{\text{total}} = E_1^{\text{detected}} + E_2^{\text{detected}}
\tag{8.14}
$$

which now depends on the orientation of each dipole with respect to, for example, the cross-line L by an angle $\beta$.

By fitting the experimental data using formula 8.12, 8.13, 8.14, with known angles $(\theta, \phi)$, we obtain $\beta = 50° \pm 1°$ for the investigated NV color center.

In conclusion, by a simple all-optical method, by measuring the polarization dependence of excitation and emission, we are able to determine the optical transition dipoles and their orientations and also the orientation of a single NV color center in a diamond nanocrystal that is randomly oriented in space. In order to validate the use of this all-optical technique, we demonstrate in the next Section another alternative method based on the spin resonance technique to determine the orientation of the NV electron spin-axis, which is equivalent to the NV-axis.

## 8.4   Determination of the orientation of a single NV electron spin

Based on the Zeeman effect, we have designed a two-measurement technique to determined the spin orientation of the NV center. In fact, if we fix the **B**-field orientation and change its magnitude, we can infer the angle ($\theta$) between the **B**-field and **S**-orientation, from the Zeeman spitting. Further more, if we fix the **B**-field magnitude and change its orientation, the smaller the angle ($\theta_{\text{min}}$) between the **B**-field and **S**-orientation is, the stronger Zeeman effect (the separation of the resonance frequency) can be obtained.

Firstly, we apply the **B**-field along the $Oz$-axis (Figure 8.6(a)), corresponding to the optical axis of the microscope objective, and we change **B**-magnitude by translating
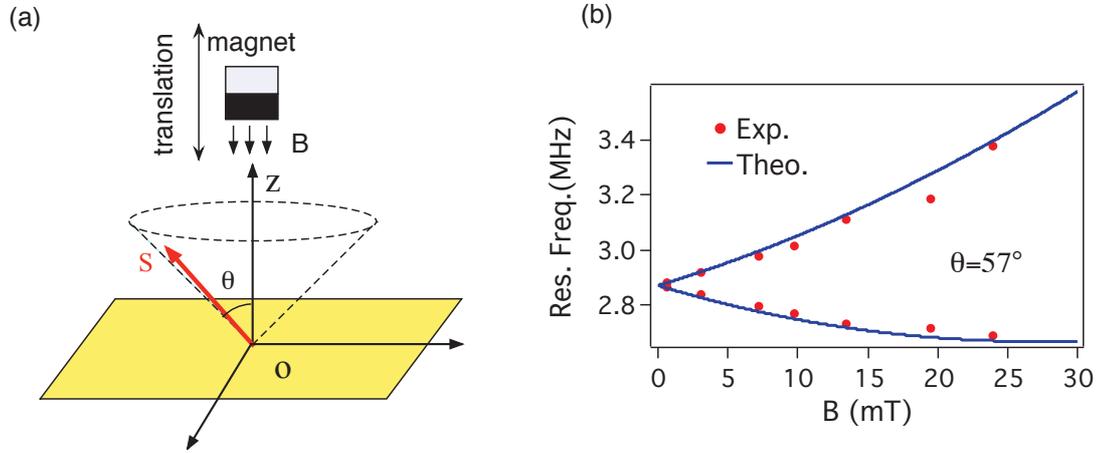
**Figure 8.6:** Determination of the orientation of a single NV spin (**S**) by ODMR method. First measurement: $\theta$-angle is obtained by changing the magnetic field magnitude, which is controlled by translating vertically the magnet along the $(Oz)$ axis. $(x, y)$ is the sample plane containing also the polarization of the excitation light.

the permanent magnet along the $Oz$-axis. By scanning the microwave frequencies, we obtained two resonance peaks for each magnet position, with an increasing splitting upon the increase of the **B**-field magnitude (Figure 8.6(b)). By comparing with the numerical simulation[148] using equation (5.3), we obtained then the $\theta$-angle ($\theta = 57°\pm1°$) between the **B**-field and the NV spin orientation. In the $(O, x, y, z)$ coordinate reference frame, this $\theta$-angle is called the polar angle of the NV spin. Of course, only $\theta$-angle is not enough to confirm the orientation of the NV spin, because **S** can be in any orientation belonging to a cone as shown in Figure 8.6(a).

We then keep the distance between the magnet and the NV-center constant in order to fix the **B**-magnitude applied to the NV spin. The magnet is then rotated around the $Oz$-axis, by an angle $\phi$, with the condition that the magnet North-South axis is always pointing toward the NV-center, as shown in Figure 8.7(a). Doing that, we change the angle between **B**-field and **S**-axis. According to Zeeman effect, the resonance peaks positions, corresponding to $m_s = 0 \leftrightarrow m_s = -1$ and $m_s = 0 \leftrightarrow m_s = +1$ transitions, vary as a function of $\phi$, and when the **B**-field and **S**-axis angle is minimal (corresponding to $\theta_{\min}$), the splitting between the two resonance peaks is maximal.

Figure 8.7 shows the experimental data of resonance frequencies versus the rotation $\phi$-angle in comparison with theoretical calculations. In the $(O, x, y, z)$ reference frame, we then obtained the azimuthal angle ($\phi = 105°\pm1°$) of the studied NV spin, which corresponds to the $\theta_{\min}$-angle between **B** and **S**.

By realizing these two simple measurements, we determined accurately the orientation of a single electron spin associated to a single NV color center in an arbitrarily
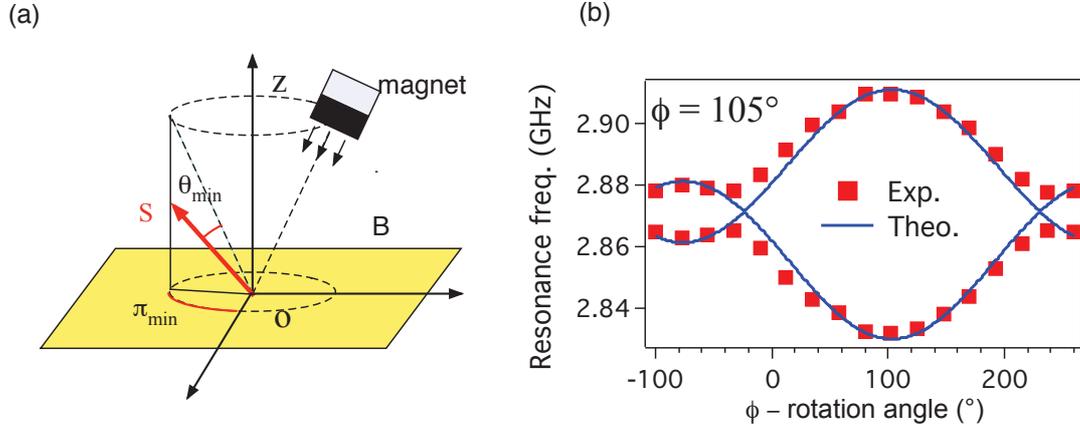
**Figure 8.7:** Determination of the orientation of a single NV spin (**S**) by ODMR method. Second measurement: the azimuthal $\phi$-angle is obtained by changing the magnetic field (**B**) orientation. (a) The magnet is rotated horizontally around the $Oz$-axis while its North-South axis is always pointing towards the NV color center. Doing that, the angle between **B** and **S** is changed, and the two resonances frequencies varies as plotted on (b). **B**-magnitude is kept constant at 3.5 mT.

oriented diamond nanocrystal. The obtained angles ($\theta = 57°$, $\phi = 105°$) of the studied spin are almost identical to the results obtained by the all-optical method ($\theta = 53°$, $\phi = 105°$). The small variation of the $\theta$-angle is probably due to the calculation method based on the ratio $C_{\min}/C_{\max}$ of the all-optical technique. Indeed, this ratio is affected by the detected ambient photons and the stability of the detection system. The electron spin resonance method is based only on the magnetic resonant frequencies and therefore avoid the influence of these noises.

## 8.5   Conclusions

In conclusion, we have demonstrated a simple measurement technique based on the analysis of the excitation and emission polarizations to determine the transitions dipoles orientations and spin-axis of a single NV color center in an arbitrary oriented diamond nanocrystal. By varying the orientation of the linear polarization of the excitation laser beam, we experimentally confirm the existence of two optical transition dipoles of a single NV color center, which are in the plane perpendicular to the NV spin axis. Moreover, the orientation of each dipole can also be determined by analyzing the photoluminescence polarization with a linear polarizor. These results are enforced by an alternative measurement technique based on the optically detected magnetic resonance, which allows to determine with an accuracy of $< \pm 1°$ the orientation of a

single electron spin associated to a single NV color center. The polar and azimuthal angles of a random oriented single NV spin are determined by varying the **B**-field magnitude and orientation, respectively. The results obtained with the polarization analysis are consistent with the ones obtained by the ODMR technique, and are in good agreement with corresponding numerical calculations. The determination of the orientations of a single electron spin and of the optical dipoles of a single color center in a diamond nanocrystal is very important for many applications at room temperature, such as NV color center-based magnetic field sensor at the nanoscale

# Conclusion and outlook

In this work, the prospect of using NV color center as a qubit for the quantum information process has been studied. For this propose different aspects were examined. Two charge states of NV color center were investigated firstly, followed by controlling the NV photoluminescence with IR irradiation. Then three approaches to increase the confocal microscope resolution have been explored. In Chapter 5, polarized excitation was carried out to study NV center's optical dipoles. In Chapter 6, Zeeman effect was employed to determined NV spin orientation which is perpendicular to the NV optical dipoles. Finally, NV spin was manipulated with microwave field and magnetic field, the interaction of NV spin with external field was observed optically.

The NV color center exhibits photochromic effect in certain samples and have various behaviors. Apparently, neutral charge state of NV center is more stable at low excitation power. Our observation shows that $NV^0$ center is "brighter " than $NV^-$ center, and we propose a two-level energy scheme for $NV^0$ color center base on the photon correlation curve at saturation power and the PL intensities of the two charge states of a photochromic single NV center.

The photoluminescence of NV center was observed to be quenched by the pulsed infrared excitation. By exciting the diamond sample with a high peak intensity pulsed IR beam, diamond crystal is locally annealed due to the multi-photon absorption of the diamond crystal, leading to the change of the energy level of the NV color centers embedded inside the diamond. Consequently, the photoluminescence of NV color centers is quenched to almost 80%, depending on the IR excitation intensity. The quenching effect is demonstrated reversible without and with IR excitation, with a typical response time of hundred picoseconds. The rapid photoluminescence quenching with very sort time response is useful for rapid switching of NV color center based single photon source

To address optically a single color center without perturbing the neighbors is essential in the realization of diamond-based quantum computer functioning at room temperature. Hence it is necessary to increase the resolving ability of the system. Three different approaches have been demonstrated to achieve the super-resolution of optical microscopy. The first one is amplitude modulated annular beam, which can

increase the lateral resolution by 30%, this technique is suitable for 2D imaging, nano-fabrication, data storage et. al. The second one is making a phase modulated doughnut beam work at the saturation regime of fluorophore (i.e., NV color center), this technique is able to distinguish two NV colors 250nm apart. The third one is a STED-like super resolution imaging based on the IR thermal quenching effect of NV color center in diamond, the nature of thermal effect makes it can only be applied for the diamond nanocrystals.

The NV electron spin can be manipulated by microwave field and magnetic field. the fluorescence cycle and Rabi oscillation are competing in the aspect of population distribution. The fluorescence cycle polarizes NV center into $|0\rangle$ state, by increasing the excitation power, the fluorescence cycle is accelerated and the spin will be polarized to $|0\rangle$ state quickly. In contrast, the resonant microwave field induces the Rabi oscillation between $|0\rangle$ state and $|\pm 1\rangle$ states. Increasing the microwave power will increase the Rabi frequency, and the population will be redistributed in a smaller period. The static magnetic field induces Zeeman effect, the energy levels of the spin substates will be splitted. Besides, if the magnetic field is not aligned along the NV axis, it will change the eigenstates composition, the $|0\rangle$ state will be described by (mostly) $m_s = 0$ eigenfunction, as well as a $m_s = \pm 1$ component.

Coupling NV center to an optical microcavity has been studied widely because it can strongly enhance the performance of NV center, improving, e.g., the photon emission rate and photon indistinguishability due to the (coherent) interaction with the highly localized photon field of the cavity. Properly positioning NV color center is supposed to largely enhance the coupling property. The NV axis orientation can be determined either from ESR spectrum or from the dipole position. The NV dipole position can be achieved by measuring the polarization dependence of excitation and emission.

This work may hopefully contribute to a better understanding of the properties of the NV color centers for the applications of quantum information and high sensitivity magnetometry.

# Bibliography

1. E. Abbe, "Theorie des mikroskops und der mikroskopischen wahrnehmung" *Arch. Mikrosk. Anat.* **9**, (1873) 413.

2. V. M. Acosta, E. Bauch, M. P. Ledbetter, C. Santori, K. -M. C. Fu, P. E. Barclay, R. G. Beausoleil, H. Linget, J. F. Roch, F. Treussart, S. Chemerisov, W. Gawlik, D. Budker, "Diamonds with a high densiity of nitrogen-vacancy centers for magnetometry applications" *Phys. Rev. B* **80** (2009) 115202.

3. I. Aharonovich, S. Castelletto, B. C. Johnson, J. C. McCallum, D. A. Simpson, A. D. Greentree, S. Prawer, "Chromium single-photon emitters in diamond fabricated by ion implantation" *Phys. Rev. B* **81** (2010) 121201(R).

4. T. P. M. Alegre, C. Santori, G. Medeiros-Ribeiro, R. G. Beausoleil, "Polarization-selective excitation of nitrogen vacancy centers in diamond" *Phys. Rev. B* **76** (2007) 165205.

5. R. Alléaume, F. Treussart, G. Messin, Y. Dumeige, J-F. Roch, A. Beveratos, R. Brouri-Tualle, J-P. Poizat, P. Grangier, "Experimental open-air quantum key distribution with a single-photon source" *New J. Phys.* **6** (2004) 92.

6. E. Ampem-Lassen, D. A. Simpson, B. C. Gibson, S. Trpkovski, F. M. Hossain, S. T. Huntington, K. Ganesan, L. C. L. Hollenberg, S. Prawer, "Nano-manipulation of diamond-based single photon sources" *Optics Express* **17** (2009) 11287.

7. D. D. Awschalom, R. Epstein, R. Hanson, *Scientific American* **297** (2007) 84.

8. R. S. Balmer, J. R. Brandon, S. L. Clewes, H. K. Dhilon, J. M. Dodson, I. Friel, P. N. Inglis, T. D. Madgwick, M. L. Markham, T. P. Mollart, N. Perkins, G. A. Scarsbrook, D. J. Twitchen, A. J. Whitehead, J. J. Wilman, S. M. Woollard, "Chemical vapour deposition synthetic diamond: materials, technology and applications" *J. Phys. Condens. Matter* **21** (2009) 364211.

9. G. Balasubramanian, I. Y. Chan, R. Kolesov, M. Al-Hmoud, J. Tisler, C. Shin, C. Kim, A. Wojcik, P.R. Hemmer, A. Krueger, T. Hanker, A. Leitenstorfer, R. Bratschitsch, F. Jelezko, J. Wrachtrup, "Nanoscale imaging magnetometry with diamond spins under ambient conditions" *Nature* **455** (2008) 648.

10. G. Balasubramanian, P. Neumann, D. Twitchen, M. Markham, R. Kolesov, N. Mizuochi, J. Isoya, J. Achard, J. Beck, J. Tissler, V. Jacque, P. R. Hemmer, F. Jelezko, J. Wrachtrup, "Ultralong spin coherence time in isotopically engineered diamond" *Nat. Mat.* **8** (2009) 383.

11. P. E. Barclay, K.-M. C. Fu, C. Santori, R. G. Beausoleil, "Chip-based microcavities coupled to nitrogen-vacancy centers in single crystal diamond" *Appl. Phys. Lett.* **95** (2009) 191115.

12. P. E. Barclay, C. Santori, K.-M. Fu, R. G. Beausoleil, O. Painter, "Coherent interference effects in a nano-assembled diamond NV center cavity-QED system" *Optics Express* **17** (2009) 8081.

13. A. Batalov, C. Zierl, T. Gaebel, P. Neumann, I.-Y. Chan, G. Balasubramanian, P. R. Hemmer, F. Jelezko, J. Wrachtrup, "Temporal conherence of photons emitted by single nitrogen-vacancy defect centers in diamond using optical rabi-oscillations" *Phys. Rev. Lett.* **100** (2008) 077401.

14. S. C. Benjamin, D. E. Browne, J. Fitzsimons, J. J. L. Morton, "Brokered graph state quantum computing" *New J. Phys* **8** (2006) 141.

15. S. J. Bending, "Local magnetic probes of superductors" *Adv. Phys.* **48** (1999) 449

16. A. Beveratos, R. Brouri, J. -P. Poizat, P. Grangier, "Bunching and antibunching from single NV color centers in diamond" *arXiv:quant-ph/0010044v1.*

17. A. Beveratos, R. K
   textquotedbluhn, S. Brouri, T. Gacoin, J. -P. Poizat, P. Grangier, "Room temperature stable single-photon source" *Eur. Phys. J. D* **18** (2002) 191.

18. G. Binnig, C. F. Quate, "Atomic force microscope" *Phys. Rev. Lett.* **56** (1986) 930.

19. G. Binnig, H. Rohrer, "Scanning tunneling microscopy" *IBM J. Res. Dev.* **30** (1986) 355.

20. H. Blatt, R. J. Tracy, B. E. Owens *Petrology: igneous, sedimentary, and metamorphic* (San Francisco, CA: Freeman) (1996) 212.

21. M. Born and E. Wolf, *Principles of Optics*, Pergamon, New York, 1980.

22. F. P. Bundy, H. T. Hall, H. M. Strong, R. H. Wentorf, Jun, "Man-made diamonds" *Nature* **176** (1955) 51.

23. Y.-R. Chang, H.-Y. Lee, K. Chen, C.-C. chang, D.-S. Tsai, C.-C. Fu, T.-S. Lim, Y.-K. Tzeng, C.-Y. Fang, C.-C. Han, H.-C. Chang, W. Fann, "Mass production

and dynamic imaging of fluorescent nanodiamonds" *Nat. Nanotech.* **3** (2008) 284.

24. A. M. Chang, H. D. Hallen, L. Harriott, H. F. Hess, H. L. Kao, J. Kwo, R. E. Miller, R. Wolfe, J. van der Ziel, T. Y. Chang, "Scanning Hall probe microscopy" *Appl. Phys. Lett.* **61** (1992) 1974.

25. J.-I. Chao, E. Perevedentseva, P.-H. Chung, K.-K. Liu, C.-Y. Cheng, C.-C. Chang, C.-L. Cheng, "Nanometer-sized diamond prticle as a probe for biolabeling" *Biophys. J.* **93** (2007) 2199.

26. F. T. Charnock, T. A. Kenndy, "Combined optical and microwave approach for performing quantum spin operations on the nitrogen-vacancy center in diamond" *Phys. Rev. B* **64** (2001) 041201.

27. C.-L. Cheng, C.-F. Chen, W.-C. Shaio, D.-S. Tsai, K.-H. Chen, "The CH stretching feature on diamonds of different origins" *Diamond Relat. Mater.* **14** (2005) 1455.

28. L. Childress, J. M. Taylor, A. S. Sørensen, M. D. Lukin, "Fault-tolerant quantum repeaters with minimal physical resources and implementations based on single-photon emitters" *Phys. Rev. A* **72** (2005) 052330.

29. L. Childress, M. V. Gurudev Dutt, J. M. Tylor, A. S. Zibrov, F. Jelezko, J. Wrachtrup, P. R. Hemmer, M. D. Lukin, "Coherent dynamics of coupled electron and nuclear spin qubits in diamond" *Science* **314** (2006) 281.

30. A. T. Collins, "The fermi level in diamond" *J. Phys., Condens. Matter.* **14** (2002) 3743.

31. A. V. Crewe, J. Wall, J. Langmore, "Visibilit of Single Atoms" *Science* **12** (1970) 1338.

32. C. L. Degen, "Scanning magnetic field microscope with a diamond single-spin sensor" *Appl. Phys. Lett.* **92** (2008) 243111.

33. G. Davies, M. F. Hamer, "Optical studies of the 1.945 eV vibronic band in a color center in diamond" *Proc. Royal. Soc. London A* **348** (1976) 285.

34. G. Davies, S. C. Lawson, A. T. Collins, A. Mainwood, S. J. Sharp, "Vacancy-related centers in diamond" *Phys. Rev. B* **46** (1992) 13157.

35. G. Davies, *Properties and growth of diamond (EMIS Data Review Series* The Institution of Electrical Engineers, London, (1994).

36. P. Dedecker, J.-I. Hotta, C. Flors, M. Sliwa, H. Uji-i, M. B. J. Roeffaers, R. Ando, H. Mizuno, A. Miyawaki, J. Hofkens, "Subdiffraction imaging through the

selective donut-mode depletion of thermally stable photoswitchable fluorophores: numerical analysis and application to the fluorescent protein Dronpa" *J. Am. Chem. Soc.* **129** (2007) 16132.

37. V. V. Dobrovitski, A. E. Feiguin, D. D. Awschalom, R. Hanson, "Decoherence dynamics of a single spin versus spin ensemble" *Phys. Rev. B*, **77** (2008) 245212.

38. A. Drabenstedt, L. Fleury, C. Tietz, F. Jelezko, S. Kilin, A. Nizovtzev, J. Wrachtrup, "Low-temperature microscopy and spectroscopy on single defect centers in diamond" *Phys. Rev. B* **60** (1999) 11503.

39. Y. Dumeige, F. Treussart, R. Alleaume, T. Gacoin, J-F. Roch, P. Grangier, "Photo-induced creation of nitrogen-related color centers in diamond nanocrystals under femtosecond illumination" *J. Lumin.* **109** (2004) 61.

40. A. R. Edmonds, "The theory of the quadratic Zeeman effect" *J. Phys. Colloques* **31** (1970) C4-71.

41. E. Betzig, A. Harootunian, A. Lewis, M. Isaacson, "Near-field diffraction by a slit: implications for superresolution microscopy" *Appl. Opt.* **25** (1986) 1890.

42. R. J. Epstein, F. M. Mendoza, Y. K. Kato, D. D. Awschalom, "Anisotropic interactions of a single spin and dark-spin spectroscopy in diamond" *Nat. Phys.* **1** (2005) 94.

43. O. Faklaris, D. Garrot, V. Joshi, F. Druon, J-P. Boudou, T. Sauvage, P. Georges, P. A. Curmi, F. Treussart, "Detection of single photoluminescent diamond nanoparticles in cells and study of the internalization pathway" *Small* **4** (2008) 2236.

44. S. Felton, A. M. Edmonds, M. E. Newton, P. M. Martineau, D. Fisher, D. J. Twitchen, "Electron paramagnetic resonance resonance studies of the neutral nitrogen vacancy in diamond" *Phys. Rev. B* **77** (2008) 081201(R).

45. A. A. Finnerty, F. R. Boyd, "Evaluation of thermobarometers for garnet peridotites" *Geochim. Cosmochim. Acta* **48** (1984) 15.

46. K.-M. C. Fu, C. Santori, P. E. Barclay, L. Aharonovich, S. Prawer, N. Meyer, A. M. Holm, R. G. Beausoleil, "Coupling of nitrogen-vacancy centers in diamond to a GaP waveguide" *Appl. Phys. Lett.* **93** (2008) 234107.

47. K. -M. C. Fu, C. Santori, P. E. Barclay, R. G. Beausolei, "Conversion of neutral nitrogen-vacancy centers to negatively charged nitrogen-vacancy centers through selective oxidation" *Appl. Phys. Lett.* **96** (2010) 121907.

48. T. Gaebel, I. Popa, A. Gruber, M. Domhan, F. Jelezko, J. Wrachtrup, "Stable single-photon source in the near infrared" *New J. Phys.* **6** (2004) 98.

49. T. Gaebel, M. Domhan, C. Wittmann, I. Popa, F. Jelezko, J. Rabeau, A. Greentree, S. Prawer, E. Trajkov, P. R. Hemmer, J. Wrachtrup, "Photochromism in single nitrogen-vacancy defect in diamond" *Appl. Phys. B* **82** (2006) 243.

50. T. Gaebel, M. Domhan, I. Popa, C. Wittmann, P. Neumann, F. Jelezko, J. R. Rabeau, N. Stavrias, A. D. Greentre, S. Prawer, J. Meijer, J. Twamley, P. R. Hemmer, J. Wrachtrup, "Room-temperature coherent coupling of single spins in diamond" *Nat. Phys.* **2** (2006) 408.

51. A. Gali, M. Fyta, E. Kaxiras, "Ab inito supercel calculation on nitrogen-vacancy center in diamond: electronic structure and hyperfine tensors" *Phys. Rev. B* **77** (2008) 155206.

52. A. Gali, "Theory of the neutral nitrogen-vacancy center in diamond and its application to the relization of a qubit" *Phys. Rev. B* **79** (2009) 235210.

53. A. Gruber, A. Dräbenstedt, C. Tietz, L. leury, J. Wrachtrup, C. Von Borczyskowsi, "Scanning confocal optical microscopy and magnetic resonance on single defect centers" *Science* **276** (1997) 2012.

54. M. V. Gurudev Dutt, L. Childress, L. Jiang, E. Togan, J. Maze, F. Jelezko, A. S. Zibrov, P. R. Hemmer, M. D. Lukin, "Quqntum register based on individual electronic and nuclear spin qubits in diamond" *Science* **316** (2007) 1312.

55. M. Gu, *Principle of three-dimensional imaging in confocal microscopes* World Scientific, Singapore, (1996).

56. M. Gu, *Advanced optical imaging theory*, Spinger, Heidelberg, 2000.

57. P. Zijlstra , J. W. W. Chon, M. Gu, "Five-dimensional optical recording mediated by surface plasmons in gold nanorods" *Nature* **459** (2009) 410.

58. L. T. Hall, J. H. Cole, C. D. Hill, L. C. L. Hollenberg, "Sensing of fluctuating nanoscale magnetic fields using nitrogen-vacancy, centers in diamond" *Phys. Rev. Lett.* **103** (2009) 220802.

59. L. T. Hall, C. D. Hill, J. H. Cole, L. C. L. Hollenberg, "Ultrasensitive diamond magnetometry using optimal dynamic decoupling" *Phys. Rev. B* **82** (2010) 045208.

60. K. Y. Han, K. I. Willig, E. Rittweger, F. Jelezko, C. Eggeling, S. W. Hell, "Three-dimensional stimulated emission depletion microscopy of nitrogen-vacancy centers in diamond using continuous-wave light" *Nano Lett.* **9** (2009) 3323.

61. R. Hanson, F. M. Mendoza, R. J. Epstein, D. D. Awschalom, "Polarization and readout of coupled single spins in diamond" *Phys. Rev. Lett.* **97** (2006) 087601.

62. R. Hanson, "Quantum information: mother nature outgrown" *Nature Mat.* **8** (2009) 368.

63. R.T. Harley, M.J. Henderson, R.M. Macfarlane, "Persistent spectral hole burning of colour centres in diamond" *J. Phys. C: Solid State Phys. 17* (1984) L233.

64. S. W. Hell, J. Wichman, "Breaking the diffraction limit of resolution by stimulated emission: stimulated-emission depletion microscopy" *Opt. Commun.* **19** (1994) 780.

65. S. W. Hell, P. E. Hännien, A. Kuusisto, M. Schrader, E. Soini, "Annular aperture two-photon excitation microscopy" *Opt. Commun.* **117** (1995) 20.

66. S. W. Hell, "Toward fluorescence nanoscopy" *Nat. Biotechnol,* **21** (2003) 1347.

67. M. Hofmann, C. Eggeling, S. Jakobs, S. W. Hell "Breaking the diffraction barrier in fluorescence microscopy at low light intensities by using reversibly photoswichable proteins" *PNAS*, **102** (2005) 17565.

68. K. Izukawa, I. Okumura, "Optical system for making an annular beam" *United States Paten* **4,657,360** (1987).

69. V. Jacques, E. Wu, F. Grosshans, F. Treussart, P. Grangier, A. Aspect, J-F. Roch, "Experimental realization of wheeler's delayed-choice gedanken experiment" *Science* **315** (2007) 966

70. F. Jelezko, T. Gaebel, I. Popa, A. Gruber, J. Wrachtrup, "Observation of coherent oscillations in a single electron spin" *Phys. Rev. Lett.* **92** (2004) 076401.

71. F. Jelezko, T. Gaebel, I. Popa, M. Domhan, A. Gruber, J. Wrachtrup, "Observation of coherent oscillation of a single nuclear spin and realization of a two-qubit conditional quantum gate" *Phys. Rev. Lett.* **93**, (2004)130501.

72. G. Jia, H. Wang, L. Yan, X. Wang, R. Pei, T. Yan, Y. Zhao, X. Guo, "Cytotoxicity of carbon nanomaterials: single-wall nanotube, multi-wall nanotube, and fullerene" *Eniron. Sci. Technol.* **39** (2005) 1378.

73. F. Kaiser, V. Jacques, A. Batalov, P. Siyushev, F. Jelezko, J. Wrachtup, "Polarization properties of single photons emitted by nitrogen-vacancy defect in diamond at low temperature" *arXiv:0906.3426v1 [quant-ph]*.

74. N. Kossovsky, A. Gelman, H. J. Hnatyszyn, A. Rajguru, R. L. Garrell, S. Torbati, S. S. F. Freitas, G.-M. Chow, "Surface-modified diamond nanoparticles as antigen delivery vehicles" *Bioconjugate Chem.* **6** (1995) 507.

75. C. Kurtsiefer, S. Mayer, P. Zarda, H. Weinfurter, "Stable solid-state source of single photons" *Phys. Rev. Lett.* **85** (2000) 290.

76. N. D. Lai, J. H. Lin, P. W. Chen, J. L. Tang, C. C. Hsu, "Controlling aspect ration of focal spots of high numerical aperture objective lens in multi-photon absorption process" *Opt. Commun* **258** (2006) 97.

77. N. D. Lai, D. Zheng, F. Jelezko, F. Treussart, J-F. Roch, "Influence of a static magnetic field on the photoluminescence of an ensemble of nitrogen-vacancy color centers in a diamond single-crystal" *Appl. Phys. Lett.* **95** 2009 133101.

78. N. D. Lai, D. Zheng, F. Treussart, J-F. Roch, "Optical determination and magnetic manipulation of single nitrogen-vacancy color center in diamond nanocrystal" *Adv. Nat. Sci.: Nanosci. Nanotechnol.* **1** 015001.

79. J. R. Lakowicz, *Principle of fluorescence spectroscopy* Plenum Press, 1983.

80. S. C. Lawson, D. Fisher, D. C. Hunt, M. E. Newton, "On the existence of positively charged single-substitutional nitrogen in diamond" *J. Phys., Condens. Matter.* **10** (1998) 6171.

81. A. Lenef, S. C. Rand, "Electronic structure of the N-V center in diamond: Theory" *Phys. Rev. B* **53** (1996) 13441.

82. S. van de Linde, S. Wolter, M. Heilemann, M. Sauer, "The effect of photoswitching kinetics and labeling densities on super-resolution fluorescence imaging" *J. Biotechnol.* (2010) doi:10.1016/ j.jbiotec.2010.02.010.

83. K.-K. Liu, C.-L. Cheng, C.-C. Chang, J.-I. Chao, "Biocompatible and detectable carboxylated nanodiamond on human cell" *Nanotechnology* **18** (2007) 325102.

84. J. H. H. Loubser, J. A. van Wyk, "Electron spin resonance in the study of diamond" *Rep. Prog. Phys.* **41** (1978) 1201.

85. B. Lounis, W. E. Moerner, "Single photons on demand from a single molecule at room temperature" *Nature* **407** (2000) 491.

86. M. D. Lukin, P. R. Hemmer, "Quantum entanglement via optical control of atom-atom interaction" *Phys. Rev. Lett.* **84** (2000) 2818.

87. B. J. Maertz, A. P. Wijnheijmer, G. D. Fuchs, M. E. Nowakowski, D. D. Awschalom, "Vector magnetic field microscopy using nitrogen vacancy centers" *Appl. Phys. Lett.* **96** (2010) 092504.

88. H. J. Mamin, M. Poggio, C. L. Degen, D. Rugar, "Nuclear magnetic resonance imaging with 90-nm resolution" *Nat. Nanotechnol.* **2** (2007) 301.

89. N. B. Manson, X.-F. He, and P. T. H. Fisk, "Raman heterodyne detected electro-nuclear-double-resonance measurements of the nitrogen-vacancy center in diamond" *Opt. Lett.* **15** (1990) 1094.

90. N. B. Manson, J. P. Harrison, "Photo-ionization of the nitrogen-vacancy center in diamond" *Dia. Relat. Mat.,* **14** (2005) 1705.

91. N. B. Manson, J. P Harrison, M. J. Sellars, "Nitrogen-vacancy center in diamond: Model of the electronic structure and associated dynamics" *Phys. Rev. B* **74** (2006) 104303.

92. N. B. Manson, J. P. Harrison, M. J. Sellars, "The nitrogen-vacancy center in diamond re-visited" *arXiv:cond-mat/0601360v2.*

93. N.B. Manson, R.L. McMurtrie, "Issues concerning the nitrogen-vacancy center in diamond" *J. Lumin.* **127** (2007) 98.

94. Y. Marting, H. K. Wickramasinghe, "Magnetic imaging by "force microscopy" with 1000 Åresolution" *Appl. Phys. Lett.* **50** (1987) 1455.

95. J. R. Maze, P. L. Stanwix, J. S. Hodges, S. Hong, J. M. Taylor, P. Cappellaro, L. Jiang, M. V. Gurudev Dutt, E. Toga, A. S. Zibrov, A. Yacoby, R. L. Walsworth, M. D. Lukin, "Nanoscale magnetic sensing with an individual electronic spin in diamond" *Nature* **455**(2008) 644.

96. J. Meijer, B. Burchard, "Generagions of single color centers by focused nitrogen implantation" *Appl. Phys. Lett.* **87** (2005) 261909.

97. B. Michael, N. Nils, L. Bernd, B. Oliver, "Controlled coupling of a single-diamond nanocrystal to a photonic crystal cavity" *Opt. Lett.* **34** (2009) 1108.

98. Y. Mita, "Change of absorption spectra in type-Ib diamond with heavy neutron irradiation" *Phys. Rev. B,* **53** (1996) 11360.

99. N. Mizuochi, P. Neumann, F. Rempp, J. Beck, V. Jacque, P. Siyushev, K. Nakamura, D. J. Twitchen, H. Watanabe, S. Yamasaki, F. Jelezko, J. Wrachtrup, "Coherence of single spins coupled to a nuclear spin bath of varying density" *phys. Rev. B* **80** (2009) 041201.

100. W. E. Moerner, "Single-photon sources based on single molecules in solids" *New J. Phys.* **6** (2004) 88.

101. N. Mohan, Y-K. Tzeng, L. Yang, Y. Y. Chen, Y. Y. Hui, C-Y. Fang, H-C. Chang, "Sub-20-nm fluorescent nanodiamonds as photostable biolabels and fluorescence resonance energy transfer donors" *Adv. Mater.* **22** (2010) 843.

102. B. Naydenov, V. Richter, J. Beck, M. Steiner, P. Neumann, G. Balasubramanian, J. Achard, F. Jelezko, J. Wrachtrup, R. Kalish. "Enhanced generation of single optically active spins in diamond by ion implantation" *Appl. Phys. Lett.* **96** (2010) 163108.

103. P. Neumann, N. Mizuochi, F. Rempp, P. Hemmer, H. Watanabe, S. Yamasaki, V. Jacques, T. Gaebel, F. Jelezko, J. Wrachtrup, "Multipartite entanglement among single spins in diamond" *Science* **320** (2008) 1326.

104. P. Neumann, R. Kolesov. V. Jacques, J. Beck, J. Tisler, A. Batalov. L. Rogers, N.B. Manson, G. Balasubramanian, F. Jelezko, J. Wrachtrup, "Excited-state spectroscopy of single NV defects in diamond using optically detected magnetic resonance" *New J. Phys.* **11** (2009) 013017.

105. P. Neumann, R. Kolesov, B. Naydenov, J. Beck, F. Rempp, M. Steiner, V. Jacques, G. Balasubramanian, M. L. Markham, D. J. Twitchen, S. Pezzagna, J. Meijer, J. Twamley, F. Jelezko, J. Wrachtrup, "Quantum register based on coupled electron spins in a room-temperature solid" *Nat. Phys.* **6** (2010) 249.

106. P. Neumann, J. Beck, M. Steiner, F. Rempp, H. Fedder, P. R. Hemmer, J. Wrachtrup, F. Jelezko, "Single-shot readout of a single nuclear spin" *Science* **329** (2010) 542.

107. E. van Oort, N. B. Manson, M. Glasbeek, "Optically detected spin coherence of the diamond n-v center in its triplet ground state" *J. Phys. C: Solid state phys.* **21** (1988) 4385.

108. E. van Oort, P. Stroomer, M. Glasbeek, "Low-field optically detected magnetic resonance of a coupled triplet-doublet defect pair in diamond" *Phys. Rev. B* **42** (1990) 8605.

109. Y.-S. Park, A. K. Cook, H. Wang, "Cavity QED with diamond nanocrystals and silica microspheres" *Nano lett.* **6** (2006) 2075.

110. J. B. Pawly, *Handbook of biological confocal microscopy* Spinger, 2006.

111. J. R. Rabeam S. T. Huntington, A. D. Greentree, S. Prawer, "Diamond chemical-vapor deposition on optical fibers for fluorescence waveguiding" *Appl. Phys. Lett.* **86** (2005) 134104.

112. N.R.S. Reddy, N.B. Manson, E.R. Krausz, "2-laser spectral hole burning in a color center in diamond" *J. Lumin.* **38** (1987) 46.

113. D. Redman, S. Brown, R. H. Sands, S. C. Rand, "Spin dynamics and electronic states of NV centers in diamond by EPR and four-wave-mixing spectroscopy" *Phys. Rev. Lett.* **67** (1991) 3420.

114. E. Rittweger, K. Y. Han, S. E. Irvine, C. Eggeling, S. W. Hell, "STED microscopy reveals crystal colour centres with nanometric resolution" *Nature Photon.* **3** (2009) 144.

115. L. J. Rogers, S. Armstrong, M. J. Sellars and N. B. Manson, "New infrared emission of the NV center in diamond: Zeeman and uniaxial stress studies" *New J. Phys.* **10** (2008) 103024

116. V.A. Pushkarchuk, S. Ya. Kilin, A.P. Nizovtsev, V.E. Borisenko, A.B. Filonov, A.L. Phshkarchuk, S.A. Kuten, "Quantum-chemical modeling of structural, electronic, and spin characteristics of NV centers in nanostructured diamond: surface effect" *Opt. Spec.* **108** (2010) 247.

117. E. Rittweger, D. Wildanger, S. W. Hell, "Far-field fluorescence nanoscopy of diamond color centers by ground state depletion" *Eur. Phys. Lett.* **86** (2009) 14001.

118. D. Rugar, R. Budakian, H. J. Mamin, B. W. Chui, "Single spin detection by magnetic resonance force microscopy" *Nature* **430** (2004) 329.

119. C. Sangtori, M. Pelton, G. Solomon, Y. Dale, Y. Yamamoto, textquotedblleft Triggered single photons from a quantum dot" *Phys. Rev. Lett.* **86** (2001) 1502.

120. C. Santori, P. Tamarat, P. Neumann, J. Wrachtrup, D. Fattal, R. G. Beausoleil, J. Rabeau, P. Olivero, A. D. Greentree, S. Prawer, F. Jelezko, P. Hemmer, "Coherent population trapping of single spins in diamond under optical excitation" *Phys. Rev. Lett.* **97** (2006) 247401.

121. C. Santori, P. E. Barclay, K. -M. C. Fu, R. G. Bausoleil, "Vertical distribution of nitrogen-vacancy centers in diamond formed by ion implantation and annealing" *phys. Rev. B* **79** (2009) 125313.

122. C. Santori, P. E. Barclay, K.-M. C. Fu, R. G. Bausoleil, "Nanophotonics for quantum optics using nitrogen-vacancy centers in diamond" *Nanotechnology* **21** (2010) 274008.

123. N. Shenvi, R. de Sousa, K. B. Whaley, "Universal scaling of hyperfine induced electron spin echo decay" *phys. Rev. B* **71** (2005) 224411.

124. C. J. R. Sheppard, "Validity of the Debye approximation" *Opt. Lett* **25** (2000) 1660.

125. S. Schietinger, T. Schroder, O. Benson, "One-by One coupling of single defect centers in nanodiamonds to high-Q modes of of an optical microresonator" *Nano Lett.* **8** (2008) 3911.

126. S. Schietinger, M. Barth, T. Aichele, O. Benson, "Plasmon-enhanced single photon emission from a nanoassembled metal-diamond hybrid structure at room temperature" *Nano Lett.*, **2009**, *9*, 1694.

127. A. M. Schrand, H. J. Huang, C. Carlson, J. J. Schlanger, E. Osawa, S. M. Hussain, L. M. Dai, "Are diamond nanoparticles cytoxic?" *J. Phys. Chem. B* **111** (2007) 2.

128. C. Shin, C. Kim, R. Kolesov, G. Balasubramanian, F. Jelezko, J. Wrachtrup, P. R. Hemmer, "Sub–optical resolution of single spins using magnetic resonance imaging at room temperature in diamond" *J. Lumin.* **130** (2010) 1635.

129. S. Steinert, F. Dolde, P. Neumann, A. Aird, B. Naydenov, G. Balasubramanian, F. Jelezko, J. Wrachtrup, "High sensitivity magnetic imaging using an array of spins in diamond" *Rev. Sci. Instrum.* **81** (2010) 043705.

130. C-H. Su, A. D. Greentree, L. C. L. Hollenberg, "Towards a picosecond transform-limited nitrogen-vacancy based single photon source" *Opt. Express* **16** (2008) 6240.

131. S. K. Sudheer, V. P. M. Pillai, V. U. Nayar. "Diode pumped Q-switched Nd:YAG laser at 1064 nm with nearly diffraction limited output beam for precise micro-machining of natural diamond for micro electro mechanical systems (MEMS) applications" *J. Optoelectron. Adv. Mater.* **8** (2006) 363.

132. S. Takahashi, R. Hanson, J. van Tol, M. S. Sherwin, D. D. Awshchalom, "Quenching spin decoherence in diamond through spin bath polarization" *Phys. Rev. Lett.* **101** (2008) 047601.

133. J. M. Taylor, P. Cappellaro, L. Childress, L. Jiang, D. Budker, P. R. Hemmer, A. Yacoby, R. Walsworth, M. D. Lukin, "High-sensitivity diamond manetometer with nanoscale resolution" *Nature Phys.* **4** (2008) 810.

134. V. Vaijayanthimalia, Y.-K. Tzheng, H.-C. Chang, C.-L. Li, "The biochompatibility of fluorescent nanodiamonds and their mechanism of cellular uptake" *Nanotechnology* **20** (2009) 425103.

135. C. -S. Yan, Y. K. Vohra, H. -K. Mao. R. J. Hemley. "Very high growth rate chemical vapor deposition of single-crystal diamond" *PNAS* **99** (2002) 12523.

136. Y. Hu, Z. Zhang, Y. Chen, Q. Zhang, W. Huang, "Two-photon-induced polarization-multiplexed and multilevel storage in photoisomeric copolymer film" *Opt, Lett* **35** (2010) 46.

137. A. Young, C. Y. Hu, L. Marseglia, J. P. Harrison, J. L. O'Brien, J. G. Rarity, "Cavity enhanced spin measurement of the ground state spin of an NV center in diamond" *New. J. Phys.* **11** (2009) 013007.

138. J. Wall, J. Langmore, M. Isaacson, A. V. Crewe, "Scanning transmission electron microscopy at high resolution" *PNAS* **71** (1974) 1.

139. C. Wang, C. Kurtsiefer, H. Weinfurter, B. Burchard, "Single photon emission from SiV centers in diamond produced by ion implantation" *J. Phys. B* **39** (2006) 37.

140. C. F. Wang, Y-S. Choi, J. C. Lee, E. L. Hu, J. Yang, J. E. Butler, "Observation of whispering gallery modes in nanocrystalline diamond microdisks" *Appl. Phys. Lett.* **90** (2007) 081110.

141. C. F. Wang, R. Hanson, D. D. Awschalom, E. L. Hu, T. Feygelson, J. Yang, J. E. Butler, "Fabrication and characterization of two-dimensional photonic crystal microcavities in nanocrystalline diamond" *Appl. Phys. Lett.* **91** (2007) 201112.

142. T-L. Wee, Y-K. Tzeng, C-C. Han, H-C. Chang, W. Fann, J-H. Hsu, K-M. Chen, Y-C. Yu, "Two-photon excited fluorescence of nitrogen-vacancy centers in proton-irradiated type Ib diamond" *J. Phys. Chem. A* **111** (2007) 9379.

143. J. Wrachtrup, S. Y. Kilin, A. P. Nizovtsev, "Quantum computation using the $^{13}$C nuclear spins near the single NV defect center in diamond" *Opt. Spectrosc.* **91** (2001) 429.

144. E. Wu, V. Jacque, H. Zhang, P. Grangier, F. Treussart, J.-F. Roch, "Narrow-band single-photon emission in the near infrared for quantum key distribution." *Opt. Exp.* **14** (2006) 1296.

145. A. M. Zaitsev. *Optical properties of diamond: a data handbook* Springer, Berlin, (2000).

146. O. H. Y. Zalloum, M. Parrish, A. Terekhov, W. Hofmeister, "On femtosecond micromachining of HPHT single-crystal diamond with direct laser writing using tight focusing" *Opt. Express* **18** (2010) 13122.

147. W. Zhao, J. Tan, L. Qiu, "Improvement of confocal microscope performance by shaped annular beam and heterodyne confocal techniques" *Optic* **116** (2005) 111.

148. The spin Hamiltonian, which includes the **B**-field coupling, is solved using EasySpin software (Stoll,S.; Schweiger, A. *J. Magn. Reson.* **2006**, *178*, 42) adapted for our purpose.